Solution Growth of Microcrystalline Silicon on Amorphous Substrates

DISSERTATION

zur Erlangung des akademischen Grades

doctor rerum naturalium
(Dr. rer. nat.)
im Fach Physik

eingereicht an der
Mathematisch-Naturwissenschaftlichen Fakultät I
Humboldt-Universität zu Berlin

von
Dipl.-Phys. Robert Heimburger
14.02.1981 in Berlin

Präsident der Humboldt-Universität zu Berlin:
Prof. Dr. Dr. h.c. Christoph Markschies

Dekan der Mathematisch-Naturwissenschaftlichen Fakultät I:
Prof. Dr. Lutz-Helmut Schön

Gutachter:
1. Prof. Dr. Roberto Fornari
2. Prof. Dr. Manfred Mühlberg
3. Prof. Dr. Recardo Manzke

eingereicht am: 29.01.2010
Tag der mündlichen Prüfung: 05.07.2010

Abstract

This work deals with low–temperature solution growth of micro–crystalline silicon on glass. The task is motivated by the application in low–cost solar cells. As glass is an amorphous material, conventional epitaxy is not applicable. Therefore, growth is conducted in a two–step process. The first step aims at the spatial arrangement of silicon seed crystals on conductive coated glass substrates, which is realized by means of vapor–liquid–solid processing using indium as the solvent. Seed crystals are afterwards enlarged by applying a specially developed steady–state solution growth apparatus. This laboratory prototype mainly consists of a vertical stack of a silicon feeding source and the solvent (indium). The growth substrate can be dipped into the solution from the top. The system can be heated to a temperature below the softening point of the utilized glass substrate. A temperature gradient between feeding source and growth substrate promotes both, supersaturation and material transport by solvent convection.

This setup offers advanages over conventional liquid phase epitaxy at low temperatures in terms of achievable layer thickness and required growth times. The need for convective solute transport to gain the desired thickness of at least 50 µm is emphasized by equilibrium calculations in the binary system indium–silicon. Material transport and supersaturation conditions inside the utilized solution growth crucible are analyzed. It results that the solute can be transported from the lower feeding source to the growth substrate by applying an appropriate heating regime. These findings are interpreted by means of a hydrodynamic analysis of fluid flow and supporting FEM simulation.

To ensure thermodynamic stability of all materials involved during steady–state solution growth, the ternary phase equilibrium between molybdenum, indium and silicon at 600 °C was considered. Based on the obtained results, the use of molybdenum disilicide as conductive coating material is proposed. $MoSi_2$ thin films on glass, produced by annealing near–stoichiometric Mo–Si multilayers, are shown to resist solution contact. Subsequent investigation of feasibility of the vapor–liquid–solid mechanism revealed the success of indium microdroplet formation to be determined by both, the multilayer deposition parameters and the substrate temperature during indium deposition.

Steady–state solution growth at 610 °C was utilized to enlarge silicon seed crystals to diameters of up to 200 µm. The grown material has been subject of characterization regarding the crystallinity, orientation and purity. Additionally, morphological anomalies are considered. The outgrown material was found to be bound by {111} facets. Many of these microcrystallites contain at least two twin domains. Twin–assisted growth at formed re-entrant edges promotes high growth rates even at low supersaturation. Additionally, many crystallites exhibit hoppers at the center of their facets. This is explained by a solute concentration inhomogeneity within the diffusion boundary layer of the nutrient solution leading to solute depletion at the facet centers and to morphological instability.

The feasibility of the process for growth of microcrystalline silicon on glass has been shown in principle. Nevertheless, limitations exist regarding the achievable crystalline solidity ratio and the size of crystallites grown under stable conditions.

Zusammenfassung

Die vorliegende Arbeit behandelt die Lösungszüchtung von mikrokristallinem Silicium auf Glas bei niedrigen Temperaturen. Ihre Motivation findet die Methode in der Anwendung als Absorberschicht für kostengünstige Solarzellen. Da Glas ein amorphes Material ist, können konventionelle Epitaxietechniken nicht angewendet werden. Der untersuchte Wachstumsprozess lässt sich in zwei Schritte aufteilen. Zunächst werden separierte Silicium–Saatkristallite auf leitfähig beschichteten Glassubstraten durch Anwendung des Vapor–Liquid–Solid Verfahrens abgeschieden. Als Lösungsmittel kommt Indium zum Einsatz. Die so erzeugten Saatkristallite werden anschließend in einer speziell angepassten Apparatur mittels stationärer Lösungszüchtung vergrößert. Bei der Apparatur handelt es sich um einen Prototypen im Labormaßstab, welcher im Wesentlichen aus einer vertikalen Anordnung eines Sättigungssubstrates und des Lösungsmittels (Indium) besteht. Das Züchtungssubstrat wird von oben in die auf eine Temparatur unterhalb des Erweichungspunktes des Substratmaterials erwärmte Züchtungslösung eingebracht. Durch geeignete Heizeranordnung kann ein Temperaturgradient zwischen dem Nährsubstrat am Boden und dem Züchtungssubstrat derart eingestellt werden, dass gleichzeitig eine ausreichende Übersättigung der Nährlösung sowie konvektiver Stofftransport zum oberen Substrat realisiert wird.
Die Betrachtungen konzentrieren sich zunächst auf das Potenzial konventioneller Lösungszüchtung bezüglich erreichbarer Schichtdicken und Wachstumsraten bei niedrigen Temperaturen. Berechnungen zum thermodynamischen Gleichgewicht im binären Stoffsystem Silicium–Indium zeigen die Notwendigkeit zum konvektiven Antransport des zu wachsenden Stoffes zum Erreichen ausreichender Schichtdicken ($>50\,\mu m$). Die Verhältnisse bezüglich des Stofftransportes und der Übersättigung in der vorliegenden Züchtungsapparatur werden analysiert. Es zeigt sich, dass gelöstes Silicium mittels Einsatz einer geeigneten Heizerkonfiguration gezielt vom Nähr– zum Züchtungssubstrat transportiert werden kann. Die experimentellen Ergebnisse werden mit Hilfe einer Analyse zur Hydrodynamik diskutiert. Zusätzlich werden Finite–Elemente Simulationen zum konvektiven Transport zur Diskussion herangezogen.
Die chemische Stabilität verschiedener leitfähiger Zwischenschichten bei prozessrelevanten Temperaturen wurde durch Berechnungen im ternären Stoffsystem Molybdän, Silicium und Indium betrachtet. Auf diesen Ergebnissen basierend erfolgte die Präparation von Molybdändisilicid auf Glas durch Temperung alternierender Molybdän–Silicium Schichtpakete. Die Stabilität der so erzeugten Schichten im Kontakt mit Silicium gesättigter Züchtungslösung konnte experimentell nachgewiesen werden. Die anschließende Untersuchung des Vapor–

Liquid–Solid Prozesses auf $MoSi_2$–Schichten zeigte eine signifikante Anhängigkeit von den Parametern der Schichtpräparation sowie der Substrattemperatur während der Lösungsmittelverdampfung.

Saatkristallite wurden anschließend mit Hilfe der stationären Lösungszüchtung bei 610 °C ausgewachsen und das gezüchtete Material bezüglich Kristallinität, Orientierung und Reinheit charakterisiert. Zusätzlich standen Untersuchungen zur Morphologie im Vordergrund. Ausgewachsene Kristallite zeigen eine deutliche {111}–Facettierung. Die Ausdehnung einzelner Facetten beträgt bis zu 200 µm. Oftmals bestehen einzelne Körner aus mindestens zwei Zwillingsdomänen. Das Auftreten einer Facettierung sowie das Vorhandensein von einspringenden Kanten an Zwillingskorngrenzen sind Voraussetzungen für einen speziellen Wachstumsmechanismus, welcher hohe Wachstumsraten selbst bei geringer Übersättigung ermöglicht. Die Entstehung skellettartiger Morphologien wird mit dem Auftreten von Konzentrationsinhomogenitäten innerhalb der Diffusionsgrenzschicht erklärt. Diese führen zu ungenügender Übersättigung im Zentrum einzelner Facetten und somit zum Auftreten einer morphologischen Instabilität.

Die prinzipielle Anwendbarkeit des Prozesses zur Abscheidung von mikrokristallinem Silicium auf Glas konnte nachgewiesen werden. Allerdings verbleiben Limitierungen bezüglich des erreichbaren Bedeckungsgrades sowie der Größe unter stabilen Bedingungen gewachsener Silicium Kristallite.

Contents

1 Introduction

The investigation of deposition techniques leading to polycrystalline silicon thin films on amorphous substrates is of persistent interest for the fabrication of electronic devices. Today, wafer–based processes are well established in this field but also expensive. Taking photovoltaic as an example, here about 30–40 % of production costs of a 300 µm thick monocrystalline device are related to wafer fabrication [1]. However, considering the wavelength–dependent penetration depth, a silicon absorber layer thickness of 50 µm is already sufficient for the fabrication of high efficient solar cells [2]. For mechanical stability a solid supporting material (substrate) is essential for thin film devices. Here, low–cost materials such as ceramics or glass are gaining increased interest. Therefore, much research focuses on the investigation of growth techniques that aim at the fabrication of polycrystalline thin films on foreign substrates, that – in general – are amorphous.

Several attempts have been made within the last years to grow polycrystalline silicon on glass. Almost all of them include two main steps, that is the deposition of a seeding layer with epitaxial thickening in a second step. Various investigations have been made considering solid–phase crystallization. Thermal treatment of an amorphous silicon layer leads to small–grained polycrystalline material. Thermal energy can be introduced into the film by means of a conventional furnace [3, 4] or by laser treatment [5, 6]. Because of the high density of grain boundaries, which act as recombination centers for electron–hole pairs, such material is unsuitable for high performance devices. Larger grains with diameters of 50 to 100 µm are obtained applying the so–called aluminum–induced layer exchange process [7]. Here a vertical stack of glass/Al/Al_xO_y/a–Si is transferred into glass/µc–Si/Al_xO_y/Al(Si) by an annealing step below the eutectic temperature of the Al–Si system. The microcrystalline silicon layer acts as seeding layer for further epitaxial thickening by vapor deposition technique [8]. Main disadvantage of this technique is the high aluminum impurity incorporation in the absorber layer caused by a rather high distribution coefficient. Control of nucleation sites and therefore grain density can be achieved by photo-lithographic or laser beam pre–patterning of the substrate. However, such techniques are difficult and expensive when scaled up to large area device fabrication.

These examples illustrate the complexity of the matter. Indeed, a promising deposition technique should meet some preconditions, which can be specified as follows. It must:

- involve the application of low–cost substrates such as glass.
- exclude process temperatures above the substrate's softening or melting point.
- be fast enough to reduce fabrication costs.
- target on growth of closed polycrystalline silicon layers with a thickness of about 50–100 µm.
- aim at growth of structural and electrical high quality material.

Until now, no silicon thin film technique has been developed, which satisfies all the needs of solar industry.

The use of an amorphous substrate and the limitation of process temperature excludes the application of well established conventional epitaxial methods. Therefore, the present work focuses on joining several different methods of crystal growth in order to fit the specified needs. Physical vapor deposition is combined with solution growth technique in a hybrid process. Parts of it are subject of a European patent registered as EP 0843748.

The basic sequence is shown schematically in Figure 1.1. The first step involves the coating of a pre–cleaned borosilicate glass substrate with a conductive intermediate layer by applying physical vapor deposition. The subsequent two steps aim at deposition of silicon seed crystals by means of the vapor–liquid–solid process. Here, a non or at least partially wetting metallic solvent is deposited to form microdroplets on the surface. The sample has to be heated above the melting point of the solvent during deposition. Subsequently, silicon is deposited while the sample is heated above the eutectic temperature of the solvent and silicon. Silicon atoms reach the solvent droplets by surface diffusion and direct impingement. The silicon vapor pressure resulting from electron–beam evaporation provides the driving force for Si nucleation inside the droplets.

Subsequent enlargement of seeds is carried out by steady–state solution growth. Otherwise from conventional solution growth, which is carried out at about 900 ℃, this method makes use of temperatures below the softening point of the glass substrate. The apparatus mainly consists of a vertical stack of silicon feeding material, the solvent (indium) and the growth substrate. To overcome the problem of low solubility at low temperatures, convective transport of silicon–saturated indium from the feeding source to the growth substrate must be offered together with suitable supersaturation.

The work focuses on the analysis of the feasibility of this growth process, which might be suitable for the low–cost deposition of a polycrystalline layer. The application as an absorber layer in the field of photovoltaic is the main motivation but not the objective of this work. In fact, the intention is to clarify basic phenomena, which determine the feasibility of each partial step, as well as their successive combination. Although the process turns up to be straightforward, a detailed investigation of each step requires knowledge of various physical concepts including thermochemistry, material transport phenomena, concepts of nucleation and crystal growth, as well as wetting behavior of thin liquid films in contact with a solid substrate.
Therefore, this work starts with a short overview on theoretical aspects covering the addressed fields in Chapter 2. A more detailed survey of the deposition process is given in Chapter 3 together with the equipment applied to obtain the experimental results. Afterwards, methods, which were used to characterize the samples, are presented in Chapter 4. The theoretical considerations and actual experimental results are presented in Chapter 5. In the course of this thesis, improvements based on these results were proposed and directly implemented in the process. This leads to the necessity to present the respective discussions in the same chapter. The thesis ends with an outlook where further approaches are discussed.

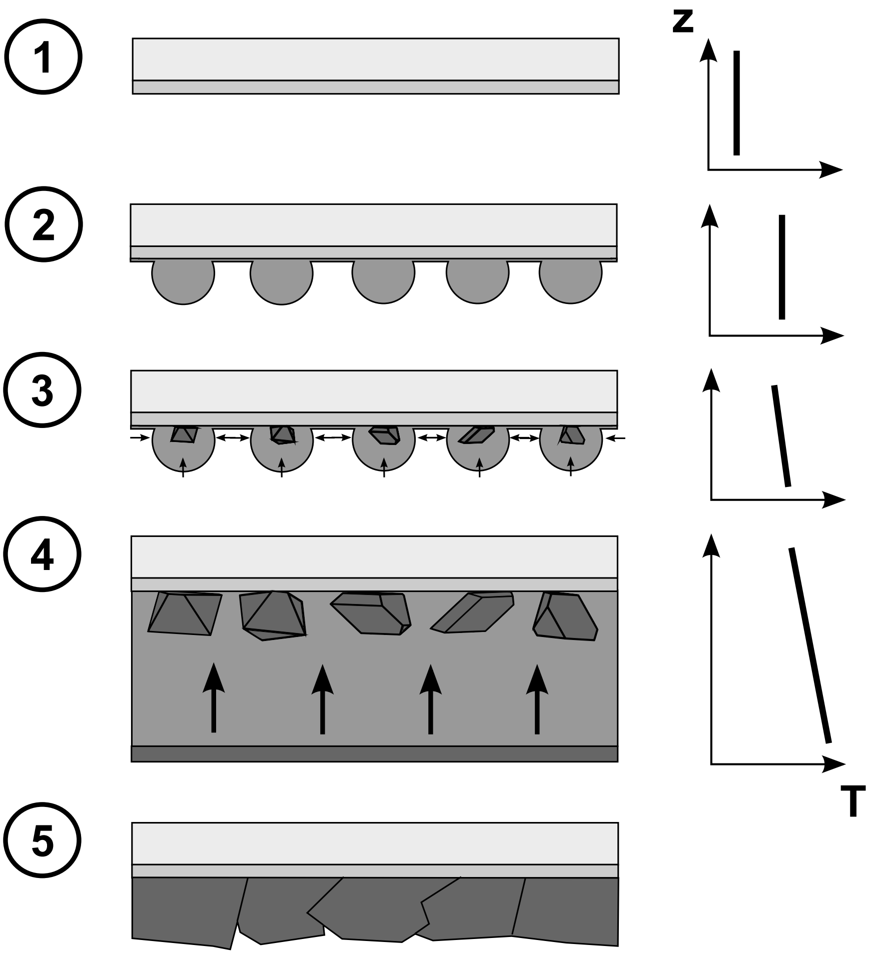

Figure 1.1: Process steps of the combined vapor–liquid–solid steady–state solution growth method to grow polycrystalline silicon on glass: (1) deposition of a conductive intermediate layer by e-beam evaporation onto the glass substrate, (2) solvent evaporation and generation of microdroplets by in situ heating of the substrate surface, (3) silicon evaporation and growth of seed crystals using the VLS method, surface heating and back side cooling, (4) enlargement of silicon using the steady–state solution growth process, (5) closed polycrystalline film.

2 Theoretical Background

To be able to discuss the potential of solution growth at low temperatures, the solubility of the growing matter has to be considered. Additionally, thermochemical relations between the substances used in processing, that is the substrate, the intermediate layer, the solute and the solvent, have to be considered. The knowledge of possible chemical reactions and their thermodynamic parameters helps to properly select the material system to be used. The second issue to consider is heterogeneous nucleation, wetting and stability of thin fluids on solid surfaces. Concepts of fluid mechanics also help to understand material transport conditions during the last step of the process. In order to classify and to discuss several common morphologies of the grown material, the underlying growth mechanisms have to be known as well.

2.1 Thermodynamic Basics of Solution Growth

Usual liquid phase epitaxy (LPE) involves growth of thin solid films from metallic solutions on crystalline substrates. The growth procedure consists of several partial steps. First, a small portion of solute A is dissolved in the metallic solvent B at temperature T_s. B gets saturated up to the equilibrium concentration at T_s. Subsequently, supersaturation and therefore a driving force $\Delta\mu_{ls}$ for crystallization is generated by cooling the solution to a temperature T_g. The supersaturated solution is brought into contact with the substrate. The growth process now includes transport to the solid–liquid interface and incorporation of matter into the crystal. In crystal growth usually pressure P, temperature T and the number of particles n are known. This set of variables forms the natural variables of the associated thermodynamic potential namely the Gibb's free energy G. The chemical potential μ_i is used to describe phase equilibrium and the driving force for crystallization. It is represented by the first partial derivative of G with respect to the number of particles n_i of component i. In equilibrium, the Gibb's free energy is at its minimum and the chemical potential of each component is equal in all phases. Starting from equilibrium calculations, which yield an expression for the solubility of silicon in liquid indium, the driving force for crystallization which is generated by a deviation from equilibrium will be quantified.

2.1.1 Phase Equilibrium and Solubility: Solution Models

The phase equilibrium between a pure solid substance A (e.g. silicon) in contact with a metallic solution (e.g. silicon in indium) will be considered in order to be able to compute the temperature dependent solubility. The chemical potential of the pure solid phase can be written as

$$\mu_A^s = \mu_A^{0,s} \tag{2.1}$$

The superscript s denotes the solid state of aggregation. $\mu_A^{0,s}$ is known as the standard chemical potential of species A. In the case of silicon LPE the solvent is built into the crystal solely at low dopant level. Therefore, solid solubility of component B in A is assumed to be negligible in the whole temperature range. For A being dissolved in liquid B, the corresponding chemical potential is

$$\mu_A^l = \mu_A^{0,l} + RT \ln x_A^l + RT \ln \gamma_A^l \tag{2.2}$$

The second term in eq (2.2) includes the configurational change of entropy due to ideal mixing of both constituents while the third term accounts for the excess interaction. This interaction is described by the introduction of the activity a_A for species A, which can be considered as an effective concentration due to the excess molecular interactions.

$$a_A = x_A \gamma_A \tag{2.3}$$

At the equilibrium, the chemical potentials in eqs (2.1) and (2.2) have to be equal for both phases. This leads to a general expression for the solubility of the solute A, x_A^l, which will be discussed in terms of several common solution models:

$$\ln x_A^l = \frac{\mu_A^{0,s} - \mu_A^{0,l}}{RT} - \ln \gamma_A^l = \frac{\Delta^{s,l} g_A^0}{RT} - \ln \gamma_A^l \tag{2.4}$$

In order to obtain an expression for the change of molar Gibb's free energy $\Delta^{s,l} g_A^0$ at temperature T, a virtual thermodynamic cycle for the transition from the solid to the liquid state is considered. It includes heating the system from T to the melting temperature of the solute $T_{m,A}$, the actual phase transformation and subsequent cooling to T [9].

$$\ln x_A^l = \int_T^{T_{m,A}} \mathrm{d}\left(\frac{g_A^{0,s}}{RT'}\right) + \frac{1}{RT}\Delta^m g_A(T_{m,A}) + \int_{T_{m,A}}^{T} \mathrm{d}\left(\frac{g_A^{0,l}}{RT'}\right) - \ln\gamma_A^l \qquad (2.5)$$

At the melting temperature, the solid and liquid phase are in equilibrium, which implies that

$$\Delta^m g_A(T_{m,A}) = 0 \qquad (2.6)$$

Using the Gibbs–Helmholtz equation written in the form for molar variables

$$\left[\mathrm{d}\left(\frac{g}{T}\right)\right]_P = \left[-\frac{h}{T^2}\mathrm{d}T\right]_P \qquad (2.7)$$

and assuming the molar heat of fusion $\Delta^{s,l}h_A^0$ being independent of temperature, eq (2.5) can be reduced to:

$$\ln x_A^l = \frac{\Delta^{s,l}h_A^0}{R}\left(\frac{1}{T_{m,A}} - \frac{1}{T}\right) - \ln\gamma_A^l \qquad (2.8)$$

Several models are applied to estimate the excess interaction enthalpy of mixing $RT\ln\gamma_A^l$. Generally, the excess term is written in the form of eq (2.9)

$$\ln\gamma_A^l \to \frac{\Delta^{mix}h_A - T\Delta^{mix}s_A}{R}\left(\frac{(1-x_A)^2}{T}\right) \qquad (2.9)$$

where $\Delta^{mix}h_A(1-x_A)^2$ refers to the molar excess heat of mixing and $\Delta^{mix}s_A(1-x_A)^2$ is the molar excess entropy of mixing. $\Delta^{mix}h_A$ and $\Delta^{mix}s_A$ can be understood as coefficients of the first non–linear term of a power series of the excess enthalpy and the excess entropy of mixing with respect to $(1-x_A)$ [10]. Therefore, they are often referred to as a and b, respectively. $(1-x_A)^2$ resembles the asymmetric nature of the excess term over the whole concentration range and ensures that the excess term vanishes for pure substances. Three common solution models can be discussed in terms of the resulting expression of eq (2.10).

$$\ln x_A^l = \frac{\Delta^{s,l}h_A^0}{R}\left(\frac{1}{T_{m,A}} - \frac{1}{T}\right) - \frac{\Delta^{mix}h_A - T\Delta^{mix}s_A}{R}\left(\frac{(1-x_A)^2}{T}\right) \qquad (2.10)$$

The first is the quasi–regular solution for which both the excess enthalpy of mixing and the excess entropy are considered to differ from zero. The case of only $\Delta^{mix}s_A$ being zero is referred to as a regular solution. For ideal solutions, both excess terms vanish in the whole concentration range, which means that $\Delta^{mix}h_A = \Delta^{mix}s_A = 0$. Usually, the solubility curve of a binary mixture is visualised in an equilibrium phase diagram, where the temperature T is drawn versus the composition (in mole fraction) x_A at constant pressure.

2.1.2 Intermediate Phases and Ternary Phase Relationships

Reactions between the constituents can occur in numerous phase relationships . The reactants are referred to as the mother phases (e.g. A and C), the reaction products are called intermediate phases ($\mathrm{A}_i\mathrm{C}_j$). Reactions can take place, when the Gibb's free energy of the mother phases is higher than that of the intermediate phases. Therefore, the Gibb's free energy of the intermediate phases has to be explicitly considered in the phase equilibrium calculation. To give an example, in the case of two mother phases A and C with one intermediate phase, the resulting binary phase diagram consist of two parts joint one by one, each respectively resembling the pure binary case of A–$\mathrm{A}_i\mathrm{C}_j$ and $\mathrm{A}_i\mathrm{C}_j$–C.

If more than two constituents have to be considered, this case is referred to as ternary, quaternary and so forth. Ternary phase equilibria are often visualised as isothermal sections through a trigonal prism, where the temperature is drawn normal to the compositions of the three constituents which are measured along the sides of a triangle. Another common presentation is derived by holding the composition of one constituent (e.g. A) fixed while drawing a pseudo–binary section through the prism relating temperature to $x_{\mathrm{B}\rightarrow\mathrm{C}}$. For the special case of the fixed composition being equal to zero, the resulting diagrams are called binary boundary phase diagrams, which necessarily have to be consistent with the three–phase region. As there is a lack of experimental data on ternary excess interaction parameters, ternary phase equilibria are predicted with the help of the phase equilibrium and phase diagram module of a software called FactSage [11]. Here, the phase equilibrium is evaluated by a Gibb's free energy minimizer which considers particular phases stored in a database.

2.1.3 Supersaturation and Nucleation

In equilibrium, the net flux of particles from one phase to another is equal to zero. Therefore, deviation from equilibrium is the essential precondition for crystal growth. This deviation generates the driving force for crystallization which is given by the difference of the chemical potential of the ambient and the crystalline phase. In solution growth, this deviation is often generated by cooling a saturated liquid from a temperature T_s to T_g. Growth can be achieved in a certain temperature region without generating nuclei in the ambient phase. This region defines the metastable Oswald–Miers region. In this region, the composition of the solution is not changed during cooling and thus the chemical potential of the solute at $T_g < T_s$ can be written in the form of

$$\mu^l\left(T_g\right) = \mu^{0,l} + RT_g \ln\left[a(T_s)\right] \tag{2.11}$$

The chemical potential of the crystalline phase at T_g equals the equilibrium potential of the solute at this temperature:

$$\mu^s\left(T_g\right) = \mu^{l,eq}\left(T_g\right) = \mu^{0,l} + RT_g \ln\left[a(T_g)\right] \tag{2.12}$$

It follows that for the difference of the two potentials and thus the driving force for crystallization from solutions the following equation holds:

$$\Delta^{l,s}\mu\left(T_g\right) = RT_g \ln\left[\frac{a(T_s)}{a(T_g)}\right] = RT_g \ln\left[\frac{x(T_s)}{x(T_g)}\right] + RT_g \ln\left[\frac{\gamma(T_s)}{\gamma(T_g)}\right] \equiv \Delta^{l,s}\mu^{id} + \Delta^{l,s}\mu^{e} \tag{2.13}$$

Two terms contribute to the driving force for crystallization in a non–ideal solution. The first term resembles the driving force of a supersaturated ideal solution. The second term modifies this by means of the excess interaction. Often, the supersaturation is given as a dimensionless quantity σ which is defined as

$$\sigma = \frac{\Delta^{l,s}\mu}{RT_g} \tag{2.14}$$

An equivalent description of the driving force of a non–ideal supersaturated solution can be derived in terms of temperatures. In contrast to the driving force of an undercooled pure substance, the molar heat of fusion has to be replaced by the molar heat of dissolution and the melting temperature by T_s. The result is a formula which formally equals the description of the driving force in melt growth (with $T_s \rightarrow T_m$):

$$\Delta^{l,s}\mu = \left(\Delta^{s,l}h_A^0 + \Delta^{mix}h_A(1-x_A)^2\right)\left(1 - \frac{T_g}{T_s}\right) \tag{2.15}$$

The driving force for crystallization can be achieved by either cooling the saturated liquid or add solute particles to the saturated liquid or by a combination of both. This is clarified in Figure 2.1 where two equivalent paths reaching the same deviation

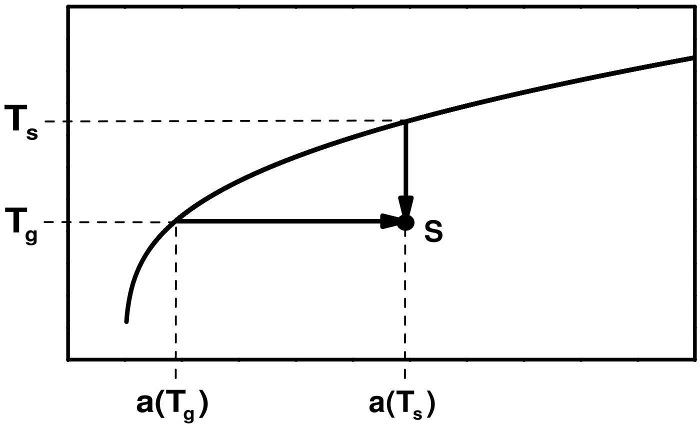

Figure 2.1: Plot of temperature T versus activity a with two thermodynamically equivalent paths to gain the same driving force for crystallization.

from equilibrium are shown.

In the case of the ambient phase being a supersaturated vapor, a relationship which is similar to eq (2.13) holds for the driving force of crystallization:

$$\Delta^{v,s}\mu = RT_g \ln\left[\frac{p}{p_0}\right] = \Delta h_{ev}\left(1 - \frac{T}{T_s}\right) \tag{2.16}$$

Here p_0 is the equilibrium vapor pressure of the growing matter, p the actual vapor pressure and Δh_{ev} denotes the molar heat of evaporation. Non–ideal behavior is considered by introducing the fugacity f in a similar way as the activity a.

If the critical supersaturation is exceeded, stable nuclei of the thermodynamic stable phase will start to grow. If nucleation starts at certain preferential sites such as phase boundaries or impurities, this is called heterogeneous nucleation. Additionally, if the nucleation site is of the same material as the growing matter, this is called homo-epitaxy. The process is referred to as homogeneous nucleation if nuclei are fully enclosed by the nutrient phase. In this case, the formation of nuclei or clusters of i particles leads to a change of the Gibb's free energy according to eq (2.17) [12].

$$\Delta G^N = -\Delta\mu i + b\gamma i^{2/3} \tag{2.17}$$

The first term describes the Gibb's free energy that is released due to the formation of the new, stable phase and is therefore proportional to the number of particles i in the nucleus and the corresponding reduction of Gibb's free energy per added

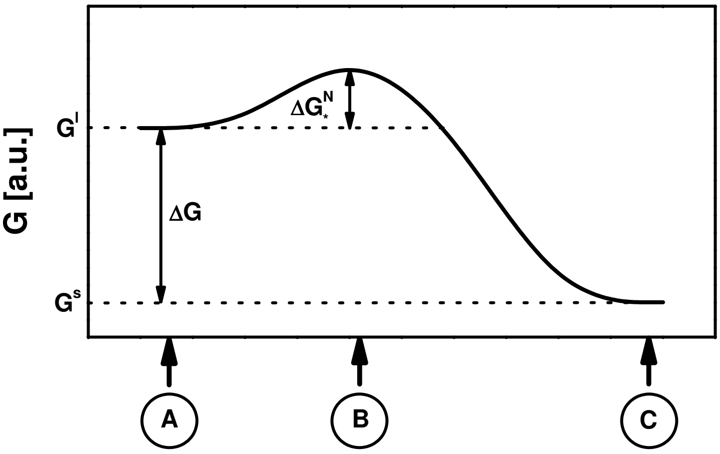

Figure 2.2: Scheme showing the principle of Gibb's free energy minimization with nucleation barrier; (A)–initial, supersaturated state, (B)–activated state, (C)–final state (crystal).

particle $\Delta\mu$. In addition, a new interface with the energy γ between the nutrient phase and the nucleus is generated. The geometry of the interface as determined by the shape of the nucleus is considered by the factor b. The sum of both contributions as depicted in eq (2.17) yields a curve with a single maximum when plotted against i or r, respectively. This maximum defines the critical cluster size i_* or r_*. The energy associated with the critical cluster size is the activation energy for nucleation ΔG_*^N. Clusters of size below i_* tend to dissolve in order to minimize the free energy, whereas clusters with size above i_* will tend to grow. Assuming a spherical nucleus of radius r eq (2.17) can be written as

$$\Delta G^N = \frac{4\pi}{3}\frac{r^3}{\Omega}\Delta^{l,s}\mu + 4\pi r^2\gamma \tag{2.18}$$

Ω denotes the atomic volume of the crystallizing species. The associated radius of the critical nucleus is given by

$$r_* = \frac{2\gamma\Omega}{\Delta^{l,s}\mu} \tag{2.19}$$

The energetic path of nucleation can be schematically shown as depicted in Figure 2.2. A system in the supersaturated, initial state has to overcome an energy barrier of ΔG_*^N in order to reach the final state. As this process is thermally activated, the corresponding nucleation rate j follows an Arrhenius–law

$$j(T) \propto \exp\left(-\frac{\Delta G_*^N}{kT}\right) \tag{2.20}$$

where k is the Boltzmann constant and T refers to the temperature.

2.2 Material Transport in Crystal Growth

In most cases, crystal growth includes transport of the growing matter through a fluid (gas or liquid) towards the growing interface. If this transport is slow compared to the kinetics at the interface, it becomes the bottleneck of the process. Vice versa, the growth rate is controlled by attachment kinetics if transport is fast compared to the interface kinetics.

In order to discuss the transport phenomena, a finite volume of a multicomponent fluid is considered [13]. The average velocity of a species i in this volume is given by the sum of the individual velocities of the n_i particles:

$$\mathbf{v}_i = \frac{1}{n_i}\sum_{j=1}^{n_i}\mathbf{v}_{ij} \tag{2.21}$$

If the $\mathbf{v}_i$ are equal for all species, transport is solely driven by convection. An additional relative motion of one component with respect to another is called diffusion. The total mass flux of a component $\mathbf{j}_i$ can therefore be written in terms of two contributions, a bulk flow (convective) velocity and a diffusive flux:

$$\mathbf{j}_i = \rho_i\mathbf{v} + \mathbf{j}_i^{\mathrm{diff}} \tag{2.22}$$

ρ_i is the local mass density of species i. Both phenomena will be discussed in brief as both play a notable role for material transport in the system under consideration in this work.

2.2.1 Diffusion

From a thermodynamic point of view, the driving force for isothermal diffusion is a gradient in the thermodynamic potential of the diffusing matter. In a two component system the diffusive flux of species i, $\mathbf{j}_i^{\mathrm{diff}}$, is related to this gradient by

$$\mathbf{j}_i^{\mathrm{diff}} = -L_i\nabla\mu_i \tag{2.23}$$

Here L_i is a transport coefficient. In the special case of an isobaric system without external fields and forces, the chemical potential is a function of the concentration as seen in eq (2.11). The concentration will be referred to as c. In this case, the diffusive flux can be written as:

$$\mathbf{j}_i^{\mathrm{diff}} = -D_{c,i} \nabla c_i, \quad D_i = L_i \frac{RT}{c_i} \tag{2.24}$$

This is Fick's first law for diffusion driven by a concentration gradient. Generally, the diffusion coefficient D_c depends on the materials involved, on the temperature and on the pressure. For bulk diffusion of a solute in liquids, D_c can be derived by the Stokes–Einstein relation in the following way (subscript i dropped) [14]:

$$D_c^{\mathrm{liq}} = \frac{kT}{6\pi\eta R_0} \tag{2.25}$$

Here, k is the Boltzmann constant, T is the temperature, η the dynamic viscosity of the solvent and R_0 the hydrodynamic radius of the solute.
At solid surfaces and in solids, two–dimensional diffusion is conducted by jumps of atoms between adjacent potential minima. For each jump, an energy barrier has to be overcome. This process is thermally activated and the associated activation energy is W. In this case, the diffusion coefficient depends on temperature as in an Arrhenius–law:

$$D^{\mathrm{sol}} = D_0 \exp\left(-\frac{W}{kT}\right) \tag{2.26}$$

By considering the mass conservation law in the form of the continuity equation, one can derive Fick's second law in the form of eq (2.27).

$$\frac{\partial c}{\partial t} = \nabla \left(D \nabla c\right) \tag{2.27}$$

In two dimensions the associated diffusion length L can be estimated by using eq (2.28) [15].

$$D = \frac{L^2}{4t} \tag{2.28}$$

2.2.2 Convection

Approximately, convective flow is considered as being independent from diffusion, i.e. the fluid is considered to consist of a single component only. A further simplification is derived by assuming the fluid to be incompressible, which means that the density ρ remains constant in a fixed control volume. Convection is described by a system of four equations, the continuity equation (2.29) and the three Navier–Stokes equations (2.30) for uncompressable fluids.

$$\frac{\partial \rho}{\partial t} = -\rho \nabla \mathbf{v} = 0 \tag{2.29}$$

$$\rho \frac{\partial \mathbf{v}}{\partial t} = -\rho(\mathbf{v} \cdot \nabla)\mathbf{v} - \nabla p + \eta \nabla^2 \mathbf{v} + \mathbf{f} \tag{2.30}$$

Here, $\mathbf{v} = \mathbf{v}(\mathbf{x})$ is the flow velocity (see eq (2.22)), t is the time, p is the pressure, η the dynamic viscosity, and $\mathbf{f}$ is volume density of additional body forces (see Section 2.4.2). The Navier–Stokes equations relate the time derivative of the velocity field to the sum of inertial forces, pressure forces, viscous forces, and additional body forces. The latter ones may arise due to gravity, external fields or small–size–effects as discussed in Section 2.4.2. In order to be able to derive solutions for eqs (2.29) and (2.30), suitable boundary conditions for the considered volume Ω have to be specified. Particles stick at the wall by adhesion. This results in a fully stagnant layer with a thickness of few molecular distances. With increasing distance from the wall, flow velocity gradually changes from zero to the bulk flow velocity. In the case of forced convection, bulk flow is dominated by inertial forces while in the boundary layer fluid behavior is determined by the viscous forces. In the case of a rigid, non–reacting solid boundary $\partial\Omega$ being wetted by the fluid, the Dirichlet boundary condition can be formulated as the so called no–slip condition for viscous flow:

$$\mathbf{v}(\mathbf{x}) = 0 \quad \forall \mathbf{x} \in \partial\Omega \tag{2.31}$$

In order to identify the significance of viscous forces in relation to the inertial force, the ratio of both is introduced in the following way:

$$\frac{\text{inertial force}}{\text{viscous force}} = \frac{\rho(\mathbf{v} \cdot \nabla)\mathbf{v}}{\eta \nabla^2 \mathbf{v}} \approx \frac{\rho V V/L}{\eta V/L^2} = \frac{\rho V L}{\eta} = \frac{V L}{\nu} \equiv Re \tag{2.32}$$

Here, V is the free–stream velocity far from any boundaries, ν is the kinematic viscosity and L is a characteristic length-scale of the system. The ratio is known as the Reynolds–Number of the system. Hence, for large Reynolds–Numbers, the flow velocity field may be divided into two zones, one (inviscid) far beyond the boundaries and the afore mentioned boundary layer region. For flow parallel to a flat plate with the edge at $x = 0$, the thickness δ_m of the momentum boundary layer can be estimated by [16]

$$\delta_m \cong 5\sqrt{\frac{x\eta}{V\rho}} \tag{2.33}$$

This equation also holds for flow driven by buoyant forces with the respective bulk flow velocity. In crystal growth, not only the flow velocity field adjacent to the growing surface but also the temperature and solute distribution near the interface are of interest. In these cases, the concept of a boundary layer is applicable, too. The particular thickness of the thermal and the solute boundary layers (δ_T and δ_c) are related to the thickness of the momentum boundary layer in the following manner [17]:

$$\delta_c/\delta_m \sim Sc^{-1/3} = (D_c/\nu)^{1/3} \tag{2.34}$$

$$\delta_T/\delta_m \sim Pr^{-1/3} = (D_T/\nu)^{1/3} \tag{2.35}$$

Here the Schmidt number Sc and the Prandtl number Pr give the ratio of kinematic viscosity to solutal diffusivity and thermal diffusivity, respectively.

Free convection is driven by either buoyancy or gradients in surface tension. The former is caused by differences of the local mass density which arise for example due to thermal or solutal expansion. The volume density of the additional body force $\mathbf{f}$ (see eq (2.30)) can be written as

$$\mathbf{f} = \rho\mathbf{g} = \rho_0\left[1 - \beta(T - T_0) - \beta'(c - c_0)\right]\mathbf{g} \tag{2.36}$$

In eq (2.36) $\mathbf{g}$ is the acceleration due to gravity, β is the thermal and β' the solutal expansion coefficient. In the framework of the Boussinesq–approximation the density variation is only considered in the buoyancy–term (2.36) of eq (2.30), where exclusively gravitational acceleration acts as a body force. As a high viscosity η and a high thermal conductivity κ both tend to slow down fluid motion, below a certain critical density gradient the system stays at rest. To estimate the parameters for the onset of steady convection, a horizontally infinite fluid under a vertical temperature gradient heated from below is considered. A linear stability analysis of the Navier–Stokes equations for this configuration (see for instance [13]) yields the stability criterion being dependent on the value of the dimensionless temperature or concentration gradient given by

$$Ra = \frac{\beta g \Delta T L^3}{\nu D_T}, \qquad Ra' = \frac{\beta' g \Delta c L^3}{\nu D_c} \tag{2.37}$$

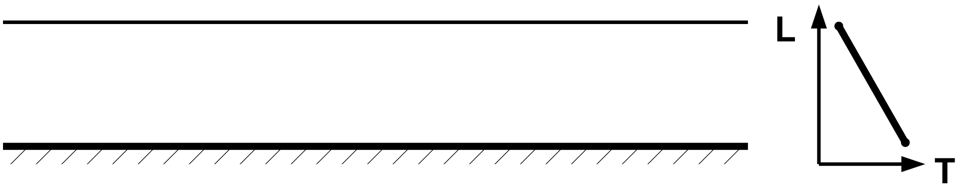

Figure 2.3: Fluid configuration for estimation of the critical Rayleigh number.

If the so–called Rayleigh–Number exceeds a certain critical value, steady convection is expected to set in. If the upper surface of the fluid is free (no no–slip condition) the critical Rayleigh number is 1101 [13]. A horizontal temperature gradient immediately gives rise to threshold-less convection which causes the fluid to drift upwards in the hotter zone and downwards in the colder zone.

In order to estimate the influence of convective heat transfer compared to heat transfer by conduction, one introduces the Prandtl number, which is the ratio of viscosity to thermal conductivity. The ratio of the Rayleigh number and the Prandtl number defines the Grashof number, which in turn gives the ratio of inertial and buoyant to viscous forces.

$$Gr = \frac{g\beta\Delta T L^3}{\nu^2}, \qquad Gr' = \frac{g\beta'\Delta c L^3}{\nu^2} \tag{2.38}$$

With all these numbers at hand, a characterization of the fluid flow behavior is possible even without having to solve eqs (2.29) and (2.30).

2.3 Crystal Faceting and Modes of Crystal Growth

Growth of a crystal can be described by the advance of elementary steps present at the interface between the nutrient phase and the crystal. The elementary step itself spreads over the surface mainly by incorporation of growth units at existing kink sites. A growth unit can either be a single atom or a cluster of them. The total mass flux to the step is given by [18]

$$j = \rho v_{step} = \beta(c - c_{eq}) \tag{2.39}$$

Here, ρ is the mass density of the growing matter, v_{step} is the step velocity, c and c_{eq} the actual and the equilibrium solute concentration and β is the kinetic coefficient.

Two effects contribute to the kinetic coefficient of a surface, first is the kink density and second is the attachment kinetics at the kink sites. The kinetic contribution is given by the attachment frequency ν_+ and detachment frequency ν_- of growth units.

$$\beta = \frac{a^2}{\lambda_0}(\nu_+ + \nu_-) \tag{2.40}$$

a denotes the length of a growth unit and λ_0 is the inter-kink distance. Generally, the kinetic coefficient is a function of the crystal orientation and the driving force. Let $\mathbf{n}$ be the vector normal to an arbitrary crystal direction and $\Delta^{l,s}\mu$ the driving force for crystallization. The growth rate normal to the surface is given by

$$R = \beta(\mathbf{n}, \Delta^{l,s}\mu)\Delta^{l,s}\mu \tag{2.41}$$

For a slightly miscut vicinal surface (see below), the kinetic coefficient is related to the step kinetic coefficient β_{st} by

$$\beta \approx \beta_{st}|p| \tag{2.42}$$

when $|p|$ is the slope of the vicinal surface (see [18]).

In order to discuss the different modes of crystal growth, the sources for elementary steps have to be considered.

2.3.1 Sources of Elementary Steps

Several physical and morphological phenomena contribute to the formation of elementary steps. First, morphological roughness in the absence of thermal or kinetic roughening ($T = 0, \Delta\mu = 0$) will be discussed. In 1955, Hartman and Perdok were the first who figured out the relationship between the strength of bonds in the crystal and its morphology [19]. They defined periodic arrangements of such bonds as *periodically bonded chains* with their directions as P.B.C. vectors. Following the definition of P.B.C.'s, the energy gain attributed to the attachment of a growth unit to the chain is maximal. Therefore, the authors postulated that the maximum growth velocity must occur parallel to the P.B.C.'s as growth must be preferred in these directions. Three different types of crystal faces can be deduced from these definitions. The first is the F–face, which contains at least two non–parallel chain vectors and is defined as being "flat". Faces containing exactly one chain–vector are called S–faces and exhibit steps which are aligned parallel to the P.B.C. direction. Finally, faces that exhibit no specific relationship to a bond–chain are called K-faces and are assumed to be morphologically rough or *kinked.* Below the roughening transition, attachment of a new growth unit is preferred at K–faces, likely at S–faces and very difficult at F–faces. For a given crystal structure, the nature of the faces can be classified by introducing the orientation–dependent kink–density function following the continuum approach Suchtelen and Veenendaal suggested in 2000 [20].

For $T > 0$ and $\Delta\mu = 0$ thermal roughness has to be taken into account. Per se, the elementary step can be considered as being thermally rough even at room temperature (see [21]). Therefore, present S–faces are expected to be kinked and being of minor importance for the shape of the grown crystal. To decide, whether an F–face is thermally rough, Jackson's criterion can be consulted [22]:

$$T_R = \frac{\Psi_{hkl}}{\Psi}\frac{\Delta^{l,s}h}{R}\frac{1}{\alpha} \tag{2.43}$$

Here, Ψ_{hkl}/Ψ is the ratio of the binding energy of a growth unit at the surface and the total binding energy of the growth unit in the bulk crystal. $\Delta^{l,s}h = \Delta^{s,l}h^0 + \Delta^{mix}h(1-x)^2$ is the molar heat of dissolution and α is known as the Jackson factor. T_R is the temperature of the roughening transition and corresponds to $\alpha = 2$.

Growth of morphologically and thermally flat interfaces must be driven by defects (see below) or by a mechanism, which is often referred to as “birth–and–spread” [23, 24]. The latter involves the generation of supercritical two–dimensional nuclei induced by a sufficient supersaturation ($T > 0, \Delta\mu > 0$), and the formation of the new atomic layer is accompanied by the formation of a new elementary step. To determine the change in Gibb's free energy associated with this process, the second term in eq (2.17) has to be modified and involves the step free energy instead of the surface free energy:

$$\Delta G_{2D}^{N} = -\Delta\mu i + c\gamma_{step} i^{1/2} \tag{2.44}$$

c denotes a geometrical factor and depends on the shape of the two dimensional nucleus.

2.3.2 Modes of Crystal Growth

Depending on supersaturation (see above), growth of crystals can be described by means of different models. For low supersaturation, Burton, Cabrera and Frank [21] found growth of a flat interface to be controlled by the presence of a self–preserving elementary step. This step is usually provided by a screw dislocation. In solution growth, the growth rate R depends on supersaturation $\sigma = \Delta^{l,s}\mu/kT$ as written in

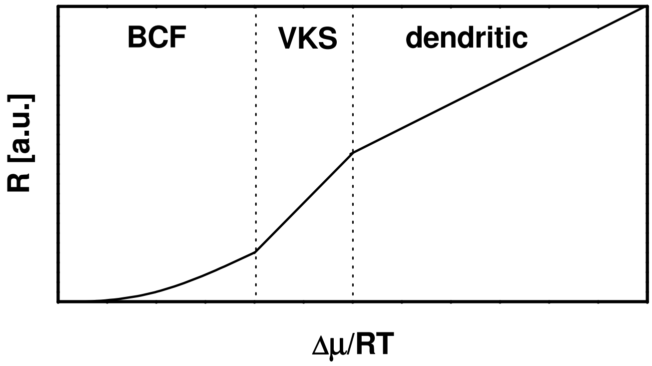

Figure 2.4: Growth rate R versus supersaturation for three different growth mechanisms: spiral, 2D–nucleation and adhesive (see [25, 26]).

eq (2.45) [16].

$$R^{\mathrm{BCF}} \propto \frac{\sigma^2}{\sigma_0} \frac{1}{\ln\left[\frac{\delta_m}{\pi a}\frac{\sigma_c}{\sigma}\sinh\left(\frac{\sigma}{\sigma_c}\right)\right]} \tag{2.45}$$

Here, σ_c is a characteristic supersaturation, a the height of the elementary step and δ_m the thickness of the stagnant boundary layer (see Section 2.2.2). Higher supersaturation enables two–dimensional nucleation on flat surfaces. Volmer, Kossel and Stranski were the first to describe the growth rate associated with this process to be non–linearly correlated with supersaturation. In the case of layer–by–layer growth, the growth rate can be expressed in terms of eq (2.46)

$$R^{\mathrm{VKS}} \propto \sqrt{\sigma}\exp\left[-\frac{const.}{(kT)^2\sigma}\right] \tag{2.46}$$

At rough interfaces, every growth unit which reaches the interface is instantaneously built into the crystal. The growth rate in this case is proportional to the supersaturation and crystals exhibit a high density of dendrites.

$$R^{\mathrm{Dend.}} \propto \sigma \tag{2.47}$$

Comparatively little theoretical work has been carried out on twin–assisted growth. Re–entrant edges formed by two facets at twin boundaries can act as a self–-preserving source for elementary steps, which can afterwards propagate onto the facets. Growth rate can be expected to be in the order of that in spiral growth, allowing twinned crystals to grow even at low supersaturation. Twin assisted growth

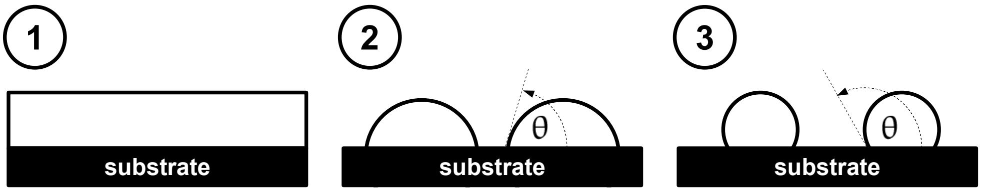

Figure 2.5: Illustration of a (1) wetting ($\theta = 0$), (2) partially wetting, and (3) non-wetting thin liquid film.

will be shown to play an important role in low–temperature solution growth of silicon from indium solutions.

2.4 Formation of Thin Fluid Films

2.4.1 Classical Nucleation Theory

The case of a structureless and flat solid substrate in contact with a supersaturated vapor will be considered. The solid substrate is hereby heated above the melting point of the vapor species, thus liquid nuclei are expected to form at the surface. The equilibrium shape of the liquid droplets is assumed to resemble a segment of a sphere with the radius of curvature being R. The contact angle θ can be derived by Young's equation [27]:

$$\gamma_s = \gamma_{l,s} + \gamma_l \cos(\theta) \tag{2.48}$$

Here γ_s, γ_l and $\gamma_{l,s}$ are the specific surface energies of the solid substrate, the liquid, and the liquid–solid interface, respectively. Depending on the numerical value of θ the liquid is said to be wetting ($\theta = 0$), partially wetting ($0 < \theta \leq \pi/2$), and non–wetting ($\pi/2 < \theta \leq \pi$). Introducing the spreading parameter S in the form

$$S = \gamma_s - \gamma_{l,s} - \gamma_l \tag{2.49}$$

enables the latter cases of wetting ($S > 0$) and non–wetting ($S \leq 0$) to be easily distinguished. The Gibb's free energy of formation of a liquid droplet ΔG is given by

$$\Delta G = -i\Delta\mu + 2\pi R^2(1-\cos\theta)\gamma_l + \pi R^2 \sin^2\theta(\gamma_{l,s} - \gamma_s) \tag{2.50}$$

where i is the number of particles in the cluster. The last two terms describe the total surface energy of the liquid droplet. The critical droplet size can be determined in a similar way as described in Section 2.1.3. For the associated work of droplet formation, the following relationship holds [16]:

$$\Delta G_* = \frac{16\pi}{3} \frac{\gamma_l^3 v_l^2}{\Delta\mu^2} \Phi(\theta) \tag{2.51}$$

Here, v_l is the volume of one particle in the liquid and $\Phi(\theta) = 0.25(1 - \cos\theta)^2(2 + \cos\theta)$ includes the contact angle and therefore takes the influence of the substrate on droplet formation into account. The nucleation rate is given by eq (2.20) and can be written in terms of temperatures as follows:

$$J = C_1 \exp\left(-\frac{C_2}{T\left(\frac{T}{T_s} - 1\right)^2}\right) \tag{2.52}$$

Here, C_1 and C_2 are constants which depend on the material system, T is the actual temperature of the substrate, and T_s is the temperature of the vapor source.

2.4.2 Stability of Thin Liquid Films on Solid Surfaces

In order to be able to decide whether there should exist a wetting layer between macroscopic droplets on a solid substrate or not, the equilibrium and dynamics of thin liquid films will be discussed in terms of the continuum approach, which was mainly developed by Sharma [28]. The solid substrate will be referred to as material **1**, the liquid as material **2** and the surrounding gas phase as material **3**. In ultra–thin (10–1000 Å) liquid films, additional body forces have to be explicitly taken into account in order to determine the wetting behavior. When considering the Gibb's free energy per unit area G of a thin liquid film of height h, besides the surface and interfacial energies γ_l and $\gamma_{l,s}$, an excess interaction term $\Delta G(h)$ which arises due to the small size has to be added. There are two types of interaction contributing to $\Delta G(h)$, namely the (apolar) van der Waals interaction ΔG^{LW} between both interfaces and the polar interaction ΔG^P. There are three types of dipole interaction contributing to the apolar forces: interaction between permanent dipoles (Keesom), between permanent and induced dipoles (Debye) and between induced dipoles (London). The height–dependence of the apolar interaction can be described by means of the effective Hamaker constant A in the following way [29]:

$$\Delta G^{LW} = -\frac{A}{12\pi h^2} \tag{2.53}$$

This equation was derived by Hamaker by summing up the pairwise interaction for each atom and for each type of interaction. The Hamaker constant is related to the dielectric function of all three materials and can be approximated by applying the Tabor–Wintership relation. The cutoff distance of the interaction due to Born repulsion is given by $d_0 \approx 1.58\,\text{Å}$. $\Delta G^{LW}(d_0)$ is the change of Gibb's free energy when bringing two semi–infinite bodies of material **1** and material **3** from infinity to d_0. Having this in mind, $\Delta G^{LW}(d_0)$ can be expressed in terms of the specific surface energies as

$$\Delta G^{LW}(d_0) = \gamma_s^{LW} - \gamma_{l,s}^{LW} - \gamma_l^{LW} \equiv S^{LW} \tag{2.54}$$

Therefore, ΔG^{LW} can be determined by one macroscopic parameter, i.e. the spreading coefficient S^{LW}:

$$\Delta G^{LW} = S^{LW} \frac{d_0^2}{h^2} \tag{2.55}$$

The polar (ionic, acid–base) interaction is usually described by introducing a correlation length l and can be written as

$$\Delta G^P = S^P \exp\left[(d_0 - h)/l\right] \tag{2.56}$$

where S^P is the polar part of the spreading parameter. The total excess Gibb's free energy per unit area is

$$\Delta G(h) = S^{LW} \frac{d_0^2}{h^2} + S^P \exp\left[(d_0 - h)/l\right] \tag{2.57}$$

The first derivative of $\Delta G(h)$ with respect to h equals the total excess energy per unit volume Φ and is referred to as the negative of the disjoining pressure. The term $\mathbf{f} = (-\nabla\Phi)$ acts as an additional body force and has to be explicitly considered in the Navier–Stokes equation (2.30). Generally, gravity can be neglected in thin film fluid dynamics. Equation (2.57) relates the excess Gibb's free energy per unit area of a nanoscopic film with the spreading parameter, which can be derived from the macroscopic wetting angle.

If both, the polar and the apolar forces are solely attractive for all film heights h, the afore mentioned Born repulsion has to be explicitly taken into account in order to remain consistent with the definitions above. By a summation of pairwise

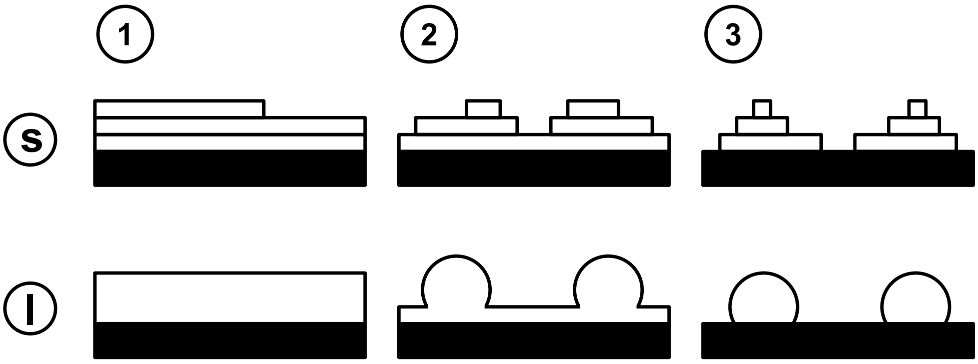

Figure 2.6: The modes of droplet formation compared to epitaxial growth mechanisms: (1) – Frank-van der Merwe (layer–by–layer), (2) – Stranski–Krastanov, (3) – Volmer–Weber (island growth).

Lennard–Jones interaction, Sharma derived [30]

$$\Delta G_{Born}(h) = \frac{27}{256}|S^{LW}|\frac{d_0^8}{h^8} \tag{2.58}$$

In 1993 the same author developed an instability criterion by analyzing the equilibrium shape of a thin liquid film with a mean thickness of h_0 under a small perturbation with a characteristic wavenumber k_c, which reads as

$$k_c^2 = -\frac{1}{\gamma_l}\left(\frac{\mathrm{d}\Phi}{\mathrm{d}h}\right)_{h=h_0} \tag{2.59}$$

This relation gives the necessary condition for thin film instability, i.e. de–wetting and droplet formation, which can be expressed in terms of the second derivative of the excess Gibb's free energy of the film:

$$\left(\frac{\mathrm{d}^2\Delta G}{\mathrm{d}h^2}\right)_{h=h_0} < 0 \quad \longleftrightarrow \quad \text{dewetting} \tag{2.60}$$

A system is referred to as being apolar if at least two of the three materials involved are apolar. In this case, only the van der Waals interaction has to be considered ($S^P = 0$), and eq (2.60) resembles the condition for droplet formation as derived in the previous section:

$$S^{LW} < 0 \quad \longleftrightarrow \quad \text{dewetting} \tag{2.61}$$

On the other hand, in apolar systems the existence of macroscopic drops with a finite contact angle ensures instability of the related thin liquid film. In the polar regime ($S^{LW} \neq 0, S^{P} \neq 0$) the algebraic sign of the left term in eq (2.60) can change with film thickness h_0. In this case, macroscopic droplets are stable in equilibrium with a thin wetting layer between them. The third case involves full wettability and both microscopic as well as macroscopic films remain stable under small perturbation. Figure 2.6 summarizes the above mentioned possibilities and emphasizes the analogy to growth modes in epitaxial crystal growth. In Stranski–Krastanov mode additional strain and/or dislocation energy stabilizes the thin layer between islands. In the case of liquids, the above discussed excess energy of polar and apolar interaction is responsible for the existence of the wetting layer.

3 Experimental Setup and Sample Processing

The use of glass as a potentially low–cost substrate for silicon deposition leads to two major requirements. As glass being an amorphous material, direct epitaxial growth is impossible because crystal lattice information are not available. One approach to overcome this problem is to start with the deposition of small seed crystals or a thin seeding layer prior to further epitaxial thickening. In addition to the necessity to form seed crystallites, overall process temperature is limited due to the softening point of the used glass substrate.

This chapter gives an overview on the equipment used for the growth experiments and the process sequence including the respective basic parameters.

3.1 Experimental Setup

Figure 3.1 shows a scheme of the cluster of high vacuum chambers used to perform the experiments for this work. The cluster tool is composed of four process chambers and four transfer chambers. The process chambers include an ion etching equipment, a high vacuum deposition chamber, an ultra high vacuum deposition chamber and the steady–state growth apparatus. Only the high vacuum deposition chamber and the steady–state growth apparatus were used for this work.

3.1.1 The High Vacuum Physical Vapor Deposition Chamber

The high vacuum deposition equipment allows the deposition of silicon, molybdenum and indium by means of electron beam evaporation and evaporation by resistive heating. Both evaporation stages are situated within the bottom part of the chamber. Indium has a higher vapor pressure compared to silicon and molybdenum. For that reason, resistively heated evaporation is a suitable technique to achieve satisfactory deposition rates in the case of indium (see Figure 3.2). Silicon and molybdenum are deposited using the electron beam evaporator. Both materials are

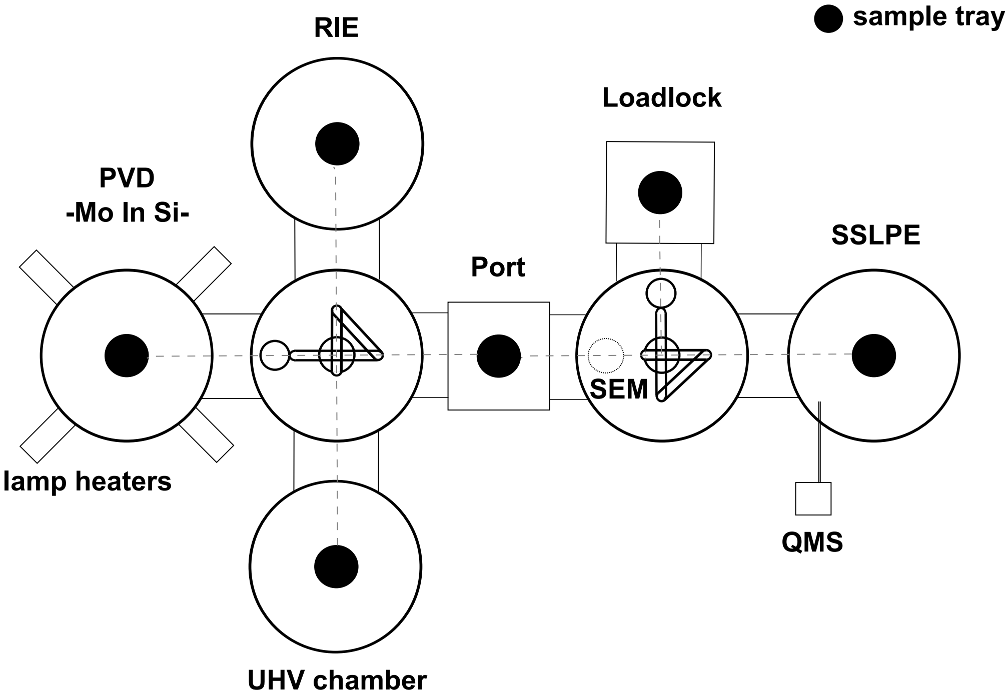

Figure 3.1: Schematic drawing of high vacuum cluster used for growth of polycrystalline silicon on glass.

separately stored in a four–pocket gun rotation stage. Besides the well determined exponential increase with temperature, the evaporation rate highly depends on the shape of the source material. The morphology of the material changes during deposition due to the evaporation. Therefore, the heating power has to be slightly adjusted from time to time to achieve rather constant deposition rates. Typical values for the operation current of the resistive heater were 90–100 A, the electron beam evaporator was operated at 8 kV BIAS voltage and typically 160 mA (molybdenum) and 70–120 mA (silicon).

The sample itself is mounted in top–down position in the upper part of the chamber on a water cooled sample stage that can be rotated. The distance between the evaporation source and the sample amounts to 40 cm. The deposited mass ratio per unit area on the sample is related to the distance r and the angle θ of the surface normal to the evaporation source by [31]

$$\frac{\mathrm{d}m}{\mathrm{d}A} \propto \frac{\cos(\theta)}{R^2} \tag{3.1}$$

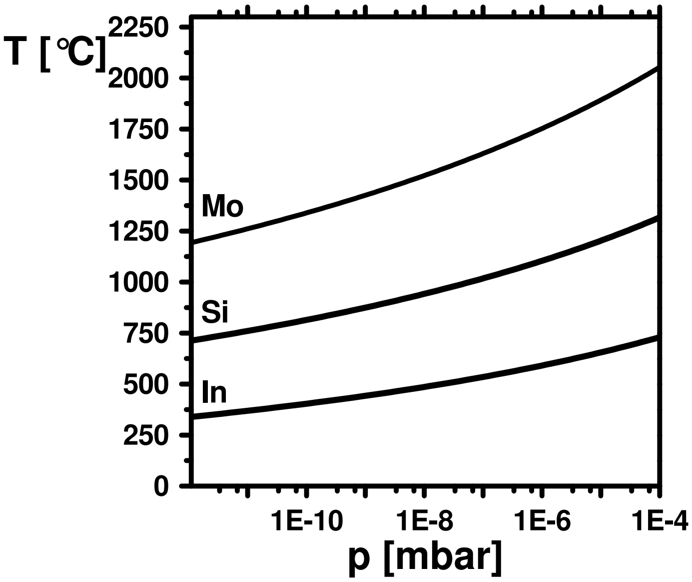

Figure 3.2: Equilibrium vapor pressures for silicon, indium and molybdenum as derived using FactSage [11].

Therefore, the rather large distance leads to a high thickness homogeneity on the typical $4 \times 4\,\mathrm{cm}^2$ substrate ($\delta d < 1\,\%$). However, a large portion of the evaporated material is deposited onto the chamber walls. The efficiency of the implemented sample support backside cooling can be increased by introducing gaseous helium between the sample support and the carrier. A flow rate of 8.3 sccm was seen to significantly decrease sample temperature by about 10 K. The sample stage can be heated by four halogen lamps mounted at the lower part of the chamber. The light is directed towards the sample, and is absorbed by the deposited layer, the substrate, and the surrounding sample holder. The ability of the layer to absorb the incident light, and therefore the efficiency of this heating method, depends on the deposit material and its thickness. The rotation of the sample stage increases the homogeneity of the temperature distribution. By heating the sample from the bottom and cooling it from the top, a temperature gradient can be established.

The deposition rate is measured using a quartz crystal microprobe which operates at a base frequency of 6 MHz and is mounted in direct vicinity of the sample holder. The thickness and the deposition rate resolution is limited to $\pm 1\,\mathrm{Å}$ and $\pm 0.1\,\mathrm{Å/s}$, respectively. Lower deposition rates can only be calculated afterwards from the total increase of layer thickness in a certain timeframe.

A combined oil–free diaphragm and turbomolecular pumping system evacuates the chamber to a base pressure of typically 7×10^{-7} mbar. Water–cooling of the deposition chamber wall during sample heating operation helps to achieve the lowest possible pressure. During evaporation, the pressure did not exceed 3×10^{-6} mbar.

3.1.2 In Situ Diagnostic and Sample Transfer

During the deposition process, the temperature of the sample can be monitored by means of a pyrometer. For that purpose, a sapphire viewport, which is transparent in the desired infrared region, is mounted at the deposition chamber. In order to gain information about the spatial temperature distribution, the ordinary pyrometer can be replaced by a pyrometric camera, which has been hired from DIAS Infrared for the present work. The camera detects radiation which is emitted and reflected by the sample within a sharp wavelength region around $\lambda = 5\,\mu\text{m}$. The device is calibrated for the radiation of a black body, which means that both, the reflection and the transmission of the sample are assumed to equal zero. For a constant sample temperature (steady–state), this implies that the heating power, which is absorbed by the black body, equals that, which is being emitted. In order to gain the real temperature of a specismen, which is not a black body, the signal has to be corrected by introducing the emissivity ϵ. By this means, the deviation of the optical properties from the black body can be quantified. Therefore, the emissivity of a set of representative samples has been measured in the infrared region and used for the calibration process. The results are presented in Section 5.3.1. During and after the data aquisition, the thermograms have been analyzed with the software PyroSoft Professional [32].

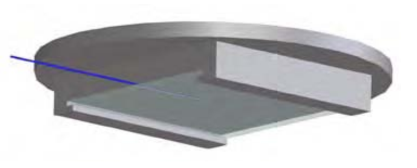

Figure 3.3: Model of the sample-holder with thermocouple

Additionally, the temperature near the sample surface has been measured using a type K thermocouple with a diameter of 0.25 mm, which can be fixed at a specially prepared sample holder directly behind the glass substrate (see Figure 3.3). Due to limitations of the chamber configuration, the mounting of the thermocouple prohibits the rotation of the sample stage and the semi–automatic handling of the sample holder. Therefore, the thermocouple has been used for calibration purposes, and was afterwards removed from the vacuum chamber.

After the deposition, the processed sample can be transferred directly in high vacuum by using two semi–automatic handler–systems. Hereby, the pressure never exceeds 1×10^{-5} mbar. A SEM mounted at the second handler chamber allows in situ

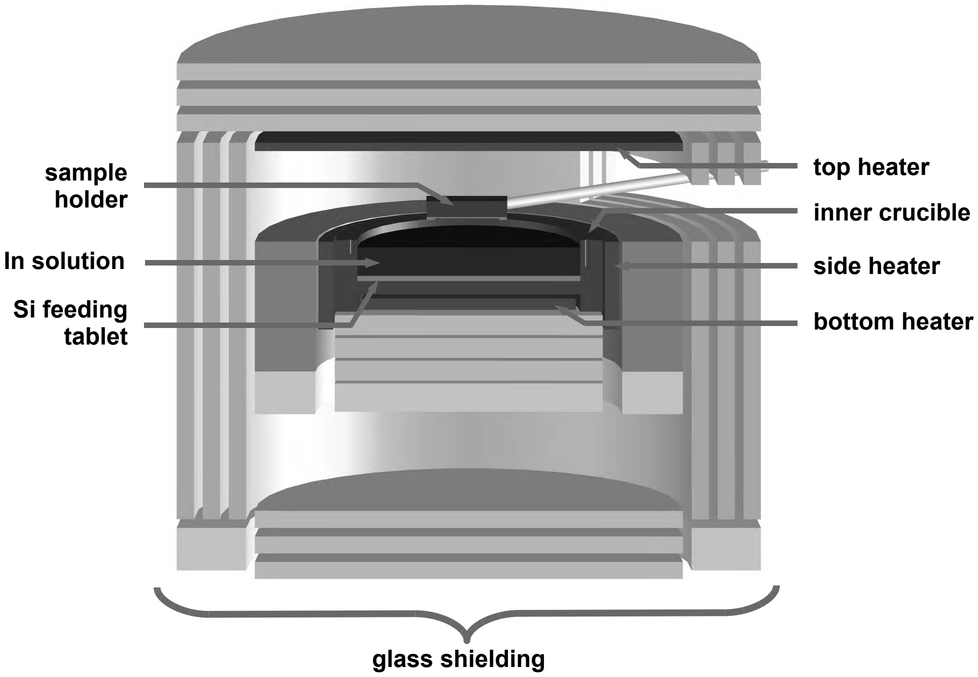

Figure 3.4: Schematic view of the inner part of the steady–state solution growth chamber.

diagnostic of the sample surface prior further processing. The resolution of electron imaging is reduced by vibrations coupled into the system by the diaphragm pumps. These vibrations can be minimized by switching off the pumps during measurements or by making use of a specially adapted stabilizer. The overall sample transfer from the vapor deposition chamber to the steady–state solution growth apparatus takes about 30 min.

3.1.3 The Steady–State Solution Growth Chamber

The steady–state growth apparatus consists of two nested water–cooled vessels. The outer part is a conventional high vacuum chamber. The inner part houses the growth crucible, three graphite heating elements and a combined glass/molybdenum shielding (see Figure 3.4). The growth crucible is made from high purity graphite (FE779), a special high density graphite for semiconductor industry. Inside the crucible a [001] oriented silicon feeding source is situated below a two centimeter high indium bath. The sample can be brought into contact with the indium in top–down position with the help of two automatic handler systems. Two type K thermocouples with H_2 resistant sheathing (TC2 and TC3) are embedded in the crucible walls to

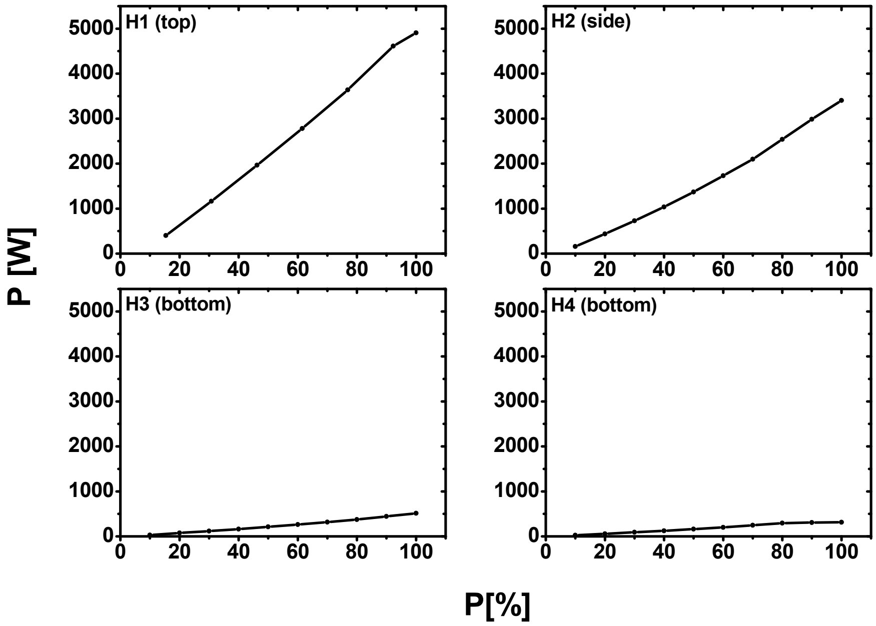

Figure 3.5: Absolute heating power as a function of output power.

measure the temperature at two different depths (1.2 cm and 2.6 cm, respectively). Heating of the crucible can be achieved by heating from top (H1), from side (H2), from bottom (H3 and H4), or by a combination of the different graphite heating elements. The calibration of controller output to absolute heating power is shown in Figure 3.5. The heater H1 is able to generate the highest heating power in order to establish a significant temperature gradient in the growth solution. Temperature is adjusted by two high precision controllers connecting TC2 to H1 and TC3 to H2 or optionally to H3/H4. An additional thermocouple (TC1) is situated in the direct vicinity of H1 in order to monitor heating power of the upper heating element.

The epitaxy chamber is continuously purged by a gas flow of 380 sccm hydrogen. Prior to that, the gas is purified using a palladium diffusion cell in order to fulfill the needs for low temperature epitaxial solution growth [33, 34]. The purity of the ambient is measured by a Hiden HPR20 quadrupole mass spectrometer to detect presence of explosive hydrogen–oxygen mixtures and residual gases. Figure 3.6 shows the characteristics of the residual gas concentration directly after venting the chamber for maintenance with subsequent sealing and heating to 600 °C (TC2 and TC3). Also shown is the state after four weeks of continuous hydrogen flow,

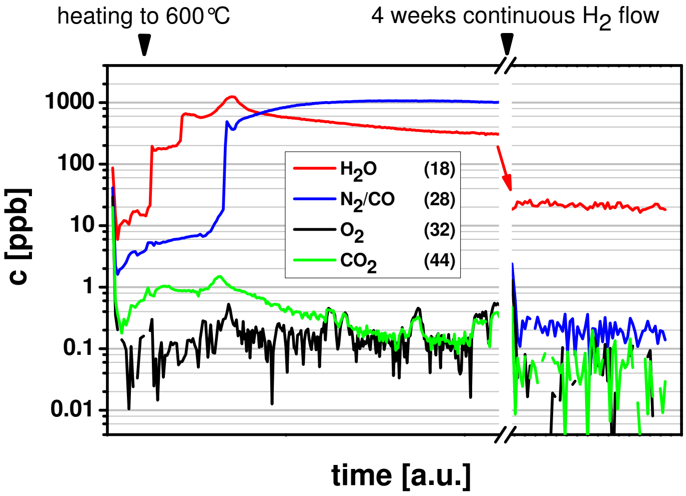

Figure 3.6: Residual gas concentration in epitaxy chamber directly after chamber maintenance and after four weeks of continuous H_2–flow.

resulting in a significant decrease of the residual gas content. Actually, after several months of operation, the water content decreases to typically 1–2 ppb and other residual gases are not detectable any more.

The heating process first leads to outgassing of water, which was introduced during contact of the system with air. As heating elements reach temperatures above 670 °C, graphite is expected to reduce residual water to form carbon monoxide and hydrogen. This can be shown by a calculation of Gibb's free energy versus temperature for this reaction using FactSage [11] and explains the retarded increase of mass number 28 signal (N_2/CO) seen in Figure 3.6. In order to reduce further contamination, hydrogen flow is only interrupted when transferring a sample into the chamber. The growth chamber can be evacuated to a pressure as low as 5×10^{-6} mbar allowing sample transfer from and to the rest of the cluster tool. To enable save evacuation, the chamber is purged by a flow of 16000 sccm argon for 14 min prior to the evacuation procedure.

3.2 Sample Processing

3.2.1 Sample Cleaning Procedure

In order to remove organic contaminations, all used glass substrates were cleaned within two steps of an empiric wet–chemical process. First, the substrates were cleaned in 100 % acetone for 20 min at room temperature under ultrasonic exposure.

After rinsed in de–ionized water ($\varrho > 15\,\mathrm{M\Omega\,cm}$), samples were held in 2 % dilute alkaline cleaner (LM2) for 20 min at 45 °C in the ultrasonic bath. Afterwards, they were again rinsed in de–ionized water and dried in nitrogen flow. Subsequently, the samples were transferred into the high vacuum cluster tool within a few minutes.

Silicon substrates were first cleaned in an acetone ultrasonic bath for 10 minutes. In order to remove foreign particles and organic impurities, samples were then soaked in NH_3(25 %)/H_2O_2(30 %)/H_2O (1:1:4) at 70-80 °C for 10 min. This process leaves a thin oxide layer on top of the wafer [35]. The oxide is removed by a 20 s treatment in HF(40 %)/H_2O (1:5). Additionally, this leads to the hydrogenation of the dangling bonds of the wafer surface. This can be checked by the immediate de–wetting of the water film after rinsing in de–ionized water. Subsequently, samples are immediately transferred into the high–vacuum chamber.

3.2.2 Vapor–Liquid–Solid Growth of Silicon Seed Crystals on Glass

Figure 1.1 shows a schematic presentation of the combined vapor–liquid–solid and steady–state solution growth method as carried out in his work. In a first step, the pre–cleaned glass substrate is coated with a thin conductive layer which might act as a backside contact in future solar cells produced by this technique. Afterwards, the sample is heated to a temperature of about 300 °C and a metallic solvent, in our case indium, is evaporated. The sample temperature clearly exceeds the melting point of indium and the metal is in the liquid state of aggregation. On low energy surfaces, the solvent nucleates to form well separated microdroplets (see Figure 1.1). Size and spatial distribution is to be controlled by deposition parameters, i.e. sample temperature and deposition rate. The second step is followed by the deposition of silicon. Due to surface diffusion and direct impingement onto the droplets, silicon is dissolved. Each droplet gets supersaturated and silicon crystals nucleate inside them. Again, success of nucleation will be shown to crucially depend on deposition parameters. A temperature gradient, which is established by means of the backside cooling between free droplet surface and the interfacial region, is intended to force the nucleation to take place in the interfacial region. This contributes to a tight adherence of the seed crystals to the sample surface. The described process leads to the formation of spatially arranged silicon seed crystals which are afterwards enlarged by means of steady–state solution growth.

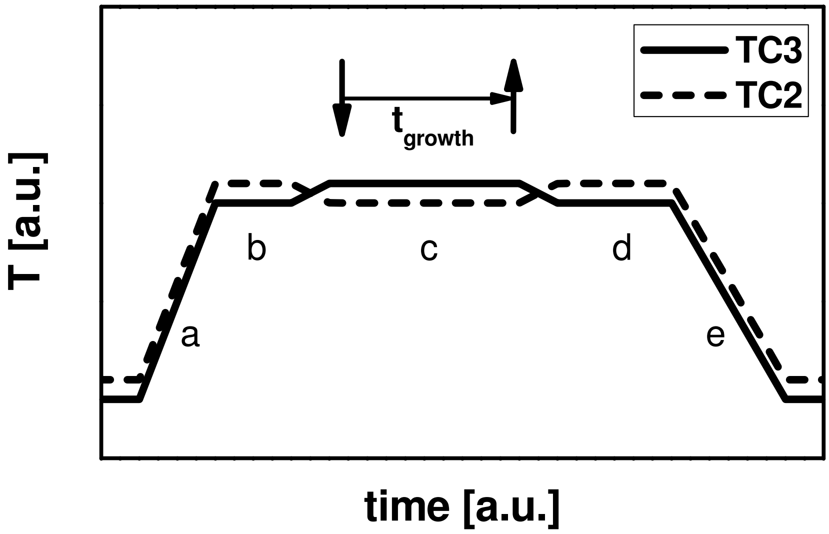

Figure 3.7: Schematic drawing of the temperature at the individual process steps of the steady–state solution growth method.

3.2.3 Outgrowth of Seed Crystals Using Steady–State Solution Growth

In order to enlarge the seed crystals, the feasibility of a modification of conventional liquid phase epitaxy entitled steady–state solution growth is investigated. Here, a vertical stack of a crystalline silicon feeding source at the bottom, indium, and the growth sample at the top is heated to the operating temperature of 600–700 ℃. In order to perform the enlargement of the seed crystals, a temperature gradient is established in a way that the substrate is placed within the coldest zone of the solution. The temperature difference between the two thermocpouples (TC2 and TC3, see Section 3.1.3) is in the order of 10 K. The temperature distribution inside the crucible must contribute to mass transfer and adjust supersaturation for growth on the upper substrate as discussed in Section 5.5. The growth process can be divided into five main stages which are illustrated in Figure 3.7: a) heating–up, b) saturation, c) growth, d) homogenization and e) cooling down. The first step was performed by applying the top heater to achieve a heating rate of 10 K/min in all experiments. During heating–up, the sample rests in the inner part of the furnace without solution contact. Once the growth temperature is reached, the system is held under this heating configuration for at least one hour to let the feeding source saturate the solvent up to the equilibrium concentration. Afterwards, the temperature gradient is reversed in order to start the growth process. The sample is now brought into contact with the solution. After a typical growth time of two to four hours, the sample is lifted off and the temperature gradient is reversed again. After a dwell–time of at least eight hours with heating from top (homogenization), the crucible is cooled down at a rate of 1 K/min while maintaining the temperature gradient.

4 Characterization Methods

Besides the growth techniques which are explained in detail in Chapter 3 supporting analysis and characterization were carried out by means of several techniques described in the present chapter. Most samples were analyzed by using scanning electron microscopy and energy dispersive X–ray analysis (EDX). Atomic force microscopy was used to characterize selected surfaces regarding morphology and roughness. Crystallinity, layer thickness and orientation was analyzed by using X–ray diffraction and reflectometry. As EDX is only applicable to detect major constituents, impurity concentrations were measured by means of secondary ion mass spectroscopy.

4.1 Scanning Electron Microscopy

Scanning electron microscopy (SEM) combined with energy dispersive X–ray analysis was used on a regular basis to characterize surface morphology and spatial element distribution of the processed samples. In contrast to optical microscopy one can benefit from a high spatial resolution and a large depth of sharpness. In this work a FEI Nova 600 NanoLab dual beam system was used to analyze the processed samples. SEM pictures were analyzed by means of an image processing and object analysis software [36].

The SEM signal is generated by the interaction of a focussed accelerated electron beam with an energy of 2–10 keV with the surface of the specimen. The penetration depth is typically in the order of several tens of nanometers. Therefore, SEM images are a two-dimensional projection of the first few tens of nanometers of the sample. The interaction of the electrons with the sample includes the elastic and inelastic back–scattering of electrons (BSE), the emission of low energetic secondary electrons (SE) and the generation of Auger electrons and characteristic X–rays. Secondary and backscattered electrons are collected in electron microscopy to scan the morphology of the surface. In the available setup, secondary electrons ($E<50\,\mathrm{eV}$) can either be collected by means of a Everhart–Thornley (ETD) or an in–lens detector (TLD). While the primary electron beam column is mounted vertically, the ETD collects the electrons under a certain angle. By this means, a surface which is directed towards the SE detector appears bright whereas other surfaces appear less bright. Additionally, edges appear bright in the SE micrographs because of the enhanced electron emission at these sites. The in–lens detector which is mounted directly inside the optical column allows the highest possible resolution and has been used for images with a magnification factor above 2000. The BSE detector was used only infrequently. Its application allows for an enhanced elemental contrast (Z–contrast) or an emphasized topographical image. The sample stage enables vertical movement of the sample as well as horizontal adjustment, rotation and specimen tilt. A detailed description of all major components used in this work is given in [37].

Besides the morphological analysis, the dual beam system allows the collection and analysis of characteristic X–rays emitted by the sample. The characteristic X–rays are induced by the inelastic interaction of the primary electrons which generate an electron hole in an inner shell of a specimen atom. The atom relaxes by either emitting an Auger electron or an X–ray photon. The energy of the X–rays is characteristic for the emitting type of atom and therefore an energy dispersive analysis allows the detection of major components in the material. By scanning the incident electron beam, an SE image and the spatial distribution of the elements can be recorded simultaneously, thus, giving a powerful tool for composition analysis. Relative amounts of the concentrations of constituents can be derived by means of a computer–aided semi–quantitative analysis. In contrast to the SE image, the spatial resolution is limited to about 1 µm and the detection is limited to major components. Trace elements can be detected by means of secondary ion mass spectrometry (SIMS).

4.2 Atomic Force Microscopy

Atomic force microscopy (AFM) allows investigation of the surface topography of a sample. The technique can be seen as a special case of scanning probe microscopy. While light–optical as well as electron microscopy involves optical imaging of the sample structure, scanning probe microscopy images are generated by probing the interaction of a thin tip with the surface. In the case of atomic force microscopy, this interaction is mainly given by two antagonistic contributions, namely the Born repulsion and the attractive Van der Waals forces. The resulting force–distance–

curve exhibits a single minimum. The tip is now moved along the surface and the deflection of the tip which results from the topology is precisely detected by means of a laser assembly. The deflection is compensated by the movement of a piezoelectric actuator and this operation is known as constant force or contact mode. The compensation movement is utilized to gain two main signals, the topography signal t which resembles the absolute position of the actuator and the error signal e given by the adjustment needed to maintain constant force. The functions $t = t(x_i, y_j)$ and $e = e(x_i, y_j)$ represent the topography and the first derivative of the topography of the probed surface area. All micrographs presented have been measured using a Topometrics AFM device operating in contact mode.
The raw data obtained in this way has been analyzed by means of the freely available Software package Gwyddion [38]. Basic data processing included the level correction by subtracting a background determined by a polynomial up to the fifth grade in the x and y direction, respectively. Artificial scars and strokes parallel to the scanning axis have been corrected by the respective built–in algorithms if necessary. By these operations, the initial set of raw data is transferred into the respective corrected values: $t(x_i, y_j) \mapsto t'(x_i, y_j)$. The surface roughness has been determined by means of the statistics module of the software and is stated as the root mean square (rms) quantity which is defined as follows:

$$\mathrm{rms} = \sqrt{\frac{1}{mn}\sum_{i,j}^{m,n} t'(x_i, y_j)^2} \tag{4.1}$$

Here the sum is taken over all data points in the analyzed surface area.

4.3 X–ray Diffractometry

The application of X–ray powder diffraction enables the determination of the presence or the absence of particular known phases in a polycrystalline material. Despite the term 'powder diffraction', the method is also applicable to polycrystalline material deposited on a substrate as in our case. The incident X–ray beam is elastically scattered at the periodic array of atoms each forming a particular plane denoted by the respective reciprocal lattice indices hkl. The necessary condition for a reflection to occur is well known as Bragg's formula:

$$2d_{hkl} \sin\theta = n\lambda \tag{4.2}$$

Here, d_{hkl} denotes the spacing between two adjacent hkl lattice planes, θ is the diffraction angle, n is a natural number and λ is the wavelength of the incident X–ray beam. For a crystal lattice having a basis which consists of multiple atoms, the intensity I_{hkl} of the diffracted radiation is, in the case of nonpolarized incident radiation, given by [39]

$$I_{hkl} = \left[\frac{I_0 \lambda^3 R_e^2 l}{16\pi R} \frac{V_s}{V} \right] M_{hkl} F_{hkl}^2 \left(\frac{1 + \cos^2(2\theta)}{\sin(2\theta) \sin\theta} \right) \tag{4.3}$$

Here, R_e is the classical electron radius and M_{hkl} is the multiplicity of the hkl–peak. l, R and V_s denote the width of the receiving slit, the distance between the slit and the sample and the effective volume illuminated by the incident beam, respectively. V is the volume of a unit cell and

$$F_{hkl} = \sum_j \exp(i\mathbf{K} \cdot \mathbf{R_j}) f_j \exp(-2W) \tag{4.4}$$

is the unit cell structure factor. The sum is taken over all j atoms in the unit cell with their respective position R_j, $\mathbf{K}$ is the diffraction vector, f_j the atomic scattering factor and $2W$ is the Debye–Waller factor and accounts for thermal fluctuation of the position of the atoms in the unit cell. In summary, the position of allowed reflections is given by the unit cell while the relative intensity is a function of the arrangement of atoms in the unit cell, the experimental setup and the temperature. Physical broadening of the diffraction peak is mainly a consequence of the particle size being lower than 1 µm. The full width at half maximum (FWHM, measured in rad) of the reflection peak is correlated with the lateral characteristic length L of the particles via the Debye–Scherrer equation (see for instance [40]):

$$\text{FWHM} = \frac{K\lambda}{L\cos\Theta} \tag{4.5}$$

Here λ is the wavelength of the incident light, Θ denotes the Bragg angle and K is a form factor which can be approximated by 0.9. In order to predict both, the position and the relative intensities of the diffraction peaks, the freely available software package PowderCell [41] has been used. Besides

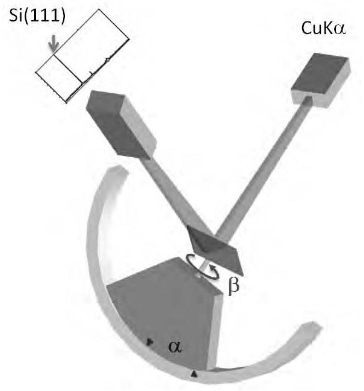

Figure 4.1: X–ray diffraction setup used in texture analysis.

the afore mentioned parameters, the unit cell and the positions of the atoms in the unit cell must be known. For the expected phases in the system under consideration here, the crystal structure parameters as used in input data are compiled with their respective reference in the appendix. In addition, the software allows the direct comparison of calculated spectra with experimental data, and enables prediction of phases appearing in the spectra.

Additionally, preferred orientations can be deduced by means of a texture analysis. Here both, the angle of the incident beam and the detector are held constant to fulfill the Bragg condition for a certain hkl reflection. The samples are mounted with a fixed initial angle of $\alpha' = 0$. The initial sample rotation β' can be varied from sample to sample in a random way. The sample is now stepwise rotated and tilt over the orientation sphere giving the polar angle $\beta = \beta' + \Delta\beta$ and the tilt angle $\alpha = \Delta\alpha$, respectively (see Figure 4.1). From these angles, a pole figure can be deduced which resembles the orientation distribution of a single lattice plane. The tilt angle α of the sample goniometer is limited by the layout of the goniometer to 70°.

All spectra were recorded using a commercially available spectrometer (GE Inspection Technologies, XRD 3003 TT) which operates in Bragg–Brentano geometry [42].

4.4 X–ray Reflectometry

X–ray reflectometry was used to determine the sequence of multiple thin layers, their respective thickness and interface roughness. The method involves the measurement of monochromatic X–rays reflected at the sample surface under grazing incidence. To be able to analyze the angular dependent reflectivity, basic principles of optics in the X–ray regime have to be considered.

Fresnel showed that the reflectivity of a material in contact with air ($n_0 \approx 1$) is related to the incident angle ω and the corresponding refractive index (n_1) (see [43]). The complex refractive index $\tilde{n}_1$ of the sample material is given by

$$\tilde{n}_1 = 1 - \delta + i\beta \tag{4.6}$$

Here, δ represents the refraction and β describes the absorption. Within the framework of the oscillator model, refraction can be shown to be related to the electron density of the material using the following equation:

$$\delta = \frac{r_0 \lambda^2}{2\pi} \rho \tag{4.7}$$

where r_0 is the classical electron radius and ρ is the electron density of the material. This equation only holds for frequencies far above optical resonances, which is fulfilled for X–rays. The electron density is a function of the mass density of the material, and therefore, the refraction depends on the mass density as well. Following Snell's law, the angle of total reflection ω_c can be determined by

$$1 - \delta = \cos \omega_c \approx 1 - \frac{\omega_c}{2} \tag{4.8}$$

For angles of incidence greater than ω_c, interference between radiation reflected at the air–layer and the layer–substrate interface occurs. The angular separation of the emerging interference fringes can be approximated by

$$\Delta\omega \approx \frac{\lambda}{2t} \tag{4.9}$$

with t referring to the distance between both interfaces, and therefore, to the thickness of the layer. The intensity of the reflection is a function of the interface roughness and the absorption in the layer. For multiple layers, complicated intensity variations may arise which are interpretable by means of reflectivity curve simulation and fitting software.

The layer structures in this work were investigated by using a high resolution spectrometer (GE Inspection technology) which operates with characteristic Cu Kα radiation. The raw data, which were provided by the characterization group of the IKZ, were analyzed by means of a specific software [44].

4.5 Raman Spectroscopy

Raman spectroscopy was used supplementary to X–ray diffractometry to detect crystalline phases in the grown material. The method involves the inelastic scattering of monochromatic light including a vibrational mode of the sample material. The scattering process can be explained within the framework of quantum–mechanic perturbation theory as the absorption and subsequent emission of a photon (energy $E_{ph,0}$) by a sample electron via an intermediate virtual energy level. Hereby, the electron is lifted from an initial vibrational state (energy E_0) to an excited state (energy E_1) and afterwards relaxes by the emission of a photon. A small portion of the excited electrons interacts with a vibrational mode of the sample material and therefore loses or gains energy. Therefore, some of the emitted photons exhibit a decreased (Stokes) or an increased (anti–Stokes) energy with respect to the incident light. This characteristic energy depends on the allowed vibrational modes and therefore on the crystal structure of the sample material. Let $E_{ph,1}$ be the energy of the elastically scattered photon, then the energy gain or loss ΔE_{ph} can be represented by the associated wavelength λ as follows:

$$\Delta E_{ph} = E_{ph,1} - E_{ph,0} = hc\frac{1}{\lambda} = hc\tilde{\nu} \tag{4.10}$$

Often, the wavelength shift is represented by its reciprocal value $\tilde{\nu}$ (wavenumber). Raman spectra were recorded at room temperature using a commercially available spectrometer (LabRAM HR 800) at the IKZ. The laser operated at 633 nm and no additional polarization filters were applied in all cases.

4.6 Secondary Ion Mass Spectrometry

Dynamic secondary ion mass spectrometry (SIMS) was used to determine the concentration of trace elements inside the growth material. SIMS includes the bombardment of the sample surface with ions and the subsequent mass spectrometry of the sputtered secondary ions. With continuous data acquisition while eroding the surface, measurement of a concentration depth profile is possible.

The primary ion beam (Cs or O_2 ions in the present case) with an energy of 1–30 keV hits the sample and produces secondary particles like photons, electrons, atoms and ions. The secondary ion efficiency is affected by the ionization potential for positive ions and electron affinity for negative ions. The use of Cs primary ions enhances the ion yield for negative secondary ions while the use of O_2 ions enhances the efficiency for positive ions [45]. Therefore, in our case, the concentration of carbon and oxygen was measured using a Cs primary ion beam while the other elements were measured using O_2 primary ions. The quantitative analysis of the elemental concentration in the sample requires the comparison with gauging standards of known concentration profile. Here, ion implants are widely used as they enable the highest possible accuracy. The secondary ion intensity I_e of an element and its concentration c_e is related to the respective quantities of the matrix element m (Si in the present case) by

$$\frac{I_m}{c_m} = \mathrm{RSF}_e \frac{I_e}{c_e} \tag{4.11}$$

Here, RSF_e is the relative sensitivity factor for the element e. If the concentration of the element e is low compared to the matrix element concentration, which is the case in trace elemental analysis, c_m can be considered to be a constant. This constant is usually absorbed in the RSF and the following expression holds, where RSF denotes the sensitivity factor for the element e embedded in the matrix element m:

$$c_e = \mathrm{RSF} \frac{I_e}{I_m} \tag{4.12}$$

This equation is used for the determination of the RSF value using a gauging standard with a known impurity concentration. The resulting value is assigned afterwards for the respective measurement of a sample with an unknown concentration. The sputter depth is measured using a profilometer. Both information yield a depth profile of the absolute concentration of the impurity in the sputtered volume. The detection threshold of the apparatus is determined by the sensitivity factor, by residual gases in the equipment and by dark count rates arising due to cosmic rays. The measurements were carried out using a Cameca ims 4f and a Cameca ims 4f-E6 secondary mass spectrometer in collaboration with RTG Mikroanalyse GmbH.

5 Results and Discussion

This chapter describes the theoretical and experimental results which are discussed based on the considerations made in Chapter 2. Considerations regarding the thermochemistry of the materials involved in the process (indium, silicon and molybdenum) were carried out in order to ensure thermodynamic stability of the backside electrode layer. Molybdenum silicides are shown to resist solution contact during the last process step. Indium droplet formation and seed crystal growth was studied in detail on pure molybdenum and molybdenum–silicon multilayers. In order to commission the steady–state growth apparatus, fluid flow and saturation conditions in the growth crucible under several heating regimes were checked. Growth results are discussed considering additional finite–element simulations of the temperature and flow velocity field. Enlarged silicon crystallites were characterized in order to gain closer insight into morphology, growth mechanisms and purity.

5.1 Thermochemistry in the Ternary System Mo–Si–In

In solution growth, knowledge of the temperature dependent phase equilibria is essential to be able to predict thermodynamic stable phases and saturation conditions. First successful experiments on droplet formation and silicon seed crystal growth were carried out using pure molybdenum as back–electrode layer and indium as solvent [46]. Based on this system, binary phase equilibria for all tree pairs of material were considered. The ternary system is discussed in order to identify thermodynamic stable phases.

In the discussion, except for nucleation theory, the validity of bulk thermodynamics is assumed even for liquid microdomains as found during the vapor–liquid–solid processing. The deviation for small–sized particles is given by the significant influence of the surface energy which adds to the Gibb's free energy and therefore tends to destabilize the respective phase. This leads to an enhancement of the equilibrium vapor pressure above the enclosed phase and a reduction of the associated melting and evaporation temperatures. The additional Gibb's free energy of a spherical cluster related to the curvature of the surface (radius r) is given by [47]

$$G^{surf} = \frac{\gamma_{l,v} V_l}{r} \tag{5.1}$$

where $\gamma_{l,v}$ is the specific surface energy and V_l is the molar volume of the regarded phase. In the case of indium at 300 °C ($\gamma_{l,v} = 554\,m\mathrm{N/m}$, $V_l = 15.7\,\mathrm{cm^3/\,mol}$, $r = 2 - 5\,\mu\mathrm{m}$ [48]) the additional Gibb's free energy is of the order of 1 J/ mol. This is small compared to the absolute value of the bulk Gibb's free energy G^{bulk} which is in the order of 10^4–10^5 J/ mol in the desired temperature range as can be derived using FactSage [11]. Therefore, the use of bulk thermodynamics is justified.

5.1.1 The Monotropic System a–Si/c–Si

Solid silicon is known to appear in a thermodynamic stable crystalline and a metastable amorphous form. Both polymorphs form a monotropic system, that is below the melting temperature of the crystalline phase, the Gibb's free energy of the amorphous form is always greater than that of the crystalline form. This results in a difference of the respective chemical potentials and provides an inherent driving force for the monotropic transition from the amorphous to the crystalline phase. Often, this monotropic transition is referred to as *recrystallization*. Nevertheless, if kinetic effects like reordering, nucleation and crystallization are omitted, both forms can be formally treated as being thermodynamically equivalent phases of one material. Therefore, phase relationships will be described by equilibrium thermodynamics even if the term *equilibrium* only holds for crystalline silicon. The author is aware of the apparent fact that the amorphous phase will transform into the crystalline phase whenever a proper kinetic pathway is given.

In consequence of the afore mentioned convention, a discrete melting temperature can be assigned to the amorphous as well as to the crystalline phase. This behavior has been subject of several experimental studies including the melting of a–Si without recrystallization applying pulsed laser irradiation [49, 50]. Figure 5.1 clarifies this situation by showing the temperature dependence of the enthalpy H and the Gibb's free energy G of amorphous, crystalline and liquid silicon in the same diagram. As the Gibb's free energy of the amorphous phase exceeds the value of the crystalline phase, the intersection G(a–Si) and G(l) at $T_{m,\text{a-Si}}$ is shifted towards a lower temperature with respect to $T_{m,\text{c-Si}}$ where G(c–Si) and G(l) intersect (point 1). Therefore, the amorphous phase is in metastable equilibrium with a supercooled liquid at the point labeled 2. In order to calculate the enthalpy associated with the

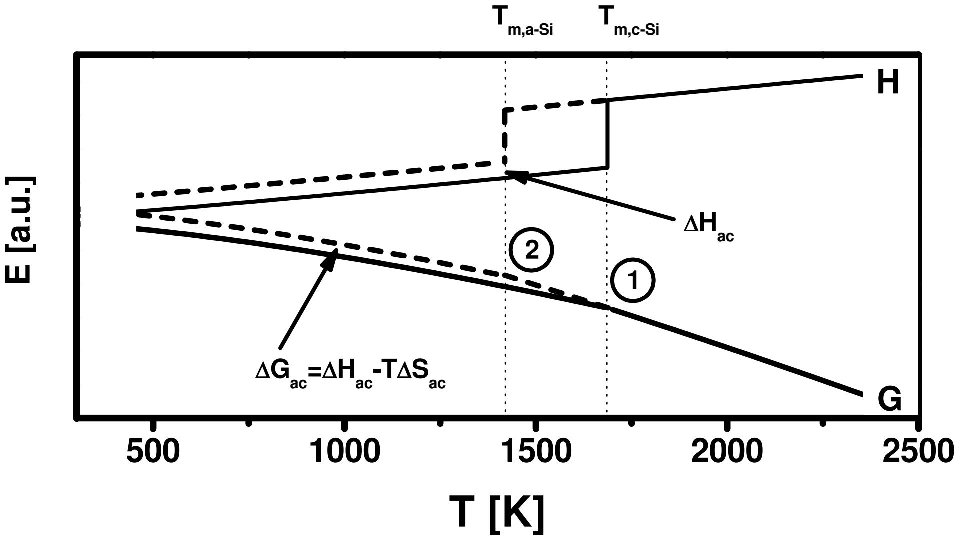

Figure 5.1: Enthalpy H and Gibb's free energy G for amorphous and crystalline silicon.

solidification of the amorphous phase, the heat of fusion of the crystalline phase has to be reduced by the heat of the monotropic transition ΔH_{ac}. The molar heat of recrystallization Δh_{ac} has been determined by Donovan et al. to equal 13.4 kJ/mol [51]. Using the molar heat of fusion $\Delta^{l,s}_{\text{c-Si}}h = 50.6\,\text{kJ/mol}$ of crystalline silicon, the respective value for a–Si can be estimated to equal 37.2 kJ/mol (see Table 5.1).

5.1.2 Conventional Solution Growth in the In–Si System

The temperature dependent solubility of silicon in indium will be discussed based on thermodynamic principles and a suitable solution model. In 1960, Thurmond and Kowalchik considered the solubility of silicon and germanium in 14 different elements (amongst others: indium) [10]. They interpreted experimental data by

		c–Si [52]	a–Si [51]
$\Delta^{l,s}h$	[kJ/mol]	50.6	37.2
T_{melt}	[K]	1685.0	1460.0
a	[kJ/mol]	39.2	
b	[kJ/mol K]	0.0071	

Table 5.1: Heat of fusion, melting temperature and binary interaction parameters for c–Si and a–Si.

T [°C]	x_{c-Si}	x_{a-Si}	$\Delta^{a,c}\mu$ [kJ/ mol]
600	3.69×10^{-4}	13.6×10^{-4}	9.4
700	13.3×10^{-4}	41.1×10^{-4}	8.9

Table 5.2: Equilibrium concentration of c–Si and a–Si in In and driving force of recrystallization at 600 °C and 700 °C.

introducing a parameter they called α in the following way:

$$\alpha = \frac{RT \ln \gamma_A}{(1 - x_A)^2} \tag{5.2}$$

They found that this parameter is a linear function of the temperature for the examined elements. A comparison with eq (2.9) results in a proper interpretation of this factor being related to the series expansion coefficients of the excess Gibb's free energy of mixing. Therefore, the phase equilibrium of solid silicon and silicon dissolved in indium can be evaluated by applying the model of a quasi–regular solution [53]. Within this model, the parameters a and b in eq (2.10) only refer to interactions inside the solution. Assuming the structure of the solution being equal for both, the dissolution of a–Si and c–Si in indium, a and b can be seen as being valid for both cases. Experimental data derived by Alonso et al. [52] and the latest data published by Donovan et al. [51] which were applied for the equilibrium calculation using eq (2.10) can be found in Table 5.1. Figure 5.2 shows the indium–rich part of the resulting binary phase diagram. The liquidus concentrations of c–Si and a–Si in indium at two process–relevant temperatures are compiled in Table 5.2. Additionally, the driving force $\Delta^{a,c}\mu$ for recrystallization of amorphous silicon is listed for both temperatures. As indicated by the vertical dotted lines in the phase diagram (Figure 5.2), the same driving forces would be built–up by saturating indium with crystalline silicon and cool the solution by 108.4 K to 700 °C or by 102.5 °C to 600 °C, respectively.

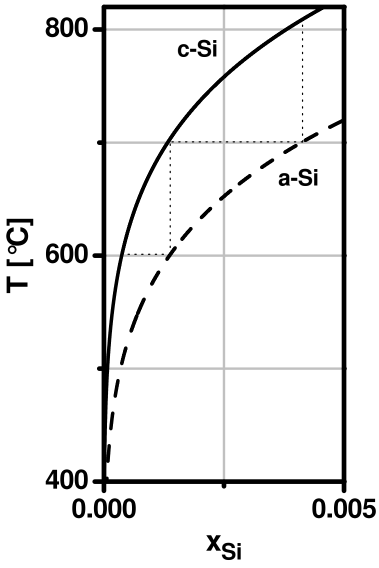

Figure 5.2: In–rich part of binary phase diagram of crystalline silicon and indium calculated from eq (2.10) together with maximum solubility of a–Si.

Furthermore, the solubility of amorphous silicon in indium is significantly higher than that of the crystalline phase. Therefore, proceeding dissolution of amorphous silicon necessarily leads to supersaturation of the solution with respect to crystalline silicon. If the supersaturation goes beyond the Ostwand–Miers region, nuclei of the thermodynamic stable phase start growing inside the solution. By increasing the mobility of silicon atoms and by decreasing the activation barrier for the crystallization process, the solvent acts as a catalyst. Another important conclusion is that it must be possible to grow crystalline silicon from a slightly supersaturated indium solution while simultaneously dissolve amorphous silicon in the same solution.

To demonstrate the advantages of steady–state solution growth, a typical conventional liquid–phase–epitaxy (LPE) experiment will be considered against the background of low temperatures. Liquid indium is saturated by bringing it into contact with crystalline silicon at the saturation temperature T_s. Afterwards it is shifted off the saturation substrate and onto the growth substrate. Let the volume of indium be $2.5 \times 2.5 \times 0.5\,\mathrm{cm}^3 = 3.125\,\mathrm{cm}^3$, the contact area with the substrate $2.5 \times 2.5\,\mathrm{cm}^2$ and the saturation temperature 610 °C and 700 °C, respectively. Under these conditions, a subsequent step cooling by 10 K results in a difference of equilibrium concentration, a driving force for crystallization and a maximum thickness of the grown layer as listed in Table 5.3 for both temperatures. At 700/690 °C, the difference of the equilibrium concentrations is about three times higher compared to the difference at 610/600 °C. Therefore, the resulting layer can be grown to a higher thickness at higher temperature. Nevertheless, the driving force for crystallization slightly decreases with increasing temperature. This can be understood by considering eq (2.13). The driving force is not determined by the difference but the ratio of the equilibrium concentrations and activities, respectively. Compared to that of the recrystallization process, the driving force due to temperature decrease by 10 K is rather low.

An absorber layer for photovoltaic application must exhibit a thickness of at least 50 µm [2]. The absolute value of thickness gained at a conventional low temperature LPE run is not sufficient for this application as shown in the last passage.

$T_s \rightarrow T_g$ [°C]	Δx_{c-Si}	$\Delta^{l,s}\mu$ [kJ/ mol]	d_{max} [µm]
610 → 600	0.56×10^{-4}	1.016	0.22
700 → 690	1.5×10^{-4}	0.923	0.58

Table 5.3: Parameters for a conventional step cooling experiment at low temperatures.

Increasing the solvent volume would help to increase the maximum layer thickness. Transport of silicon in the solution to the growing interface is solely driven by diffusion, a process which is slow compared to convection. Therefore, an increase of solvent volume would mean to significantly increase process times. One aim of the present work is to overcome this problem by taking advantage of a modification of conventional LPE. Here, the saturated liquid is supersaturated by decreasing the temperature and simultaneously transported from the saturation substrate (feeding) to the growth substrate. Afterwards, the equilibrated solvent is transported back to the feeding source. In this way, the process is conducted in a continuous way, which provides a potential for growth of thick layers at a reasonable timescale.

5.1.3 Molybdenum–Indium

In a preliminary work, molybdenum has been proposed to be a candidate for the use as conductive intermediate layer because the material allows both, indium droplet formation and seed crystal growth by applying the vapor–liquid–solid process (see [46]). Now, the applicability of this material has to be reconsidered because during the subsequent steady–state solution growth process, it is brought into direct contact with a significant amount of the solvent indium (1250 g) and the binary interaction between both has to be discussed.

Very few experimental and no theoretical data can be found in the literature regarding this system. Yatsenko and Dieva [54] presented an empiric formula for the solubility of molybdenum in indium, which they derived from fitting experimental data they obtained for temperatures below 977 °C. Figure 5.3 shows the indium–rich part of the phase diagram which can be derived from these data. For comparison, the liquidus curve assuming an ideal solution (eq (2.10) with $a = b = 0$) is drawn in the same diagram. It is clearly evident that application of an ideal solution model significantly overestimates solubility in the discussed temperature range. Therefore, the data given in ref [54] will be used in the further discussion. The equilibrium concentration of molybdenum in indium is 1.17×10^{-4} at 610 °C and 2.86×10^{-4} at 700 °C. The magnitude of solubility is comparable to that of silicon in indium. Therefore, it is expected that a 50 nm thin molybdenum layer, as used in preliminary work, is dissolved by the growth solution. To verify this estimation, several molybdenum layers, which were deposited on glass substrates, were brought into contact with the growth solution at 600 °C for 2 h. The right part of Figure 5.3 shows one of these substrates. Full removal of the film was observed in the contact area. In consequence, phase relationships between molybdenum and silicon have

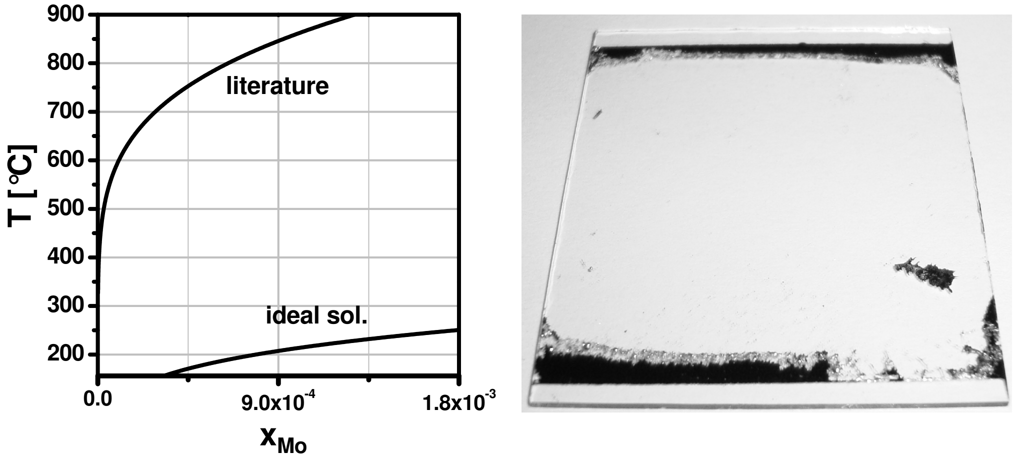

Figure 5.3: Molybdenum–rich part of the binary Mo–In phasediagram (literature data after [54]) and a 50 nm thick molybdenum layer on $4 \times 4\,\mathrm{cm}^2$ glass substrate dissolved in the growth solution at 600 °C.

to be studied as well, as both substances are expected to be present in the growth solution.

5.1.4 Molybdenum–Silicon

An equilibrium calculation in the binary system Mo–Si was performed using FactSage on the basis of the SGTE databases including SGTE_LIQU for liquid alloys and SGTE_BCC including the molybdenum A2 phase [11, 55]. The associated phase diagram is shown in Figure 5.4. Three intermediate compounds exist in the binary Mo–Si system: $MoSi_2$, Mo_5Si_3, and Mo_3Si [56]. Other authors predict an additional stability region of pure Mo_5Si_3 in the temperature range below the congruent melting point for x_{Si} being between 0.37 and 0.4 [56]. Experimental data exist only for temperatures above 1400 °C and the prosecution of this stability region to lower temperatures is likely but remains speculative. Nevertheless, all conclusions drawn in the next section concerning thermodynamic stability are not changed by the existence of this additional region.

Regarding the above–mentioned intermediate compounds, $MoSi_2$ is the most intensive studied compound because it is used as an anti-corrosive due to its high temperature stability and oxidation resistance. It is known that $MoSi_2$ can exist in two modifications, a tetragonal ($C11_b$) and a hexagonal (C40), which are referred to as t–$MoSi_2$ and h–$MoSi_2$, respectively. A transition from the tetragonal to the hexagonal structure occurs at high temperatures. The exact temperature for this

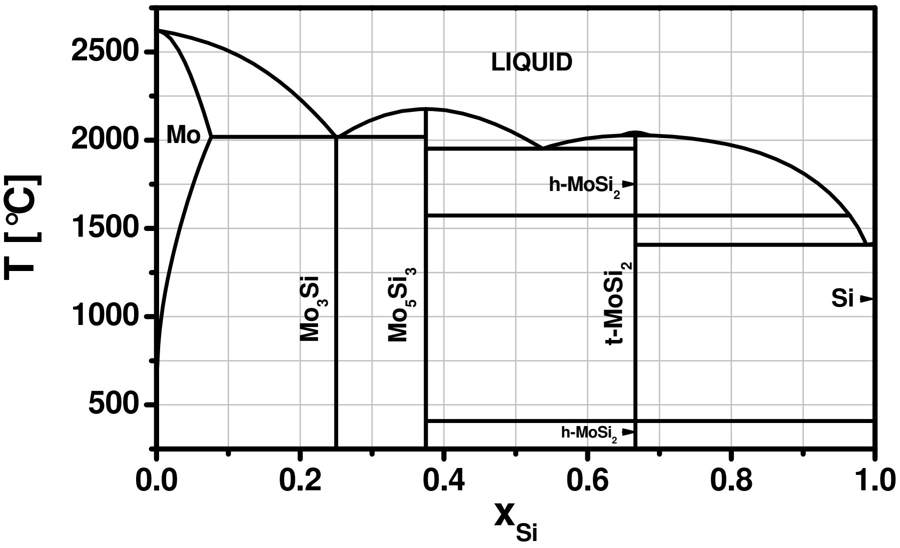

Figure 5.4: Mo-Si binary phasediagram as derived from FactSage including solid Mo_xSi_y intermediate phases.

transition is not well known, according to the SGTE database it is 1573 °C. Other authors report 1900 °C [56] or 1850 °C [57], while others doubt the occurrence of such a transformation [58]. Several authors report the hexagonal form to be stable at temperatures below 800 °C in thin films of $MoSi_2$ on silicon substrates [59, 60]. The actual transformation temperature is found to depend on the preparation method. No references regarding the solid–state silicide formation on glass substrates existed so far. Therefore, the deposition and characterization of thin $MoSi_2$–layers on glass is subject of Section 5.2.

5.1.5 The In–Si–Mo–System

The solubility of molybdenum in indium is comparable to that of silicon in indium and after having dissolved several molybdenum layers (see Figure 5.3), all three materials exist within the growth solution. To check the nature of the ternary interaction occuring in the present system, the growth solution has been examined subsequent to the dissolution of the molybdenum layers. For that purpose, the solidified indium was taken out of the graphite crucible and analyzed by means of combined SEM and EDX investigation. The study revealed the presence of solid molybdenum and silicon at the solution surface. Furthermore, molybdenum–rich regions were found to exactly coincide with silicon–rich regions. This can be seen in Figure 5.5, which resembles an EDX–mapping of the spatial distribution of Si, Mo and In of a representative area. A semi–quantitative analysis of the stoichiometry gives an atomic ratio for Mo to Si of about 0.5 and suggests $MoSi_2$ to be formed. Investigation of the bottom of the solution did not reveal any presence of molybdenum. These results can be explained by a discussion of the phase equilibrium in the present system. To the best of the knowledge, no indium containing intermediate compounds form besides molybdenum silicides in the ternary system. Thus, the binary intermediate compounds are expected to be stable in the whole indium concentration range. Using FactSage, a ternary phase diagram as shown in Figure 5.6 can be evaluated. Here, liquid indium, which contains low portions of silicon and molybdenum (denoted as LIQ), is in equilibrium with solid molybdenum–silicon compounds. Regarding our situation, where a thin molybdenum film is brought into contact with the growth solution, the associated stability region is labelled **I** in the diagram. Hence, the reaction which takes place inside the solution is

$$\mathrm{Mo} + 2\mathrm{Si} \rightarrow \mathrm{MoSi_2} \tag{5.3}$$

The associated energy release amounts to $\Delta G^{600\,^\circ\mathrm{C}} = -62.8\,\mathrm{kJ/mol}$. The emerging solid $MoSi_2$ drifts upwards because of the lower mass density compared to indium. In contrast, pure molybdenum would tend to drift downwards. The fact that no molybdenum is present at the bottom supports the idea, that the dissolved material reacts with silicon to form $MoSi_2$.

A main conclusion of the discussion above is that pure molybdenum is not compatible with the solution growth process. Therefore, one central hypothesis of this paper is that the thermodynamically unstable Mo has to be replaced by stable $MoSi_2$. The preparation and characterization of $MoSi_2$ thin films on glass as well as their stability in contact with the solution will be subject of Section 5.2.

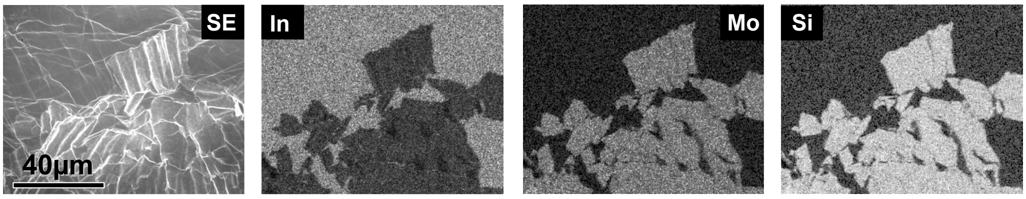

Figure 5.5: EDX–mapping of solution surface, coexistence of molybdenum and silicon.

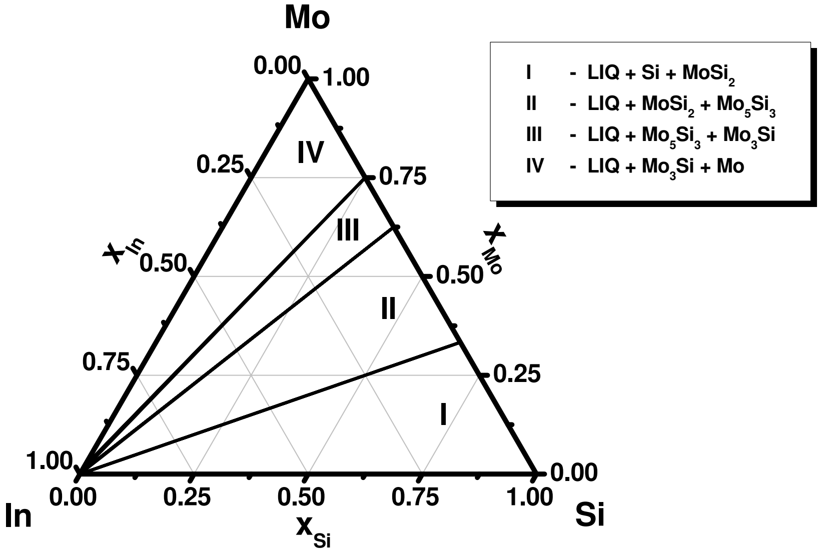

Figure 5.6: Isothermal section at 600 °C of the ternary equilibrium phase diagram of molybdenum, indium and silicon [11].

5.2 Growth and Characterization of $MoSi_2$ Layers on Glass

It has been shown in Section 5.1.5 that pure molybdenum layers, as used in preceding experiments, are thermodynamically unstable when brought into contact with silicon saturated indium solution and the application of the thermodynamic stable $MoSi_2$–compound as intermediate layer was proposed.

Thin films of $MoSi_2$ on foreign substrates can be prepared by three methods. These are: (1) co–deposition of a stoichiometric mixture or multilayer by evaporation, (2) deposition of a thin molybdenum layer on a silicon substrate, or (3) sputter–deposition from a stoichiometric target. These precursor films are transferred into crystalline $MoSi_2$ by a subsequent annealing step. The deposition of a stoichiometric multilayer requires very good control of deposition rates to achieve a suitable composition. Nevertheless, this technique has been chosen for the present study because it allows in situ processing without the need to change the existent equipment.

Up to now, only the use of silicon substrates has been subject of detailed investigation [59, 61]. This technique is used for investigation of material properties and for reference but not for our application purpose. To give an example, Chi et al. performed differential scanning calorimetry (DSC) on Mo–Si multilayers deposited on silicon substrates by heating up at different rates to study phase transformations.

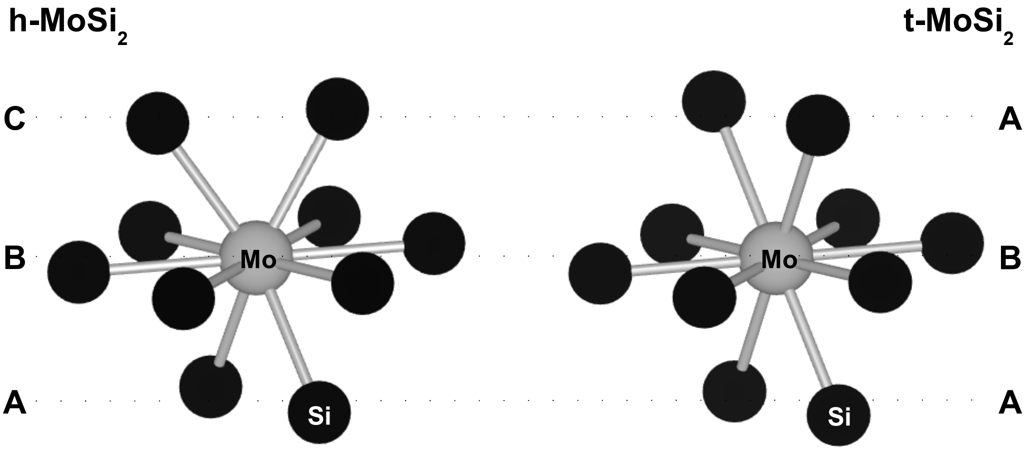

Figure 5.7: Nearest neighbour coordination of a molybdenum atom in h–MoSi$_2$ and t–MoSi$_2$.

During heating up multilayers at rather high rates ($\geq$15–20 K/min), the amorphous as–deposited structure was transformed directly into tetragonal MoSi$_2$ at about 670 °C. When heating at moderate rates the existence of a metastable hexagonal phase, only found in high-temperature bulk material or low temperature thin films, is reported to form prior to the growth of the tetragonal phase. The appearance of the metastable phase in thin solid films can be seen as a consequence of the small–size effect which leads to a change of thermodynamic equilibrium compared to bulk thermodynamics.

Crystallographic data of both phases can be found in the appendix. Hexagonal as well as tetragonal MoSi$_2$ consists of close packed planes where each molybdenum atom is surrounded by six silicon atoms. One of these planes is denoted as “B” in Figure 5.7. In addition, each molybdenum atom is bound to two silicon atoms of the overlying and underlying plane, respectively. These atoms are coplanar in tetragonal MoSi$_2$ and rotated by an angle of almost 60° in the hexagonal phase. This rotation causes a slight distortion of the nearest neighbor distances while in tetragonal MoSi$_2$ it equals 2.614 Å in all cases. Individual planes are stacked on top of each other forming a sequence of either A–B–C–A–B–C (h–MoSi$_2$) or A–B–A–B (t–MoSi$_2$). The inter-plane distance is given by 2.21 Å and 2.27 Å in the case of the hexagonal and the tetragonal phase, respectively. The layers form {003} planes in the hexagonal and {110} planes in the tetragonal phase.

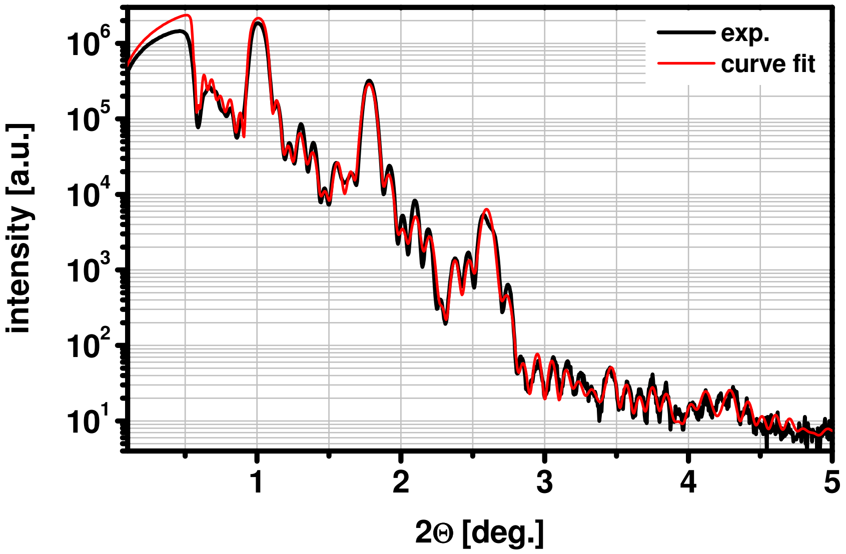

Figure 5.8: Angular dependence of reflectivity of as deposited Mo–Si multilayer.

5.2.1 Composition and Crystallinity of $MoSi_2$ Precursor Layers

The temperature dependence of the solid state reaction in Mo–Si multilayers on glass substrates prepared by electron beam evaporation has been investigated in a comparative study. Stacks of 10 Mo–Si bilayers were deposited on glass substrates by means of electron beam evaporation. In addition Si(001) was applied as reference substrate material to be able to assign Raman fingerprints to the respective crystalline phases grown on glass. In order to control and adjust the indication of the quartz crystal micro-balance, the thickness of individual layers of as–deposited films has been examined by means of X–ray reflectometry. Figure 5.8 shows the measured angular dependence of the reflectivity of a Mo–Si multilayer precursor film on glass. The data can be fitted best by assuming an individual layer thickness of 7.7 nm for silicon and 2.8 nm for molybdenum. Assuming bulk densities, this ratio can be translated to a molar composition of $MoSi_{2.14}$. The excess of silicon helps to ensure that the silicon–rich $MoSi_2$ compound is formed during annealing instead of other intermediates [61]. Further investigation of the as–deposited films has been carried out by means of powder diffraction and Raman spectroscopy. Figure 5.9 shows the associated X–ray diffraction and Raman pattern. The diffraction pattern includes a broad feature around $2\Theta = 25°$. By comparison with diffraction patterns from uncoated glass, this feature has been associated with the substrate.

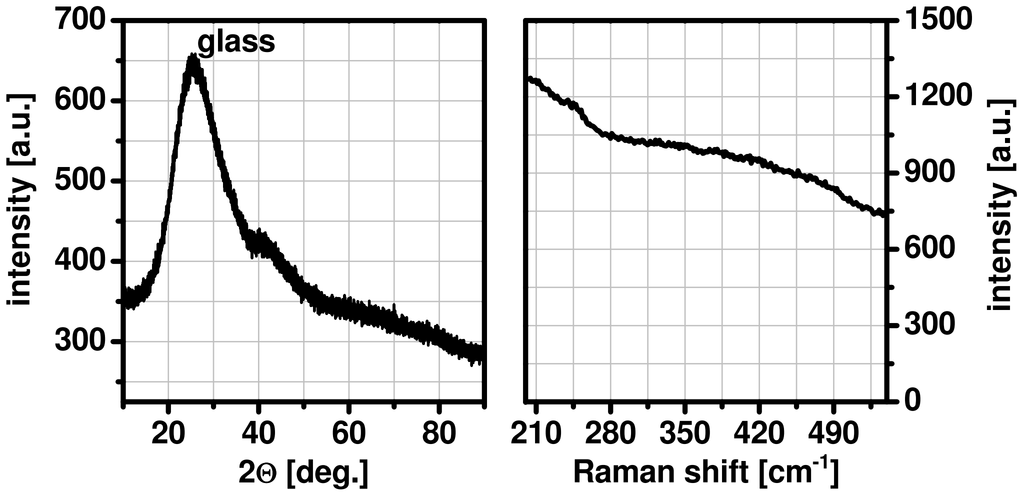

Figure 5.9: X–ray diffraction and Raman pattern of as deposited Mo–Si multilayer.

The broad shoulder around $2\Theta = 40°$ can be attributed to the deposited material but no sharp diffraction peaks were observed. This result suggests that the as–deposited multilayer is amorphous. This conclusion is supported by the Raman measurements. The right part of Figure 5.9 presents the Stokes part of the Raman spectrum where molybdenum silicides and crystalline silicon exhibit active modes [61, 62]. No sharp phonon states as they arise from crystalline material could be observed in the spectrum for the prepared samples. In addition, the surface morphology has been studied by SEM and AFM analysis. A SEM image of the surface is presented in the left part of Figure 5.10. In order to ensure proper focussing of the electron beam, a foreign particle, which accidentally adhered to the surface, was used as reference and can be seen as a bright chunk in the upper–left corner. No morphological features, which point to the formation of crystal grains, were observed as the layer itself exhibits no further contrast in the image. Also the additional AFM investigation showed no significant features at the surface. The pseudo color corresponds to a relative height of zero (blue) and 21.3 nm (orange). The rms roughness in the shown picture has been determined to be equal to 0.7 nm.

5.2.2 Preparation of Polycrystalline MoSi$_2$ Films on Glass

In order to study the crystallization behavior of the Mo–Si multilayers on glass, samples were annealed at 620 °C in high vacuum atmosphere. During annealing the pressure inside the furnace did not exceed 3×10^{-5} mbar. A heating rate of 2 K/min

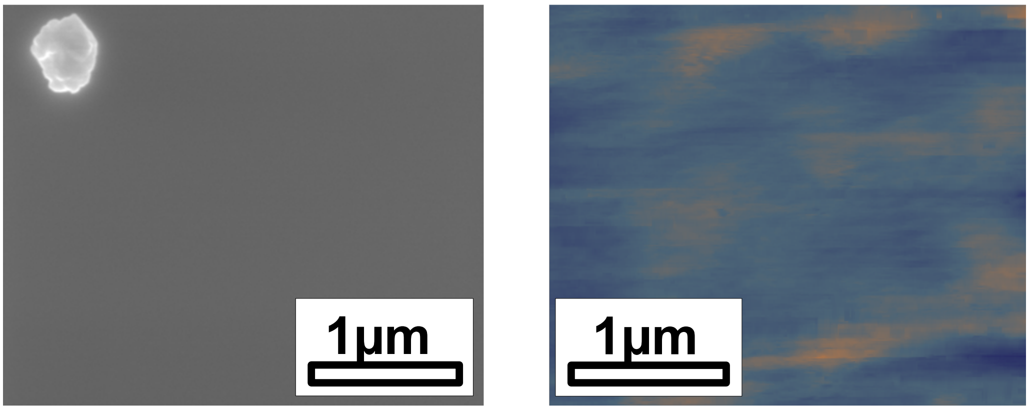

Figure 5.10: SEM and AFM topography signal micrograph of as deposited Mo–Si multilayer.

was chosen for each sample with a subsequent annealing time of 10 h. These parameters equal those of Chi et al. for the crystallization of hexagonal $MoSi_2$ on silicon substrates.

The samples were analyzed by means of SEM, AFM, XRD and Raman spectroscopy. The SEM image in Figure 5.12 indicates the formation of sub–micron sized grains in the film due to annealing. A closer examination of the image showed that the diameter of individual grains does not exceed a value of about 30 nm whereas their separation is within the same order. The right part of Figure 5.12 shows the AFM topography signal, which was recorded on the same sample as shown in the left part. The pseudo color spectrum corresponds to a range from zero (blue) to 28.1 nm (orange). Slightly elevated plates with diameters in the order of 400–500 nm were found to cover the surface. The rms value in this sample area has been determined to equal 2.3 nm. The apparent deviations of the grain structure obtained by both methods can be attributed to the differences in information depth. While AFM only accounts for the surface of the sample, SEM images contain information up to a depth of the half of the penetration depth of the electron beam. This is typically on the order of some tenth of nanometer and is therefore comparable with the overall thickness of the layer.

Additional XRD measurements revealed the presence of exactly one diffraction peak located at $2\Theta = 43.3°$. Using PowderCell [41] the position of the strongest peak to expect from a diffraction at h-$MoSi_2$ was determined. By this means, the measured peak can be assigned to the $11\bar{2}1$ reflection of h-$MoSi_2$ which is associated with a

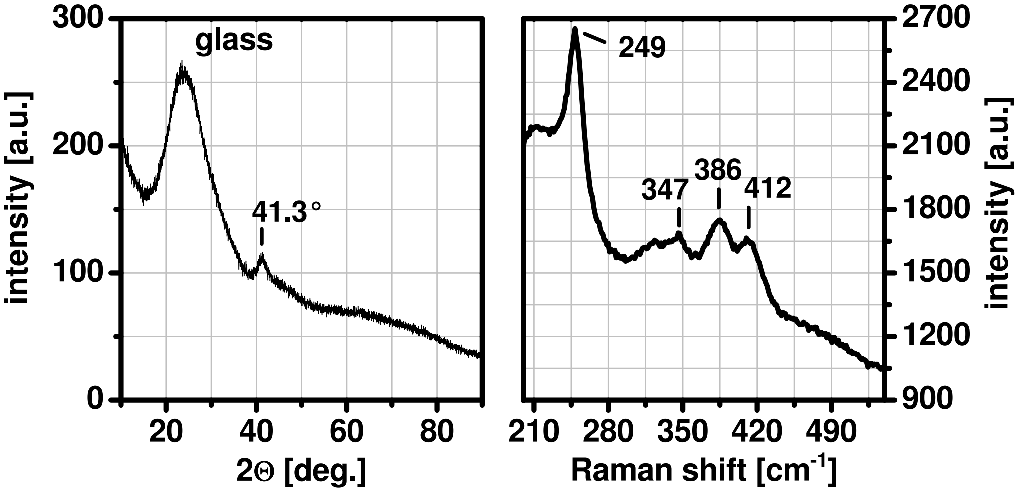

Figure 5.11: X–ray diffraction and Raman pattern of Mo–Si multilayer annealed at 620 °C.

lattice spacing of $d = 0.21828\,\text{nm}$. The strong enhancement of the intensity of a single diffraction peak is usually explained by the presence of a preferred orientation. Another possible explanation is given by the small thickness of the layer, which may cause additional peaks to vanish in the noise. The nature and origin of this finding has not been resolved definitively yet.

By applying the Debye–Scherrer equation (4.5) a typical lateral grain size of 5.7 nm can be estimated from the broadening of the $11\bar{2}1$ peak of h–MoSi$_2$ (FWHM=1.5°). This value is significantly smaller than that estimated from the SEM picture. The deviation might arise due to the limited spatial resolution of the electron microscope. Another explanation is that the peak broadening is not only due to the small particle size but also due to the limited resolution of the instrument and the line width of the Cu Kα radiation. For a better estimation, the peak should be deconvoluted into its components. Nevertheless, this procedure is hopeless for such a low intense and noisy peak.

In order to unambigeuously clarify the nature of the observed crystalline phase, the assignment of more than one diffraction peak is necessary. As only one peak has been observed, a second method was applied to resolve this problem. Here, Raman spectroscopy has proven to be able to detect and distinguish crystalline phases even when X–ray methods failed due to a low layer thickness in former investigation [63]. The associated Stokes part of the Raman spectrum for a sample annealed at 620 °C is drawn in the right part of Figure 5.11. Obvious features were observed

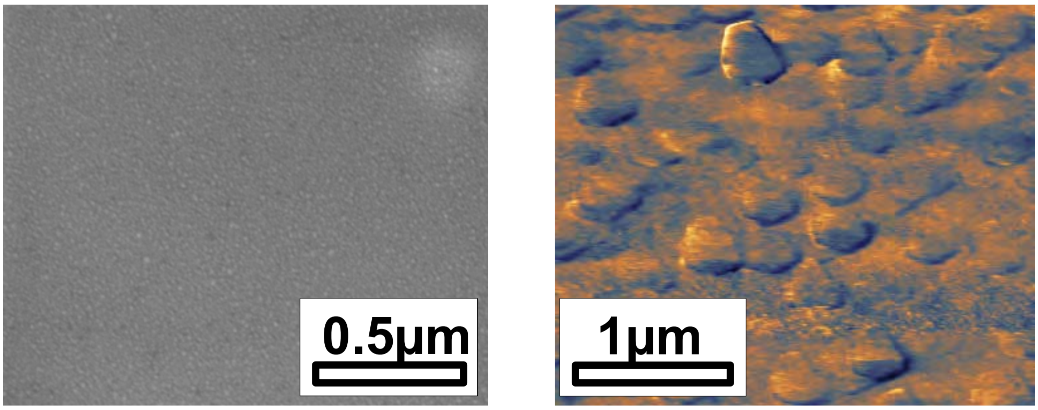

Figure 5.12: SEM and AFM topography signal micrograph of of Mo–Si multilayer annealed at 620 °C.

at wavenumbers of 249, 347, 386 and 412 cm^{-1}, weaker features form at 210 and between 280 and 350 cm^{-1}. Comparing this spectrum with that measured for the amorphous as–deposited layers gives clear evidence for a crystallization of the film due to annealing. The shape of the Raman spectrum nearly perfectly resembles that which was measured by Doland and Nemanich for h–$\mathrm{MoSi_2}$ crystallized at similar temperatures on silicon substrates [61]. Furthermore, the authors reported their main peaks to be found at 210, 260, 395 and 420 cm^{-1} as well as some minor peaks between 260 and 395 cm^{-1}. Similar results were found by Reinig et al. at the interface between molybdenum and silicon at temperatures as low as 450 °C with their peaks slightly shifted [63]. Almost all phonon states of h–$\mathrm{MoSi_2}$ found for the material produced in this work are also slightly shifted towards lower wavevectors in the spectrum, which may be assigned to tensile stress in the film. This may arise due to unsuitable thermal expansion coefficients of the film and the substrate causing the film to become strained when cooling down after annealing. As no data on thermal expansion of the metastable hexagonal $\mathrm{MoSi_2}$ phase has been found in the literature, the effect could not be quantified. Additionally to the afore mentioned tensile stress, a small grain size can lead to a shift of phonon states towards lower wavevectors.

These results strongly suggest that by annealing near–stoichiometric Mo–Si multilayers on glass a solid–state reaction takes place that is very similar to that found in layers deposited on silicon substrates. In agreement with former results, the emerging solid phase has been identified with metastable hexagonal $\mathrm{MoSi_2}$.

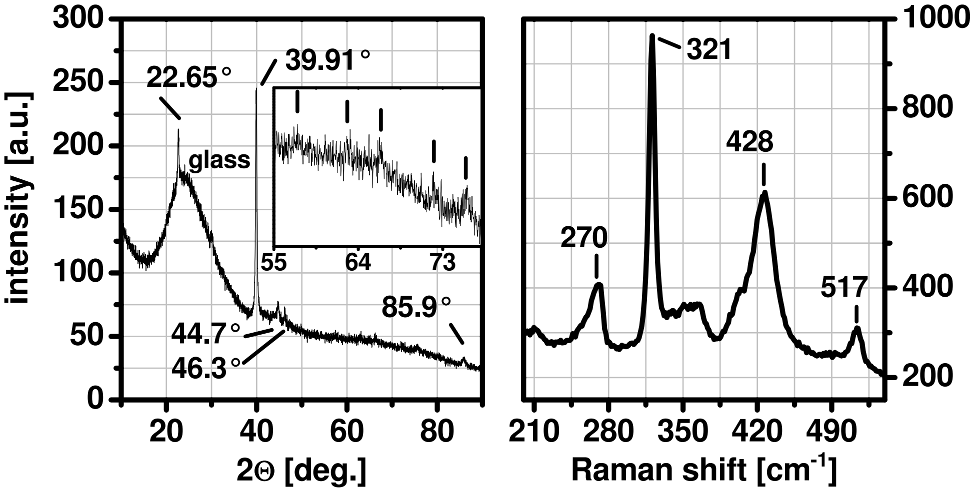

Figure 5.13: X–ray diffraction and Raman pattern of Mo–Si multilayer annealed at 800 °C.

In addition to annealing at 620 °C, further investigation has been carried out on samples annealed at 800 °C. Besides the annealing temperature, all other parameters remained comparable to those applied for samples annealed at 620 °C. As the annealing temperature lies above the softening point of the used borosilicate glass, a part of the experiments has been conducted using fused quartz as substrate material, which showed no observable distortion due to the annealing step. In contrast, annealed borosilicate glasses exhibited smooth ripples due to the softening.

The SEM micrograph presented in Figure 5.14 shows the structure of the sample after annealing. In contrast to the result obtained for annealing at 620 °C, here relatively large grains are clearly visible. Their diameter can be estimated to range from about 100 to 200 nm. The associated AFM image is shown in the same figure. The pseudo color range equals 0–19.8 nm (blue to orange). Platelets of crystalline material can be clearly seen in the picture with their shape not significantly differing from each other. In addition, the structures have a preferred orientation at least in the investigated sample area. The rms roughness has been determined as 2.0 nm and is comparable to the roughness observed on samples annealed at 620 °C.

The X–ray diffractogram of the same sample is given in Figure 5.13. Peaks at $2\Theta = 22.65°, 39.91°, 44.74°, 46.26°$, and $85.95°$ as well as some minor features at $2\Theta = 30.32°, 57.5°, 63.0°, 66.3°, 72.1°$, and $75.6°$ give clear evidence for the formation of tetragonal $MoSi_2$ in the film. The most intense reflection at 39.91° can be attributed to the $\{110\}$ lattice planes with their distance being 2.27 Å. Using

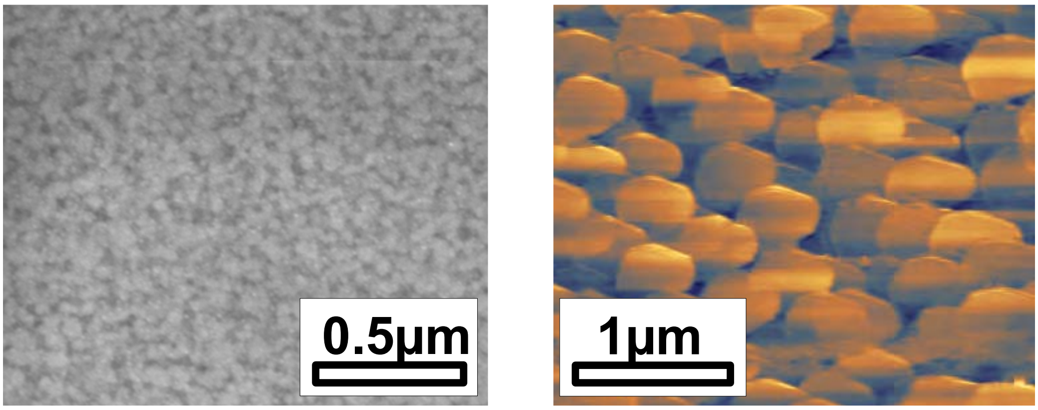

Figure 5.14: SEM and AFM topography signal micrograph of of Mo–Si multilayer annealed at 800 °C.

PowderCell, the intensity of this reflection can be estimated by theory to be only 70.8 % of the 103 reflection at 2Θ = 44.7°. In experiment, the 110 peak exhibits the highest intensity, while the 103 peak is rather weak. This strongly suggests that the grains exhibit a preferred orientation perpendicular to the {110} lattice planes. The in–plane strong inter–atomic bonds are expected to dominate the growth kinetics during formation of t–$MoSi_2$.

In addition, the 110 reflection has been deconvoluted by fitting a Voigt profile, which itself represents a convolution of a Gaussian and a Lorentz distribution [64]. By this method, the instrumental broadening, which follows a Gaussian distribution, and the physical broadening, following a Lorentz distribution, can be extracted from the peak. The FWHM of the Lorentz portion has been determined to be equal to 0.65°. Using the Debye–Scherrer equation, the average grain size has been determined to be 13 nm. Again, this value underestimates the actual grain size measured by means of SEM.

To detect possible secondary components in the film, Raman spectra were recorded in the range where $MoSi_2$ and c–Si exhibit active phonon modes. Bulk t–$MoSi_2$ has been subject of former investigation [61]. Two Raman active modes were attributed to this phase with wavevectors at about 325 and 440 cm^{-1}. The material grown in this work shows two main features around 321 and 428 cm^{-1} which are associated with t–$MoSi_2$ acting as the main component in the film. Additional phonons were observed around 270 and 517 cm^{-1} together with some minor peaks at 210 cm^{-1} and between 335 and 370 cm^{-1}. The 517 cm^{-1} feature can be attributed to the slight

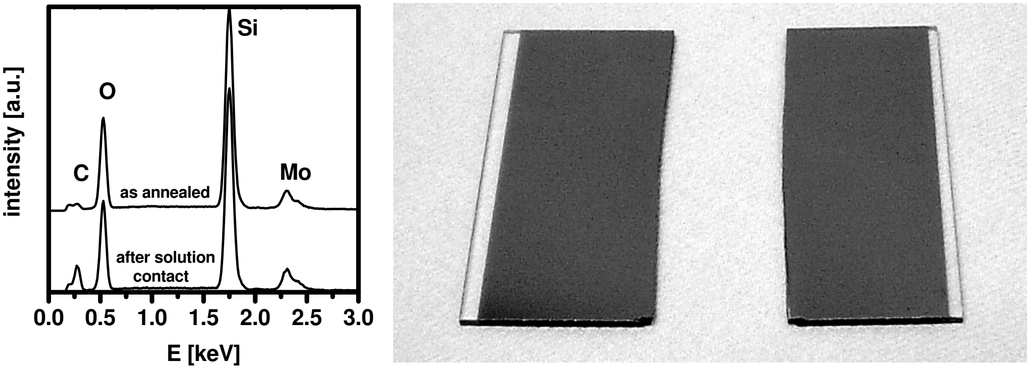

Figure 5.15: EDX spectrum and photograph of t-$MoSi_2$ layer on glass without (left) and after solution contact (right).

excess of silicon in the multilayer precursor structure, which crystallizes in competition with the silicide phase. Compared to single– and microcrystalline silicon (see Section 5.6.3), the peak is shifted towards a lower wavenumber $\nu_c = 516.8\,\mathrm{cm}^{-1}$ and slightly broadened to a full width at half maximum which equals $7.65\,\mathrm{cm}^{-1}$. This behavior indicates the grain size being in the order of 100 Å and has been reported before [65]. The nature of the other features is not clear, as additional phases do not appear in the XRD spectrum.

5.2.3 Thermodynamic Stability and Electrical Sheet Resistance of $MoSi_2$ Films on Glass

In order to verify the thermodynamic stability of $MoSi_2$ layers in contact with silicon saturated indium, the layers were brought into contact with the solution at 600 °C for 2 h, respectively. Regardless of the previously identified crystalline $MoSi_2$ phase, hexagonal or tetragonal, all layers were found to be unchanged due to the solution impact. Figure 5.15 shows a representative photograph of a t–$MoSi_2$ film on glass before and after solution contact. In a supplementary elemental analysis carried out by means of EDX measurements no significant change in composition of the layer was observed. Therefore, it has been demonstrated that the application of $MoSi_2$ instead of pure molybdenum ensures the stability of the backside layer. This result is consistent with the predictions, which were made in Section 5.1.

Formerly, molybdenum was used with the intention of providing both, a stable layer which allows the growth of well distributed indium droplets on top and a backside–electrode for photovoltaic devices. Therefore, the influence of the annealing procedure on the sheet resistance $R_\square$ of the multilayer structure was examined using the four–point probe method. In this way the influence of the contact resistance on the measurement is minimized. Relevant data derived from these measurements can be found in Table 5.4. By annealing the multilayer below the temperature of the transformation from hexagonal to the tetragonal phase, $R_\square$ was found to increase by a factor of about two. For samples annealed at 800 °C the sheet resistance significantly decreases. $R_\square$ of the hexagonal $MoSi_2$ layers was found to be about 4 times larger than that of the tetragonal $MoSi_2$ layers. This is in good agreement with data measured on silicon substrates found in the literature [66].

5.3 Indium Droplet Formation on Mo and Mo–Si Thin Films

After the thermodynamic stability of the $MoSi_2$ compound in contact with silicon saturated indium was discussed in the last section, this section deals with the next step of the process. The temperature dependence of nucleation and growth of indium droplets on glass coated with pure molybdenum, molybdenum–silicon multilayers and annealed molybdenum–silicon multilayers was studied in order to achieve control over the droplet density and size. First, the temperature characteristics at the sample position, which can be achieved using the lamp heaters mounted at the HV–chamber, was determined.

5.3.1 Temperature Calibration

In order to study the temperature dependence of droplet growth behavior, the temperature characteristics $\vartheta = \vartheta(t)$ due to different lamp heating power was measured using a type K thermocouple (see Figure 3.3). The time dependence of the temperature was fitted to Newton's law for cooling, which was expanded by an additional

Multilayer Annealing	$R_\square$ [$\Omega/\square$]
none	102
800 °C (t–$MoSi_2$)	43.6
620 °C (h–$MoSi_2$)	202

Table 5.4: Measured sheet resistance for Mo–Si multilayers annealed at different temperatures.

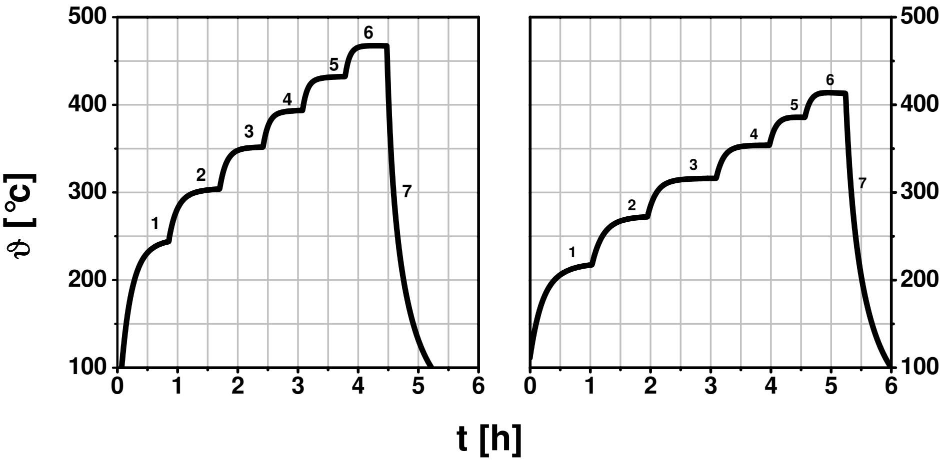

Figure 5.16: Temperature characteristics at different heating powers near the sample surface for pure glass (left) and glass/Mo–Si–multilayer (right).

heating rate J. The ansatz

$$\frac{\partial \vartheta}{\partial t} = -k\left(\vartheta - \vartheta_{room}\right) + J \quad \vartheta|_{t=0} = \vartheta_{start} \tag{5.4}$$

leads to

$$\vartheta(t) = \left(-\frac{J}{k} + \vartheta_{start} - \vartheta_{room}\right)\exp\left(-kt\right) + \underbrace{\frac{J + k\vartheta_{room}}{k}}_{\vartheta_{steady-state}} \tag{5.5}$$

Here, k is the heat transfer coefficient of the system, ϑ_{room} the room temperature and $\vartheta_{steady-state}$ denotes the end temperature which is asymptotically reached at $t \to \infty$. Figure 5.16 shows the temperature characteristics for both a pure glass substrate and a substrate coated with a Mo–Si multilayer as described in the previous section. Heating power of the lamps was increased stepwise starting from 369.6 W (step 1) up to 1523 W (step 6). Each section was fitted to eq (5.5) in order to derive the respective end temperature. The results obtained by this procedure are compiled in Table 5.5. The dependence of the steady–state temperature $\vartheta_{steady-state}$ on the nominal heating power can be well described by a third–degree polynomial. For the case of pure glass, the following equation holds:

$$\vartheta_s(P) = 83.04274 + 0.54414 \cdot P - 3.04858 \times 10^{-4}P^2 + 7.44784 \times 10^{-8}P^3 \tag{5.6}$$

If the glass substrate is coated with a Mo–Si multilayer, the temperature ϑ_s can be determined by:

$$\vartheta_s(P) = 64.4147 + 0.5155 \cdot P - 2.9206 \times 10^{-4} P^2 + 6,86054 \times 10^{-8} P^3 \tag{5.7}$$

The noticeable lower temperature behind the substrate in the case of the coated substrate is due to the shadowing effect of the layer. Further deviation might arise from the spatial separation of the thermocouple and the sample surface and the unequal optical properties of the thermocouple and the surrounding material (graphite) compared to glass.
In situ measurements using a fixed thermocouple are feasible, since the sample has to be rotated and moved in order to perform regular experiments. Therefore, the sample temperature was controlled by the output power of the lamp heaters. If not stated otherwise, all temperatures in this chapter refer to eqs (5.6) and (5.7).

In addition to the measurements with the thermocouple, results which were obtained in situ by using a pyrometric camera will be discussed in Section 5.3.5. To calculate the absolute temperature of the substrate, the emissivity has to be explicitly taken into account (see Section 3.1.2). Figure 5.17 shows measured optical data in the infrared region of four selected samples. Besides the emissivity, the reflectivity and the transmittance are plotted. The condition that the sum of all three parameters has to equal unity is satisfied by the measured data.

Coating of the glass substrate with a Mo–Si multilayer results in an enhanced reflectivity and both a slightly decreased emissivity and transmittance. The optical properties are not significantly affected by further heating the sample to indium deposition temperature (here: 270 ℃). In contrast, application of full heating power (ϑ = 413 ℃) lead to a significant change in the optical properties again. This can

	P[W]	$\vartheta_{steady-state}$ (glass) [℃]	$\vartheta_{steady-state}$ (glass/multilayer) [℃]
1	369.6	245.35	217.7
2	547.2	303.9	272.3
3	756.8	351.61	315.9
4	988	393.3	353.8
5	1236	432.19	386.2
6	1523	467.3	414.1

Table 5.5: Temperature near the sample surface versus heating power for pure glass and glass/Mo–Si–multilayer.

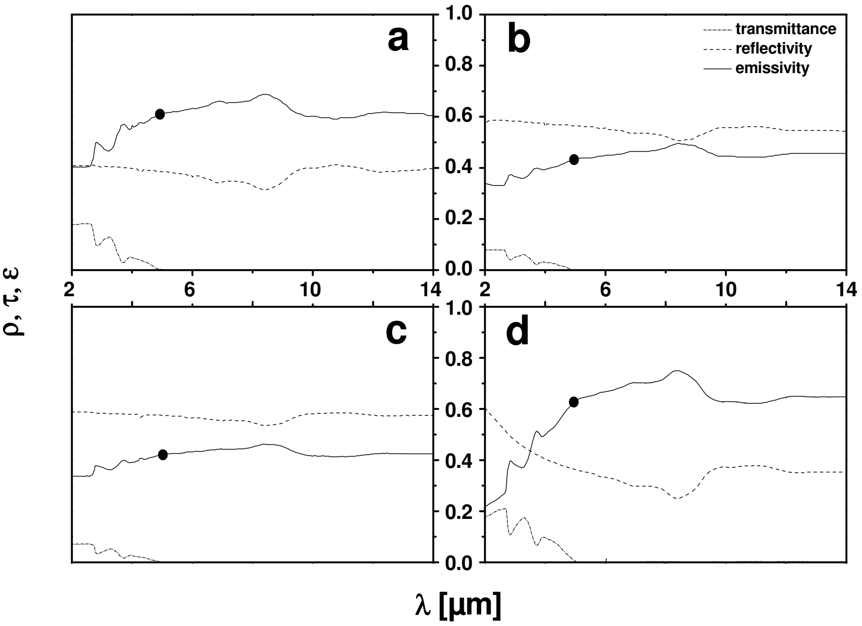

Figure 5.17: Optical properties of selected samples in the infrared region: (a) glass substrate, $\epsilon(5\,\mu\mathrm{m}) = 0.61$, (b) glass plus as deposited Mo–Si multilayer, $\epsilon(5\,\mu\mathrm{m}) = 0.43$, (c) glass plus Mo–Si multilayer annealed at 270 °C, $\epsilon(5\,\mu\mathrm{m}) = 0.42$, (d) glass plus Mo–Si multilayer annealed at 413 °C, $\epsilon(5\,\mu\mathrm{m}) = 0.63$.

be explained by the amorphous to crystalline transition in the multilayer between 270 and 413 °C (see Section 5.3.5).

All pyrometric temperature measurements were carried out at a wavelength of $\lambda = 5\,\mu\mathrm{m}$. The absolute values of the temperature given in Section 5.3.5 were determined using $\epsilon(5\,\mu\mathrm{m}) = 0.43$.

5.3.2 Thin Film Stability

The nature of the nanoscopic wetting behavior of indium on coated glass substrates is characterized using the instability criterion of eq (2.60). To determine the excess interaction, ΔG the spreading parameter S has to be derived first. The nature of the system Mo/In(liq)/vacuum is considered as apolar, because it fulfils the condition that at least two of the constituents are apolar (no acid–base interaction, see [28]). Therefore, the polar part of the spreading parameter equals zero. In this case, the apolar part of the spreading parameter $S^{LW} = S$ can be derived straight forward

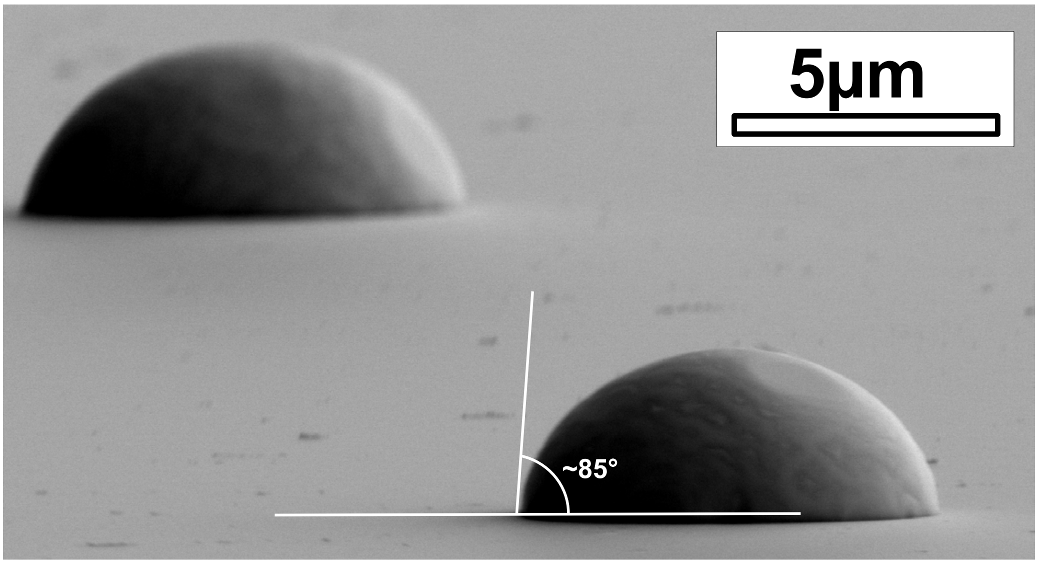

Figure 5.18: 85° tilt SEM micrograph of a solidified indium droplet on Mo coated glass showing θ being about 85°.

by using Young's equation. By combining eqs (2.48) and (2.49), the spreading parameter is shown to be a function of the specific surface energy of the liquid γ_l and the apparent macroscopic wetting angle θ:

$$S = \gamma_l \left(\cos(\theta) - 1\right) \tag{5.8}$$

Generally, the temperature dependent wetting angle can be determined by means of the sessile droplet method [67]. With the present instrumentation used for the experiments the wetting angle is only accessible by ex situ SEM–investigation at room temperature. By this means, the wetting angle was determined to be about 85°. With $\gamma_l = 0.554\,\mathrm{N/m}$, the spreading parameter S can be determined to be equal to -0.506 N/m. The layer thickness dependence of the excess Gibb's free energy per unit area using eqs (2.57) and (2.58) is plotted in Figure 5.19 together with its second derivative with respect to the film height h. The contribution of the apolar LW–forces and the Born repulsion to the total excess Gibb's free energy is referenced as dashed lines. A liquid indium film with a thickness exceeding the critical value $h_e = 1.64\,\text{Å}$ fulfils the criterion that $(\mathrm{d}^2\Delta G/\mathrm{d}h^2) < 0$. The critical height lies in between the covalent and the van der Waals radius of an indium

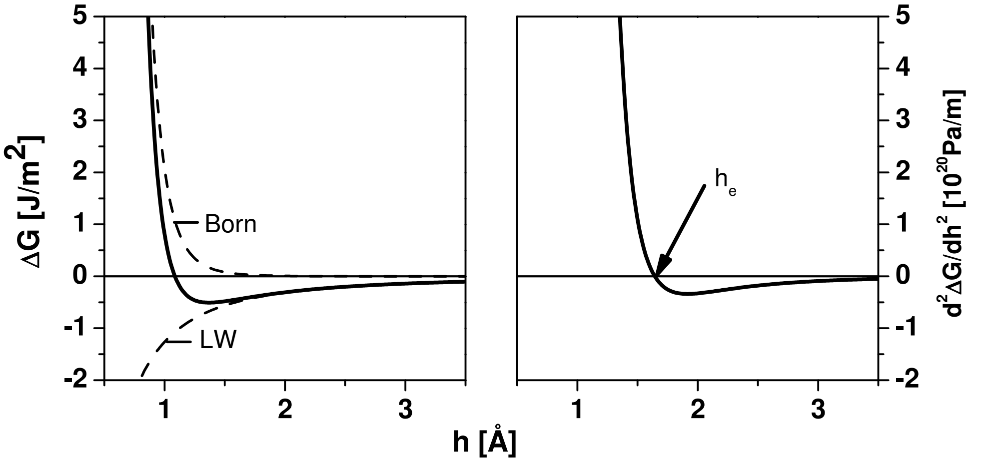

Figure 5.19: Excess Gibbs free energy with thin film height for an apolar system and second derivative (wetting angle $\theta = 85°$, $\gamma_l = 554\,\mathrm{mN/m}$).

atom (1.44 Å and 1.93 Å, respectively). The thickness of the stable film therefore corresponds to the height of one monolayer. If h exceeds this value, the film is expected to rupture under a small perturbation and droplets are forming. The subsequent dynamics of liquid indium can be described qualitatively by means of classical nucleation theory and surface diffusion phenomena. Experimental results on the formation of microdroplets on Mo coated glass substrates are shown and discussed in the following section.

5.3.3 Droplet Formation on Glass Substrates Coated with Mo

In order to compare the nucleation and growth behavior of indium on Mo–Si coated glass, first the droplet formation on glass substrates coated with pure molybdenum was investigated for reference. Results were obtained using initial 50 nm thick molybdenum layers deposited at room temperature. Subsequently, the samples were heated–up immediately by switching on the lamp heaters. After 30 min, when approaching the corresponding steady–state temperature by at least 90 %, the deposition of 20 nm indium at a constant rate of 0.1 Å/s was started. Afterwards, the samples were investigated by SEM. Micrographs were taken at the center (1), at the edge (3) and in between both points (2), respectively.

The diameter of the emerging droplets was found to vary from 7.5 µm to 10.5 µm. Figure 5.20 shows the determined droplet density at the center of the samples as a function of the sample temperature. The density shows the tendency to decrease

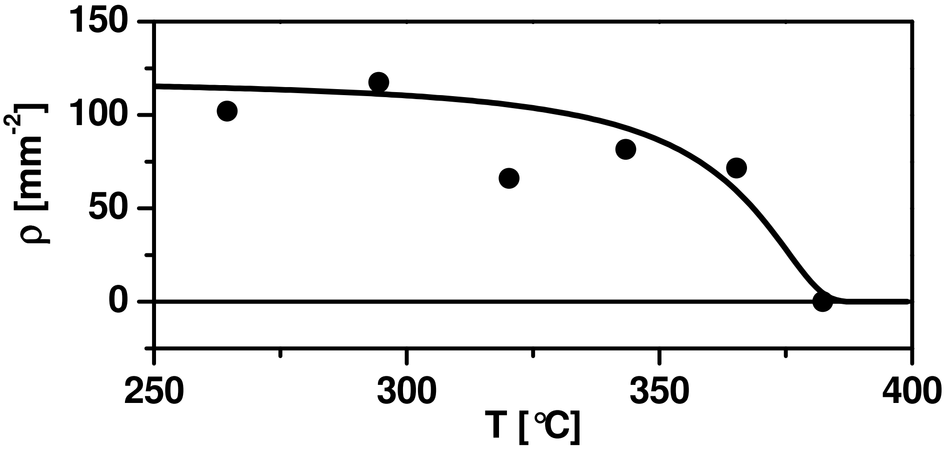

Figure 5.20: Temperature dependence of indium droplet density on molybdenum measured at the center of the sample.

with increasing temperature. If the temperature of the sample exceeds a certain critical value, the deposition was found to be completely disrupted and the droplet density equals zero. Additionally, the droplet density was found to increase with increasing distance from the center of the sample. This result indicates that the sample temperature decreases from the center to the edge. This finding was analyzed in more detail using a pyrometric camera and is discussed in Section 5.3.5.

The observation can be understood by considering the dependence of the rate of heterogeneous nucleation J on the substrate temperature. Because the indium evaporation crucible was heated applying the same heating power in all experiments, the source temperature T_s and therefore the equilibrium vapor pressure p above the source is assumed to be constant. In Figure 5.20 a plot of eq (2.52) using $C_1 = 120$, $C_2 = 1$ and $T_s = 400\,^\circ\mathrm{C}$ qualitatively resembles the temperature dependence of the droplet density. The deviations might arise due to changes of the total amount of indium in the crucible and curvature of the source due to evaporation leading to different vapor pressure above the source in different sets of experiments.

Classical nucleation theory clearly underestimates nucleation rates as it neglects small size effects like the excess intermolecular interaction described in Section 2.4.2. It has been shown before that the assumption of a spherical nucleus with a contact angle which is identical to the macroscopic value is not sufficient in presence of additional body forces [30]. Classical nucleation theory is therefore not applicable for a quantitative description of nucleus shape, contact angle and nucleation rate.

The second effect which determines the droplet distribution is transport of the liquid at the substrate. It has been demonstrated in Section 2.4.2, that a liquid film whose height exceeds the height of one monolayer is unstable. Therefore, adjacent droplets can not communicate via a thick wetting layer and indium particles have to reach the growing droplets solely by diffusion. Particles reaching an existing droplet are integrated and cause the droplet to grow. In a simple model, each growing droplet is therefore surrounded by an indium depletion area. Each droplet consists of the missing amount of material which was deposited on this area during indium deposition. Nucleation and growth of new droplets is prohibited in the depletion areas because the saturation does not exceed the critical supersaturation. Assuming the depletion areas to be circles around each droplet, the area is then

$$A_{dep} = 2\pi \left\langle r^2 \right\rangle \tag{5.9}$$

With eq (2.28) this becomes

$$A_{dep} = 2\pi L^2 = 4\pi D t \tag{5.10}$$

Considering the temperature dependence of the diffusion constant, the depletion areas are expected to grow faster at higher temperatures. Therefore, the initial droplets which formed with a low density (see Figure 5.20) at this temperature quickly form their depletion areas and inhibit further nucleation. To roughly estimate the area of the depletion circle, the temperature dependence of the diffusion constant has to be known. As no data on the diffusion of indium on thin films of molybdenum is known, data, which were measured for indium on single–crystalline Mo(110), will be used [68]. With $D_0 = 0.75 \times 10^{-11}\,\text{Å}^2/\text{s}$ and $W = 0.3\,\text{eV}$ the average displacement L of an indium atom after 10 min can be estimated to range from 48 µm at 250 °C to 82 µm at 350 °C. Therefore, after 10 minutes of deposition, the formation of new droplets is already inhibited if the distance between them is lower than about 100–160 µm in the desired temperature range.

5.3.4 Droplet Formation on Glass Substrates Coated with $MoSi_2$

In order to check the wetting behavior of indium on the formerly produced $MoSi_2$ layers (see Section 5.2), samples were coated with 20 nm indium at 295 °C. Figure 5.22 shows a SEM micrograph of the surface of a t–$MoSi_2$ layer after the indium deposition step. In sharp contrast to the wetting behavior on pure Mo, the solvent

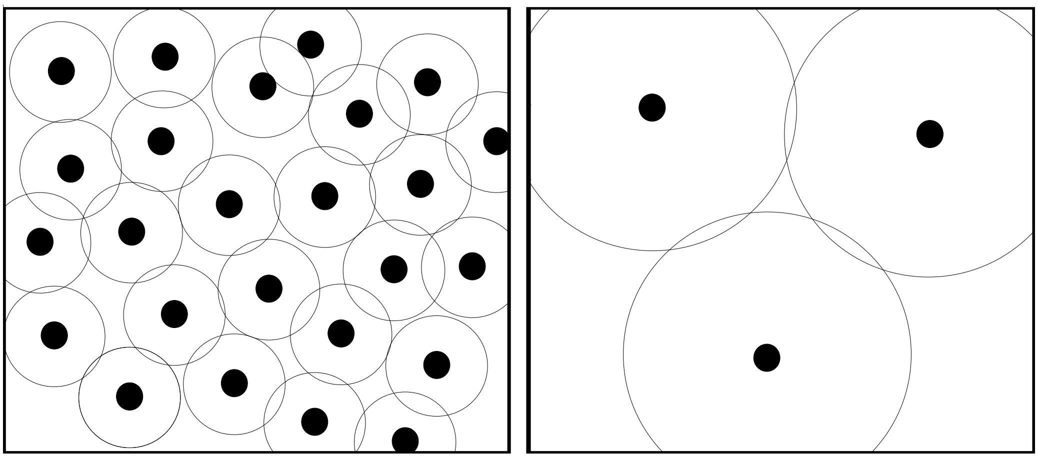

Figure 5.21: Depletion area model for growth of liquid droplets on a substrate, the temperature on the left picture is lower than that of the right picture.

was found to form sub–micron sized clusters at the surface. The density of the clusters is in the order of 150 µm^{-2}. This observation might be interpreted as a result of the surface morphology change due to the amorphous–crystalline transformation of the multilayer. The initially flat as–deposited material is transferred into sub–micron sized $MoSi_2$ grains as has been shown by the XRD investigation discussed in Section 5.2. The grains cause a considerable increase of the surface roughness and indium droplets are expected to decorate the grain boundaries.

5.3.5 Wetting of Glass Substrates Coated with Mo–Si Multilayers

In the previous section, a high density of crystal grains in the silicide layer after annealing was made responsible for the inappropriate droplet formation. In order to combine both, the thermodynamic stability of the rough crystalline $MoSi_2$ and the possibility to grow well separated microdroplets on flat layers, the wetting behavior of indium on as–deposited multilayers was investigated. Each multilayer starts with silicon and is terminated by molybdenum. To investigate the indium droplet formation, the samples were heated up to the deposition temperature without any preceding annealing step. The indium coverage was afterwards investigated by means of SEM analysis.

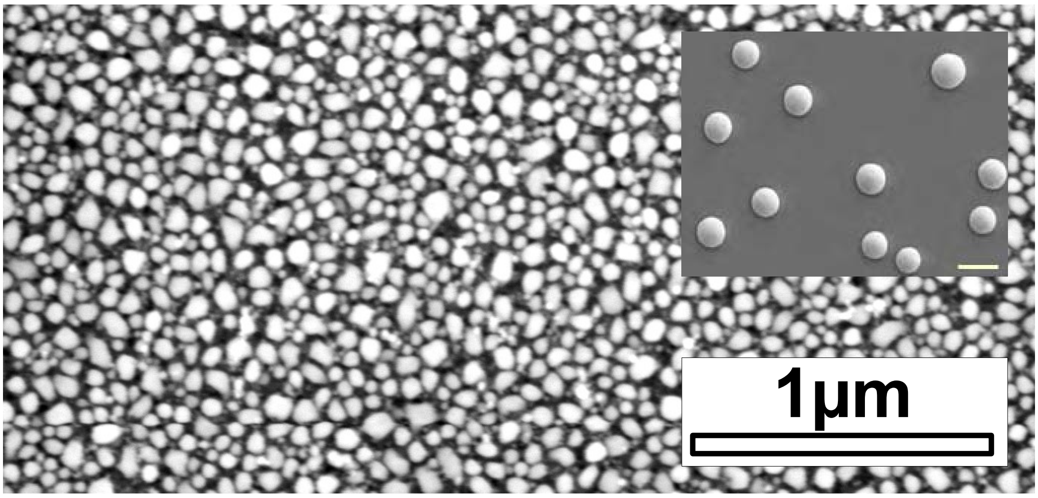

Figure 5.22: SEM micrograph of sub–micron sized indium clusters formed on t-MoSi$_2$, inset: indium microdroplets on pure Mo, scalebar: 10 µm.

Droplet Formation

First experiments revealed the successful formation of droplets, however, a high dependence on the substrate temperature was found. If a characteristic temperature T_c is exceeded, the wetting behavior was found to change dramatically. This has been shown by samples which were processed at about 320 ℃ (thermocouple). Such samples consist of two characteristic regions, see Figure 5.23. Both regions can be clearly separated in the photograph. In the inner part, indium coalesced to sub-micron sized particles. In the outer part, microdroplets with a distance in the order of several 100 microns formed.

From the experiments which were carried out on molybdenum the conclusion was drawn that the temperature is not uniform over the substrate. The inner part was found to be at a higher temperature than the outer part due to enhanced heat dissipation favoured by the graphite sample holder. This resulted in an increase of the droplet density with distance from the center. In the case of processing on multilayers, the opposite tendency was observed. To get a closer insight into this unexpected behavior, the temperature distribution on the substrate was studied by means of a pyrometric camera. Figure 5.24 displays a thermogram of the sample shown in Figure 5.23 which was taken during the indium deposition step. The absolute temperatures were derived using an emissivity of 0.43 which is valid for

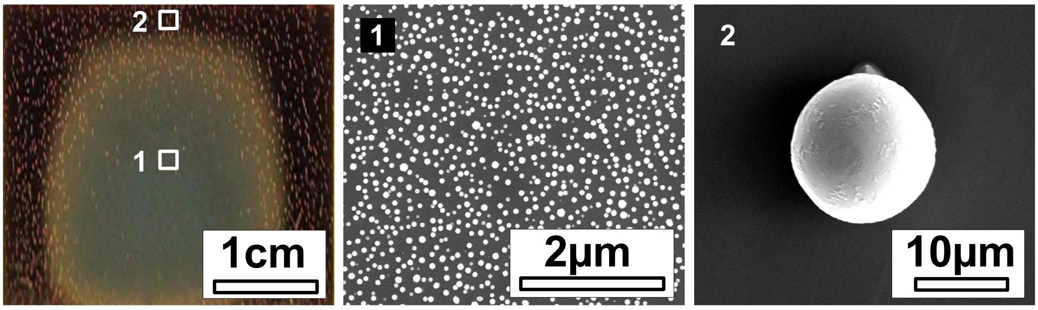

Figure 5.23: Photograph of the multilayer surface after indium deposition at 320 °C, SEM picture of region 1: sub–micron sized particles, region 2: microdroplets.

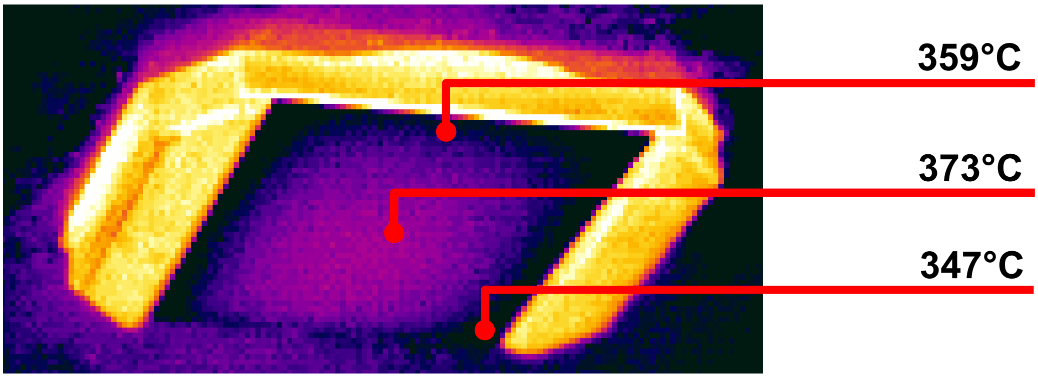

Figure 5.24: Thermogram of a Mo–Si multilayer during indium deposition ($\epsilon = 0.43$).

the substrate. Because the emissivity of graphite is close to unity, the temperature of the sample holder is clearly overestimated and appears as bright areas in the pseudo color photograph. The temperature difference between the center of the sample and the border was measured to be 14 K whereas the maximal difference amounts to 26 K. The pseudo color spectrum was chosen in a way that areas with a temperature below $T_c = 358$ °C appear as black. The coloured area on the substrate perfectly resembles the shape of the inner part of the substrate seen in the photograph of Figure 5.23. Therefore, the characteristic temperature for the transition from separated micro- to tightly packed nanodroplets can be fixed to 358 °C. This transition must be caused by a change in the chemical or morphological constitution of the subjacent layers. The onset of crystallization of the Mo–Si multilayer at the characteristic temperature would cause both, an enhanced surface roughness as well as a change of the chemistry. A higher roughness leads to a decrease of the macroscopic diffusion length, even if the length of the path stays the same on an atomic scale. This would cause an increase of the nucleation density. The chemistry influences both, the nucleation rate (via G^*) and the contact angle. Young's equation relates the equilibrium contact angle of a liquid on a flat solid surface with the specific surface energy of the substrate and the liquid and the specific interfacial energy:

$$\cos\theta = \frac{\gamma_s - \gamma_{l,s}}{\gamma_l} \tag{5.11}$$

For a certain liquid (indium, $\gamma_l = 0,554\,\mathrm{J}/m^2$ at 300 °C [48]) the wetting behavior is determined by the so called driving force for wetting which is given by the difference of the specific surface energy of the solid and the interface energy. Particularly, if the driving force is of the same order as the surface energy of the liquid, a relatively small deviation causes a drastic change in wetting behavior.

To enlighten the nature of the observed transition, indium has been removed from the surface of the sample using aqua regia. The success of indium removal was controlled by means of combined SEM/EDX investigation. This procedure leaves the glass substrate and the multilayer intact. Afterwards, the layer chemistry has been investigated by Raman spectroscopy in both regions. The surface morphology has been subject of additional AFM investigation. The original topography signal has been levelled by subtracting a fifth degree polynomial background in the x and y direction, respectively. This operation and the successive roughness and grain size determination has been conducted using the AFM image analysis software Gwyddion [38].

The Raman spectra indicate that the heat treatment during indium deposition lead to the formation of crystalline h–$MoSi_2$ (see Section 5.2.2). The presence of this phase did not depend on the position at the substrate. The surface morphology shows the characteristic flaked structure found in $MoSi_2$–layers in both regions. The gray scale range of the images corresponds to 0–37.7 nm in the upper and 0–18.6 nm in the lower image. While the size of the flakes ranges from 300 to 350 nm near the edge of the sample, at the center the size has been determined to range from 200 to 250 nm. The rms roughness has been measured to equal 1.8 nm near the edge and 2.0 nm at the center of the sample.

The nature of the transition in droplet growth behavior could not have been clarified in detail yet. As Raman spectroscopy is sensitive not only for the surface but related to the penetration depth of the incident laser radiation, it basically gives

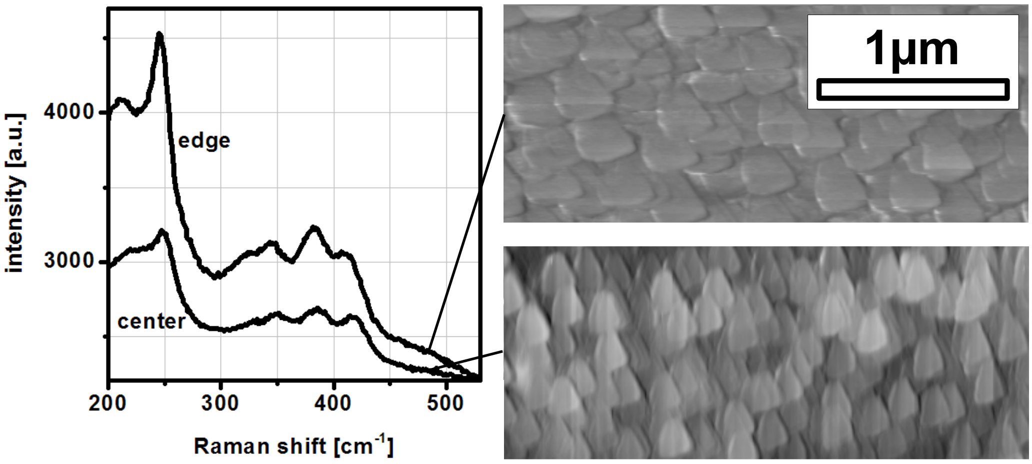

Figure 5.25: Raman spectrum and AFM images of the topography signal taken at the center and near the edge of the sample (indium removed by etching in aqua regia).

information of the "bulk" of the layer. A significant change in bulk chemistry could have been subject of the explanation of changed droplet growth behavior, but this has not been observed in the measurements. The slight increase of surface roughness and the decrease in grain size when approaching the center of the sample might be made responsible but this explanation remains speculative. Besides this unsatisfactory result, the analysis gave clear evidence for the transformation of the amorphous multilayer to h–$MoSi_2$ even at temperatures as low as 350 °C. Therefore, the layer could be thermodynamically stabilized by annealing at much lower temperatures as proposed before.

Droplet Spreading and Solid–Liquid–Solid Crystallization

Besides the growth of nano– and microdroplets, the spreading of indium onto the substrate has been observed. In Figure 5.26 a SEM image of the surface of a Mo–Si multilayer which was coated with 21 nm indium at 305 °C illustrates this behavior. This temperature is only slightly lower than that of the former experiments, where nano-and microdroplets formed. At this temperature, indium was found to strongly interact with the underlying layer structure. The same observation holds for temperatures below 305 °C. Tree-like spreading patterns were observed to encircle a central point. On top of the spreading patterns, thin crystalline layers were

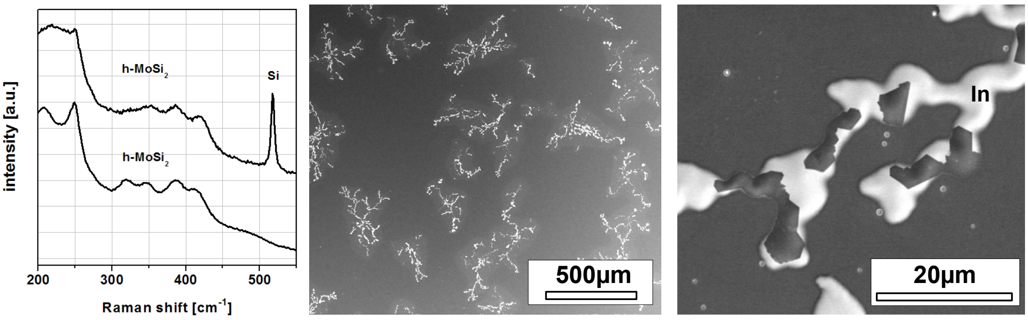

Figure 5.26: SEM images of a Mo–Si multilayer coated with 21 nm indium at 305 °C, spreading and crystallization, Raman spectra, both recorded at spreading pattern revealing crystalline phases being identified with h–MoSi$_2$ and Si.

found to exist. These findings can be understood by the thermodynamic consideration done in Section 5.1.2. Instead of forming separated droplets, the indium partially dissolves the amorphous layers up to the equilibrium concentration. In Section 5.1.2 it was shown, that the equilibrium concentration of an amorphous material dissolved in the liquid is considerably higher than that of the associated crystalline phase. Therefore, the liquid is necessarily supersaturated with respect to the crystalline phase. This supersaturation acts as a driving force for crystallization. In other words, the liquid significantly lowers the activation barrier for the phase change from the amorphous to the crystalline state by enhancing the mobility of the crystallizing species. In this way, the amorphous matrix is transformed into crystalline material even at temperatures as low as 305 °C. Raman spectra which were taken at the position of a spreading pattern revealed the presence of both phases: h–MoSi$_2$ and c–Si. The competing formation of c–Si can be attributed to the excess of silicon in the multilayer. The described solid–liquid–solid mechanism is proposed as an alternative approach for the low temperature crystallization of amorphous silicon on foreign substrates. First results on that topic are presented in Chapter 7.

Application of a Protective Interlayer

One main conclusion of the experiments described before was that the formation of stable h–MoSi$_2$ can be observed even at low temperatures ($\approx 350\,^{\circ}$C). Although the exact nature of nanodroplet formation on these films could not have been clarified in detail, the onset of the multilayer crystallization process can be made responsible for it. At lower temperatures, indium was found to show strong interaction with

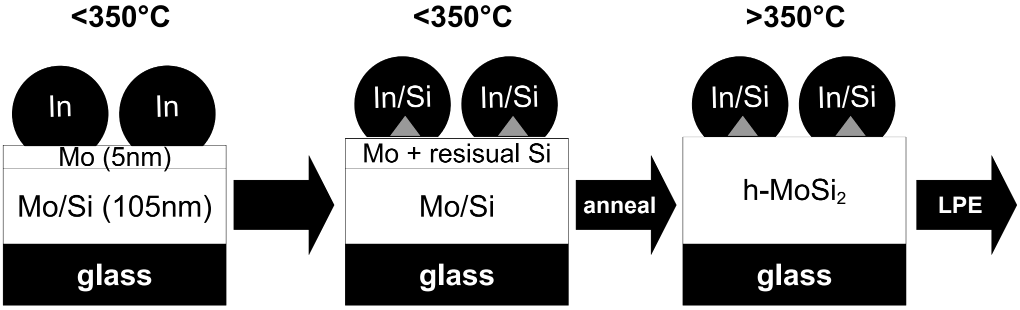

Figure 5.27: Implementation of the growth process accounting for the results in this part of the thesis.

the underlying structure leading to a monotropic phase transition in the layer. The driving force for this interaction has been identified with the difference of the chemical potentials of the amorphous and the crystalline phases, respectively. In order to allow regular microdroplet formation on these layers, they have to be buried under a thin molybdenum layer directly before the indium deposition step. A thickness of this protective coating of at least 5 nm has been proven to inhibit this interaction enabling the growth of indium droplets with their size and density being comparable to these grown on pure molybdenum. This can be explained by considering the phase diagram proposed for thin Mo films in [69]. At room temperature, as–deposited molybdenum layers are known to transform from an amorphous to the crystalline bcc structure, if their thickness exceeds about 4.5 nm. Therefore, the driving force for the spreading interaction is not present for these layers.

The sample temperature has to be held at a value below 350 °C during all steps to prevent significant crystallization of the films. The buried multilayer has to be transformed into crystalline h–$MoSi_2$ by an additional annealing step above 350 °C just after seed crystal formation (see Section 5.4). Residual amorphous silicon which remains between the droplets after seed formation is expected to combine with the subjacent protective molybdenum layer forming $MoSi_2$ during annealing as well. The described process is summarized in Figure 5.27. All results presented in the next sections have been deduced using templates which were processed in this way.

5.4 Seed Crystal Formation

Before starting to test the feasibility of steady–state solution growth, seed crystal formation was characterized first. The success of seed crystal formation was found to depend on the deposition parameters during the silicon deposition step. Particularly, the silicon vapor supersaturation plays an important role for the success of this process step. The driving force for crystallization inside the droplet is given by

$$\Delta^{v,s}\mu = \mu_v - \mu_s \tag{5.12}$$

where μ_v and μ_s are the respective chemical potential of the vapor phase and of the solid (crystalline) phase. In order to reach the growing crystal the silicon atoms undergo an intermediate liquid solution stage. If μ_l denotes the chemical potential of silicon in the solution, the following inequality must hold in order to enable a net flux from the vapor phase to the crystal:

$$\mu_v \geq \mu_l \geq \mu_s \tag{5.13}$$

By applying rather low supersaturation, silicon was found to form oxygen containing dendrite structures by a reaction with residual gas in the HV environment. Dendrites overgrow the indium droplets without any nucleation inside the droplets. The left micrograph of Figure 5.28 shows the dendrite structure obtained at a silicon deposition rate of 0.238 nm/min. SiO_x dendrites start at the bottom line of the respective droplet and branch out as they grow over the surface of the droplet. By applying a higher deposition rate (0.417 nm/min), the resulting structure contains of both, dendrites and crystalline silicon. The silicon crystal appears as a dark triangle in the SEM image. By further increase of the deposition rate, the formation of dendrites can widely be suppressed. The right micrograph shows a typical seed crystal which was grown by applying a deposition rate of 0.673 nm/min. In contrast to deposition rate, a significant influence of the deposition temperature was not observed.

Silicon seed crystals grown by this technique are found to be partly faceted. Their lateral dimension is limited by the outer curvature of the solvent droplet and is in the order of 1–6 µm. Some seeds contain several twin boundaries which lead to an enhanced growth rate during the steady–state solution growth step.

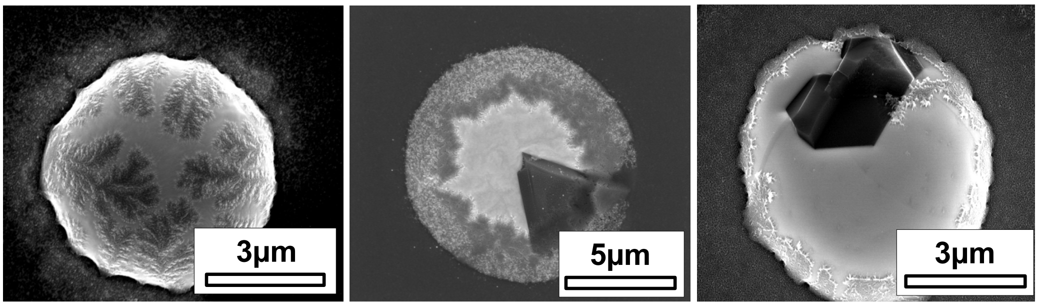

Figure 5.28: Dependence of the seed crystal formation and growth of SiO_x dendrites on silicon deposition rate (see text).

5.5 Thermo–Solutal Convection and Saturation Conditions Inside the Steady–State Solution Growth Apparatus

In order to successfully enlarge silicon seed crystals on glass, fluid flow and saturation conditions inside the growth crucible were characterized first. Growth results carried out using a molybdenum–free indium growth solution are presented. To eliminate the effects of the deposition parameters during seed crystal formation, a preliminary study was conducted on [001] oriented single–crystalline silicon substrates.

Like described in Section 3.2.3, heating of the graphite crucible can be carried out predominantly from the top, the side and from the bottom, respectively. Temperatures T_{top} and T_{bot} were measured by the two thermocouples embedded into the crucible walls at different depth.

5.5.1 Results

Solution contact was found to cause the formation of uniformly distributed etch pits at the wafer surface when heating the growth crucible from the top. The sample shown in the left SEM micrograph of Figure 5.29 was brought into contact with the solution for 2 h at $T_{top} = 700.0\,°C$ and $T_{bot} = 691.8$. Etch pits are bound by $\{111\}$ facets and indium remains preferably at the center of a cavity. These results indicate that in case of heating from top, the indium solution is permanently under–saturated at the place of the growth substrate. Due to this under–saturation, silicon from the substrate gets dissolved in indium resulting in pyramid–shaped etch pits. The electron micrograph in the middle of Figure 5.29 shows a sample,

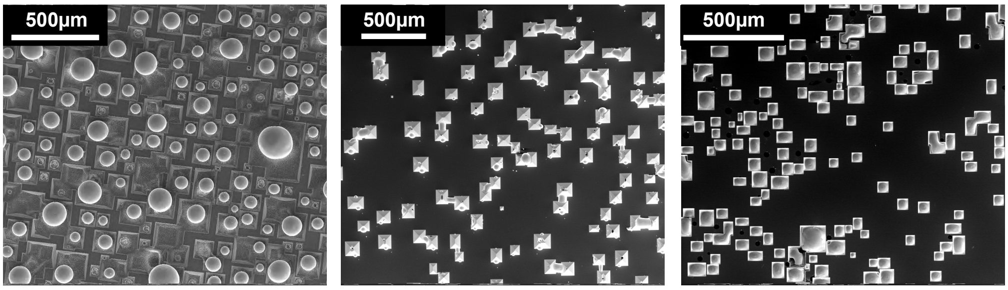

Figure 5.29: SEM micrographs of Si(001) after solution contact: (left) heating from top, (middle) heating from top with subsequent heating from the side, and (right) heating from top with subsequent heating from the bottom.

which was etched for 1 h at $T_{top} = 597.0\,^{\circ}\mathrm{C}$ and $T_{bot} = 590.0\,^{\circ}\mathrm{C}$. Subsequently, the temperature gradient has been reversed by switching to side heating. The sample remained in contact with the solution at $T_{top} = 590.8\,^{\circ}\mathrm{C}$ and $T_{bot} = 600.0\,^{\circ}\mathrm{C}$ for additional 2 h. Growth of {111} faceted silicon pyramids filling former etch pits can be clearly recognized. This result indicates the growth solution to be permanently supersaturated at the growth substrate after the temperature gradient has been reversed. The density of grown pyramids was measured to be about 17 per mm^2, each having an averaged base area of $100 \times 100\,\mu\mathrm{m}^2$. The third sample of Figure 5.29 was etched for 1 h at $T_{top} = 597.4\,^{\circ}\mathrm{C}$ and $T_{bot} = 590.1\,^{\circ}\mathrm{C}$ with a subsequent growth step using the bottom heater to set up the temperature gradient. Etch pits formed at the dissolution step were not affected during the subsequent growth step. Residual indium perfectly wets the cavities. In the first two experiments described previously, the measured temperature fluctuation around the respective setpoint at T_{top} and T_{bot} was found to be in the order of $\pm 0.1\,\mathrm{K}$. This situation can be referred to as steady–state. In sharp contrast, heating from bottom resulted in unstable temperature characteristics, which are plotted in Figure 5.30. The mean deviation from the average temperature can be found to be in the order of $\pm 1\,\mathrm{K}$. The double arrow in Figure 5.30 marks the time the sample was lifted off the solution. This procedure resulted in a partial smoothing of the temperature characteristics. The fact that no growth could be observed in the former case shows that saturation conditions are not suitable when applying the bottom heater.

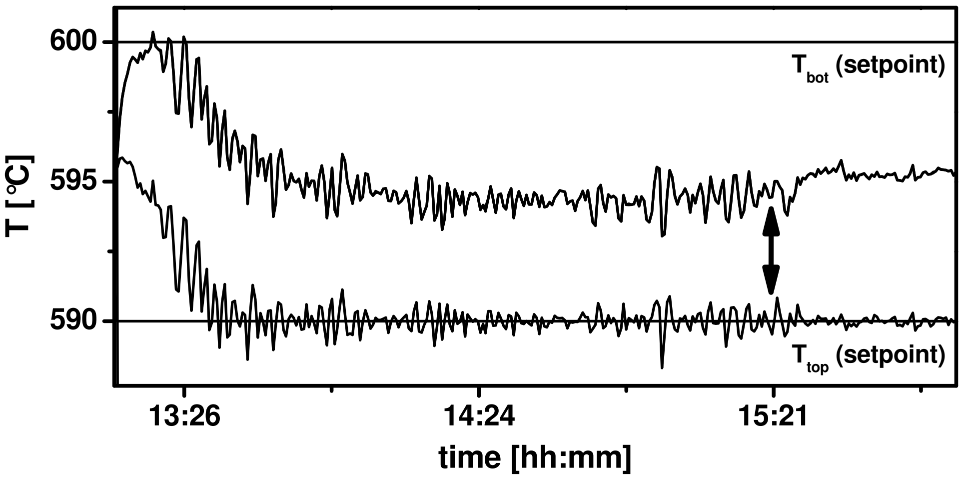

Figure 5.30: Temperature characteristics for bottom heating, arrow denotes lifting of the substrate from the solution.

5.5.2 Discussion

To explain these findings, fluid flow inside the growth crucible was examined. The configuration under consideration here is closely related to the classical Bénard–problem. In our system, indium is confined between the upper and the lower substrate and bound sideways by the crucible walls. Buoyancy forces, which arise due to density differences caused by the vertical temperature gradient, are expected to dominate the fluid flow behavior inside the growth crucible. Additionally, solutal convection has to be taken into account. Inertial forces due to a rotation of the crucible and/or the sample are not present in our case. Other body forces such as electromagnetic forces are assumed to be negligible. Therefore, the fluid behavior is mainly characterized by the thermal and solutal Rayleigh number defined in eq (2.37). The material parameters used in the calculation are compiled in Table 5.6 for $T = 600\,°\mathrm{C}$. In order to harmonize with the definition of the Rayleigh number, in the further discussion the temperature difference will be referred to as being negative for the case of heating from the top and positive for heating from the bottom. As a consequence, negative Rayleigh numbers are allowed.

Heating from top. The imposed vertical temperature gradient in the order of $\Delta T = -10\,\mathrm{K}$ gives rise to a density difference between any control volume in the lower part and in the upper part of the crucible. Because the thermal expansion coefficient of indium β is positive, the density at the bottom is higher than at the top. This density gradient tends to decelerate any initial disturbance in the stagnant fluid. The associated vertical thermal Rayleigh number is on the order of -0.5×10^5. This value is far below the critical Rayleigh number for Bénard convection and therefore, thermal convection is expected to play no role for heating from the top because the temperature gradient stabilizes the system against perturbation. In a multi component system, besides the thermal also the solutal density differences have to be considered. At the bottom of the crucible, indium is in contact with the silicon feeding tablet, and therefore, gets saturated up to the equilibrium concentration at T_{bot}. The substrate which is in contact with the solution in the upper part saturates the liquid up to the appropriate saturation concentration at T_{top}. It was shown in Section 5.1.2 that the equilibrium concentration of the binary mixture increases with increasing temperature. In order to be able to evaluate the influence of solutal expansion, the algebraic sign of the associated expansion coefficient has to be deduced. No experimental data were found for the system under consideration. Hence, a rough estimation will be used. Because the density of pure indium is greater than that of pure silicon, the density of their mixture is expected to gradually decrease with increasing silicon concentration. Hence, the solution density at the top is estimated to be lower than that at the bottom. Consequently, the solutal density gradient stabilizes the system and therefore acts in the same direction as the thermal density gradient. The main conclusion is that the solvent flow velocity due to natural convection inside the crucible is expected to be zero in the case of heating from the top. Diffusion, which is driven by the silicon concentration gradient between the upper and the lower part, is the only remaining transport mechanism. Therefore, silicon, which was dissolved at the top, feeds the silicon tablet at the bottom. Furthermore, parasitic silicon crystallites, which accidentally formed inside the solution during growth experiments and are

Parameter	Value	Unit	Ref.
Density ρ	6.684	$\mathrm{g/cm^3}$	[70]
Thermal expansion coefficient β	1.0730×10^{-4}	1/ K	[70]
Thermal conductivity λ	50.08	$\mathrm{W/(m \cdot K)}$	[71]
Dynamic viscosity η	1.219	$\mathrm{mPa \cdot s}$	[72]
Specific heat capacity c_p	27.2	$\mathrm{J/K \cdot mol}$	[73]
Molar mass M	114.82	g/ mol	

Table 5.6: Material constants of liquid indium at 600 °C.

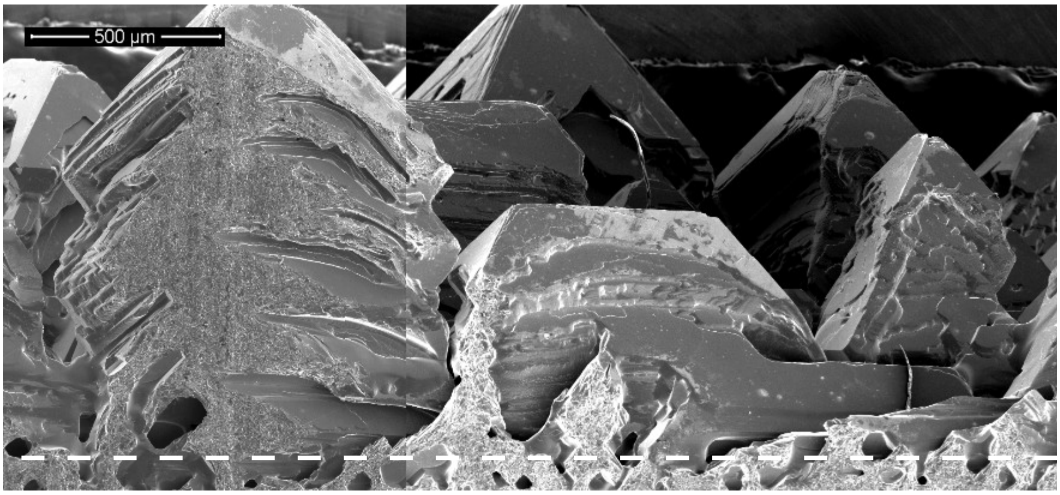

Figure 5.31: SEM micrograph showing a cutting edge of the silicon feeding source after removing indium.

floating at the solution surface, can be removed by applying this mechanism. This "recycling" or "refeeding" process is carried out for at least 8 h after each growth run and ensures that the next run starts with a crystallite free solution. Figure 5.31 presents an SEM micrograph of the [001] oriented silicon feeding tablet which was examined after several growth runs with subsequent re-feeding procedure. Indium has been removed by chemical etching to reveal the surface structure. Initially, the surface of the tablet has been flat. The alternating dissolution and growth processes lead to the formation of macroscopic silicon islands at the surface. The formation of cavities and tree–like dendrite structures indicate the growth process to be unstable.

Heating from the bottom. When heating the crucible from below, the vertical temperature gradient of about 10 K gives rise to thermal convection. The associated Rayleigh number has the same absolute value as for top heating. Because the temperature gradient is now directed in the opposite direction, the Rayleigh number must have a positive algebraic sign. Thus, the value is significantly higher than the critical Rayleigh number for the onset of thermal convection. The solutal convection amplifies this behavior. In order to reveal closer insight into the convective flow pattern, the temperature and velocity field was simulated by applying finite element simulation (FEM), which is implemented in software packages

ENTWIFE and FIDAP[1]. Simulation was carried out on the basis of experimental results regarding the applied heating power and measured temperature (T_{top} and T_{bot}) in order to achieve relevant data. The left part of Figure 5.32 shows the axisymmetric steady–state solution of the temperature and flow velocity field inside the growth container for bottom heating. The temperature difference between two adjacent isotherms is 1.3 K. The temperature isolines start at 617 °C at the feeding tablet and end at 590 °C at the outer crucible wall. The flow velocity "measured" at the inner cross is of the order of 1 cm/s. The solution was brought to convergence by starting from a stagnant fluid at zero gravity with an impressed temperature distribution due to bottom heating which fits the experimental values. By step–wise increase of the gravity acceleration to the nominal value, the convective flow was driven to the actual distribution as seen in the picture. Because the Prandtl number, which is the ratio of the kinematic viscosity to the thermal diffusivity, is about 0.006, the temperature field is mainly governed by heat conduction. The temperature distribution is only slightly distorted by the convective flow pattern. Therefore, regardless of the convective flow, the substrate is situated within a rather hot zone of the crucible. The coldest zone is fixed at the outer part of the container. This situation is not suitable to enforce silicon supersaturation in direct vicinity of the substrate. Additionally, the main flow vortex acts within the coldest zone and promotes transport from below to the outer part of the crucible. An additional transient analysis of the convective flow (not shown here) resembled the oscillatory behavior of the temperature measured inside the crucible wall.

Heating from the side. Heating from the side results in a significant horizontal temperature gradient which is directed from the wall to the inner part of the crucible. This immediately gives rise to threshold-less convection driven by bouyant forces causing the fluid to drift upwards in front of the wall. Additionally, the growth substrate is situated within the coldest zone of the solution, which enforces maximal supersaturation in the direct vicinity of its surface. The right part of Figure 5.32 shows the associated FEM simulation of the temperature and flow velocity field. The temperature difference between adjacent isotherms is 0.8 K. The temperature distribution starts at 680 °C at the growth substrate and ends at 696 °C at the crucible wall. The main flow vortex acts with an average velocity of about 2 cm/s within the hottest zone of the solution and contributes to solute transport from the feeding source to the growth substrate.

---

[1] The numerical simulation presented here was carried out by Dr. Klaus Böttcher

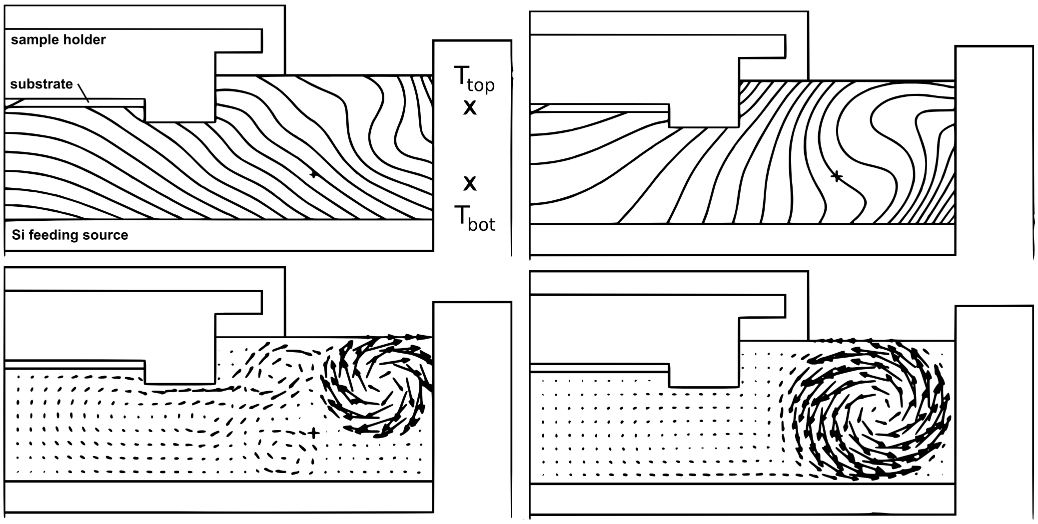

Figure 5.32: Steady–state FEM solutions of temperature and flow velocity field for bottom heating (left) and top heating (right).

In summary, the latter heating configuration was found to be suitable for solution growth of silicon at low temperatures. Re-feeding of the silicon source is possible by applying a vertical stabilizing temperature gradient which causes the fluid to stay at rest. In this case, transport of silicon is driven by diffusion which arises due to the concentration gradient between top and bottom.

5.6 Seed Crystal Enlargement by Steady–State Solution Growth

This section presents the results on the enlargement of the seed crystals on Mo–Si multilayers coated with a protective molybdenum interlayer by applying steady–state solution growth.

5.6.1 The Role of the Critical Grain Size

Kühnle et al. were the first to figure out the role of the critical grain size on the success of the enlargement of seed crystals from solutions. They showed that seed crystals whose size exceeds the critical grain size for nucleation are selectively outgrown by the supersaturated solution whereas smaller seeds disappear. This can be explained by applying classical nucleation theory for the case of homogeneous nucleation. Assuming a spherical nucleus, the critical radius is given by eq (2.19).

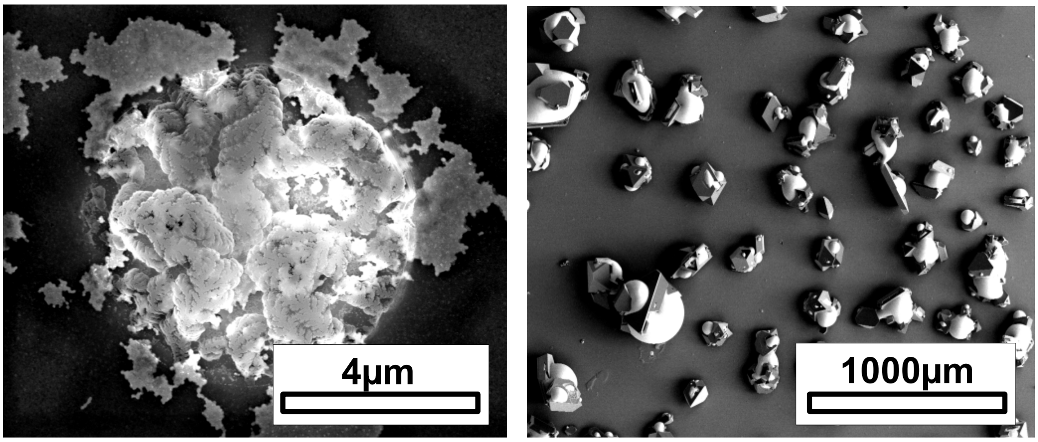

Figure 5.33: SEM micrographs of samples after solution contact for 4 h at 610/620 °C with their VLS deposition parameters adjusted (left) for dendrite growth without seed crystals, and (right) for growth of seed crystals (see Figure 5.28).

In order to decide whether the size of our seed crystals exceeds the critical value and is therefore applicable for outgrowth the specific energy of the interface between the crystal and the solvent has to be known. Very little data is found in the literature which characterizes the liquid–solid interaction in the system under consideration here. Kühnle et al. estimated the critical grain size for their experiments by using literature data valid for Si(001) in contact with indium. For a rough estimation, the same data will be used in the calculation here. For liquid indium which is saturated with c–Si at 610 °C and cooled down to 600 °C, the driving force $\Delta^{l,s}\mu$ can be found in Table 5.3. With $\gamma_{l,s} = 1.66\,\mathrm{J\,m^{-2}}$ and $\Omega = 12.1\,\mathrm{cm^3\,mol^{-1}}$ the diameter of the critical nucleus equals $2R_c \approx 80\,\mathrm{nm}$. This is only about 1 % of the actual size of a typical seed crystal grown by the VLS–mechanism. Therefore, in our case the influence of the critical grain size can be neglected.

5.6.2 Pre and Post Solution Growth Comparison

Experimental results described here were obtained by using templates which were processed as illustrated in Figure 5.27. Silicon was deposited at either high or low rate (see Section 5.4). The droplet distribution was checked by using the in situ SEM mounted on top of the handler chamber. The subsequent steady–state solution growth step was carried out by heating the solution from the side providing best possible fluid flow and saturation conditions. The nominal temperatures at the crucible walls were $T_{top} = 610\,°C$ and $T_{bot} = 620\,°C$, respectively. The growth time was 4 h in each case. Figure 5.33 illustrates the influence of the solution contact on the sample surface. In the left part, the vapor–liquid–solid deposition parameters were chosen in a way that no seed crystals were present. The SiO_x dendrites which had overgrown the droplet collapsed as the underlying indium is merged with the growth solution. As expected, this case was proven to be unsuitable for growth of silicon crystallites on glass. This result strengthens the concept of seed crystal deposition which must preceed the epitaxial enlargement. In the right part of Figure 5.33 the influence of the growth solution on existing seed crystals which were deposited at higher rate is shown. The grown crystals have a typical diameter of 50–200 µm. This means that the diameter of the seed crystals was increased by a factor of at minimum 10 due to the solution contact. Residual indium sticks at the grown crystals and appears as bright spheres in the SEM images. The left part of Figure 5.34 shows a $4 \times 4\,\mathrm{cm}^2$ glass substrate which was overgrown with silicon crystals proving the feasibility of the process in a macroscopic scale. Generally, the lateral dimension of the grown crystals is of the same order as the vertical diameter. Therefore, the origin of the ordinary crystals is concealed by the crystals themselves and it is difficult to visualize the initial nucleus. Defects such as twin boundaries result in anisotropic growth rates and plate–like crystals form (see Section 5.6.5) which uncover the view on their origin. An example is shown in the right part of Figure 5.34. In this way, grown crystals were found to directly originate from the position of a seed crystal. The circular imprint of the original indium droplet with seed is marked with an arrow.

5.6.3 Crystallinity and Texture Analysis

Raman spectra of grown silicon crystallites were recorded using an incident laser beam with a wavelength of 633 nm. The spectra have been normalized in respect to their maximum and are shown in Figure 5.35. Crystalline silicon is Raman active with a sharp peak around $521\,\mathrm{cm}^{-1}$ [63, 7]. This characteristic peak arises due to the LO–TO phonon resonance. The peaks were analyzed by fitting a Voigt profile. By this means, the peak position of the exemplary crystallite and the associated FWHM have been determined to be $520.5\,\mathrm{cm}^{-1}$ and $4.04\,\mathrm{cm}^{-1}$, respectively. Both values are in good agreement with data for single–crystalline silicon measured in this work ($\nu_c = 520.62\,\mathrm{cm}^{-1}$ and $\mathrm{FWHM} = 3.62\,\mathrm{cm}^{-1}$) and also with data from the literature [74, 65], except for the slight broadening of the peak.

In 1966, Bliznakov et al. considered the nucleation of materials with diamond lattice

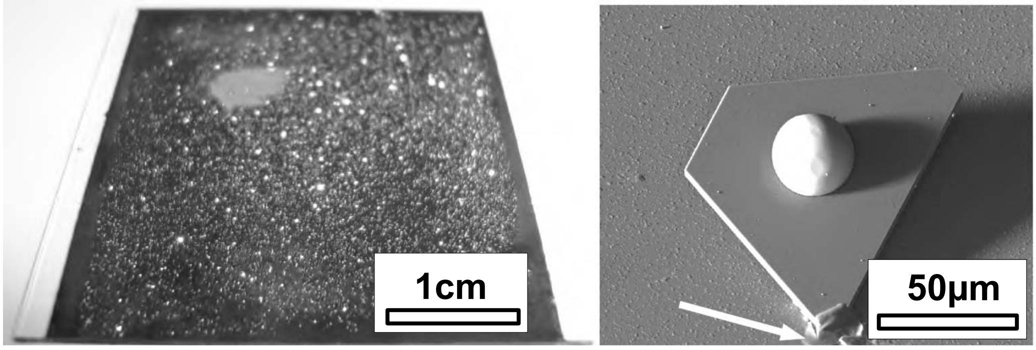

Figure 5.34: Photograph of a $4 \times 4\,\mathrm{cm}^2$ glass substrate coated with $MoSi_2$ and overgrown with silicon crystals, 45° tilt SEM micrograph of a silicon crystal directly originating from a seed.

(like silicon) on structureless substrates [75]. They concluded that at low supersaturation, a [111]–oriented nucleus must have the lowest energy of formation. To check the orientation distribution of the seeds which nucleated inside the solvent droplets and were enlarged by steady–state solution growth technique, a texture analysis was conducted by means of the X–ray diffractometer. The Si 111 reflection was chosen for its highest intensity. By measuring several independent (hkl) reflections, a orientation distribution function can be derived. The latter procedure is limited to flat polycrystalline layers, because here shadowing effects do not play a role. In our case, due to the presence of free–standing faceted crystals, information is getting lost due to the shadowing effects. Therefore the deviation of the exact orientation distribution function by this method must fail. Nevertheless, a first overview on the orientation distribution can still be deduced from the measurement of a single plane. To eliminate the influence of the angular dependence of the background, the steps of sample tilt and rotation were adjusted in a way that the covered solid angle remained constant for each step. Figure 5.36 shows stereographic projections of simulated (left) and measured (middle and right) data. First, the angular distribution of the {111}–planes of a [001]–oriented silicon single crystal was measured for reference purpose. The left part of Figure 5.36 shows the associated stereogram as derived using [76] with $\beta' = 25°$. The angle between the displayed {111} and the (001) lattice planes of $\alpha = 35.264°$ is resembled in the measured data (middle). The right part of the figure shows the measured angular distribution of {111} planes of silicon on glass grown by steady–state solution growth technique. In contrast to

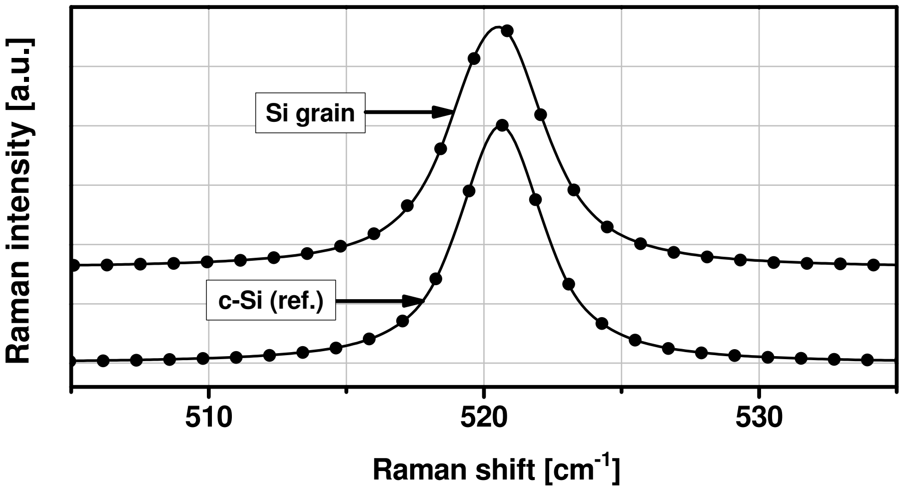

Figure 5.35: Normalized Raman spectra of a silicon grain grown on glass and a single crystalline reference, curves fitted by Voigt profile.

the single crystalline material, here a high quantity of apparently random oriented reflection spots was detected. Besides these, there seems to exist an accumulation of {111}–poles near the center of the pole figure. Especially at $\alpha = 0$ the spot with the highest intensity was measured. This reflection might originate either from a large single grain or from several grains which are [111] oriented with respect to the sample surface. From the crystal structure of silicon one can derive that the 3 additional {111} reflections in the upper hemisphere associated with this mutual grains must exhibit a tilt angle of $\alpha = 70.529°$ and thus cannot be detected by this system because of the limitation of the goniometer.

5.6.4 Purity and Electronic Properties

An important question regarding the suitability of a material in electronic devices and especially in photovoltaics is the purity of the grown material. Impurities reduce device performance by either reducing the carrier diffusion length, induce degradation by precipitation and inclusions or a combination of both. Hopkins compiled measurements of the impact of several metallic impurities on solar cell performance [77]. He found that the efficiency gradually starts to decrease as a certain threshold impurity concentration is exceeded. The threshold impurity concentration depends on the type of material.

To get a first insight into the concentration of several common impurities in the

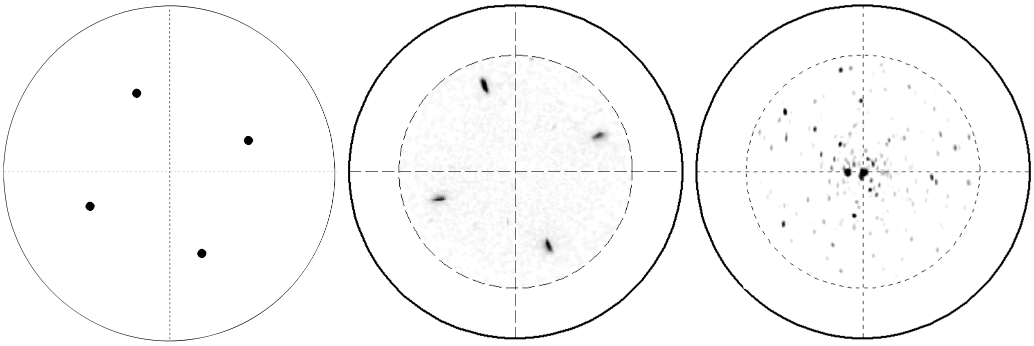

Figure 5.36: Stereographic projection of {111}–lattice planes of a [001]–oriented Si crystal (left), measured orientation distribution of a Si–[001] crystal (middle) and of Si on glass (right).

grown material, selected crystals were analyzed by means of secondary ion spectroscopy (SIMS) depth profiles. By this means, impurity concentration can be measured down to the detection limit which equals about 1×10^{15} atoms/cm^3 in the utilized setup.

To be able to achieve valid data, a flat sample surface whose surface normal is parallel to the primary ion beam must be prepared. During measurement, the primary ion beam covers an area of at least $90 \times 90\,\mu\text{m}^2$. The actual measuring area only amounts to a low fraction of the whole eroded area to prevent edge effects and shadowing. Therefore, grown twin platelets (see Section 5.6.5) were chosen for the SIMS preparation as they exhibit large flat {111} facets and barely fulfill the needs of the SIMS method. The left part of Figure 5.37 shows a SEM micrograph of a processed sample. The platelet is fixed in a Sn–matrix. Two sputter craters are clearly visible, one producing a hole through the crystal. One measurement run is restricted to the analyzation of 2–4 elements at once. A total of three crystallites was analyzed. As the SIMS sputtering is a destructive method, different elements had to be measured at different crystallites. This constrains the comparability of the respective results. Figure 5.38 shows the absolute measured impurity concentration over sputter depth for the three crystallites. First, the content of carbon together with the oxygen concentration was measured using Cs ion bombardment. Except for the material sputtered near the surface, both the oxygen and the carbon content were found to be uniformly distributed in the measured part of the crystallite. This uniformity is only seldom disturbed by oxide–containing inclusions

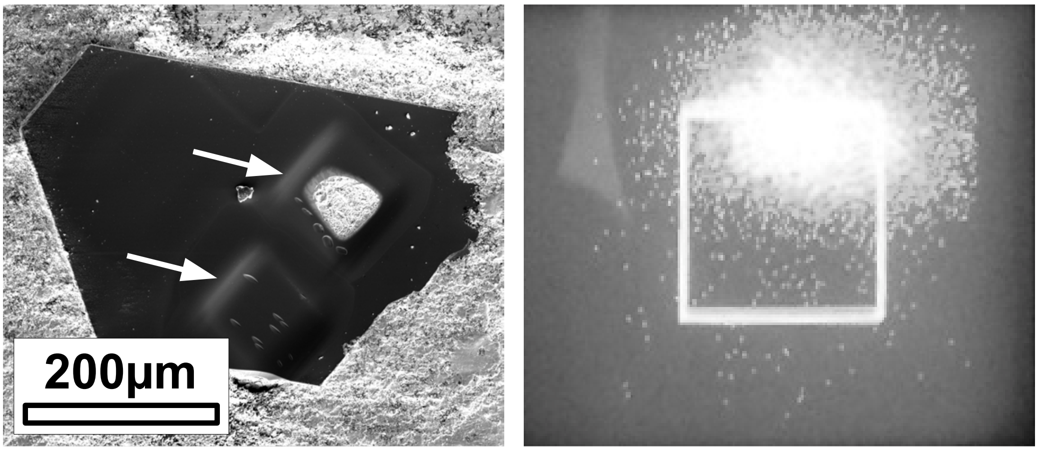

Figure 5.37: SEM micrograph of embedded Si twin platelet after SIMS measurement showing two sputter holes, spatial distribution of oxygen secondary ions during the penetration of a mutual inclusion.

which cause sharp peaks in the graph of the oxygen content. This effect can be seen between a depth of 8 and 9 µm in the presented profile. The associated spatial distribution of oxygen ions is depicted in the right part of Figure 5.37. The average bulk concentration was found to be 4×10^{16} atoms/cm^3 in the case of oxygen and 5×10^{16} atoms/cm^3 in the case of carbon. This is at least about 2 orders of magnitude below the impurity threshold concentration for the onset of electronic device degradation (C: $> 1 \times 10^{18}$ atoms/cm^3 [77], O: $> 1.2 \times 10^{19}$ atoms/cm^3 [78]).

Two additional measurements were carried out using a primary oxygen ion beam. Na was detected with a non–uniform distribution and a minimal concentration of 1.5×10^{15} atoms/cm^3 in the particular crystallite. The copper concentration was found to be near the detection limit of the apparatus, amounts to 1×10^{16} atoms/cm^3 and again lies far below the threshold concentration of $> 1 \times 10^{17}$ atoms/cm^3 [77]. The incorporation of molybdenum and indium is of special interest as both materials are directly involved in the crystal growth process. According to the measurements of Hopkins, besides other related transition metals, molybdenum is found to reduce carrier lifetime even at concentration as low as 1×10^{12} atoms/cm^3. The actual concentration was found to be below the detection limit of the spectrometer of 1×10^{15} atoms/cm^3 in the case of molybdenum. Therefore, a degrading influence of molybdenum cannot finally be ruled out. The indium content was measured to be

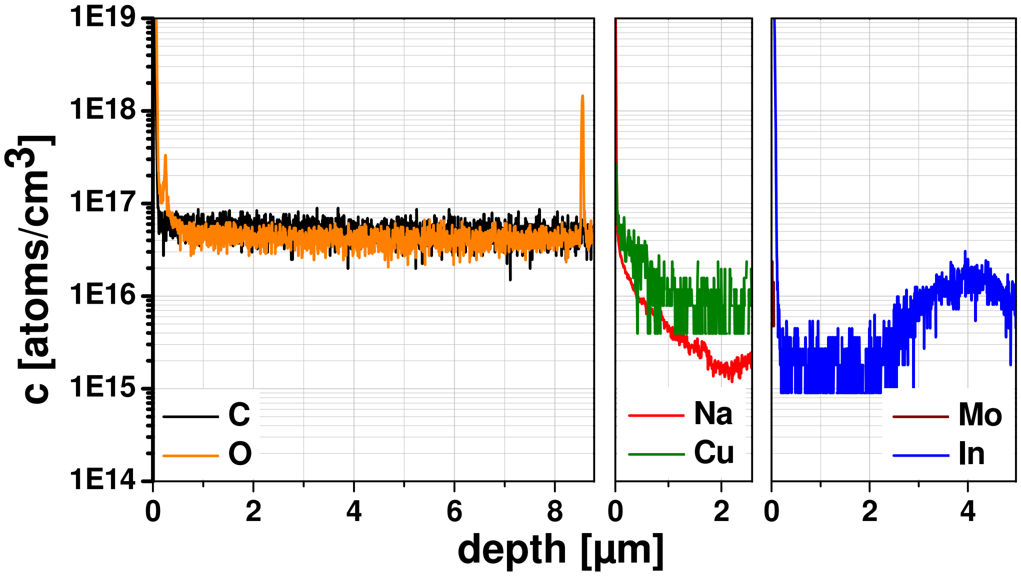

Figure 5.38: SIMS depth profiles measured at three different crystallites, C/O with Cs primary ion beam, Na/Cu and In/Mo with O primary ion beam.

as low as 1×10^{15} to 2×10^{16} atoms/cm^3. This ranks lowest as compared to other indium solution growth techniques conducted at higher temperature like conventional liquid phase epitaxy (2×10^{16} atoms/cm^3 at 940 °C) and high temperature solution growth (2×10^{18} atoms/cm^3 at 1290 °C) [79].
Only few crystallites could be analyzed by means of SIMS measurement. Therefore, the obtained data is only showing the potential of growing silicon crystallites with high purity at low temperatures.

5.6.5 Crystal Morphology and Modes of Crystal Growth

This section describes the typically observed growth morphologies and proposes the underlying growth mechanisms.

Crystal Faceting

All crystals grown by steady–state solution growth technique were found to be terminated by {111} facets. This is illustrated in Figure 5.39 which shows a SEM micrograph of a typical crystal together with its redrawn shape using [80]. The outer shape can be exactly resembled by solely use of {111} facets in the construction. The holes filled with indium which remain at the center of the facets are due to

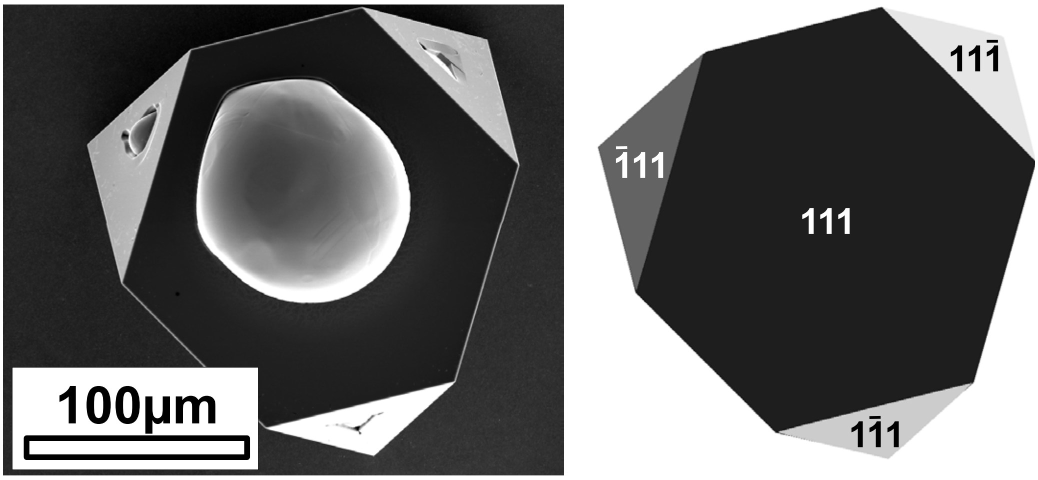

Figure 5.39: SEM micrograph of a $\{111\}$–faceted silicon crystal with crystal shape redrawn using [80].

a developing morphological instability and will be discussed later in this section. It is widely known that, in the diamond structure, the $\{111\}$ facets exhibit the lowest growth rate. Two terms contribute to the kinetic coefficient and therefore to the growth rate: the interkink distance and the attachement kinetics. The attachment kinetics are strongly influenced by the solid–liquid interaction at the phase boundary. As these interaction at the interface is not well quantified in detail yet for the case of silicon growth from indium, the author will focus the discussion on the kink density.

The existence of kinks is a consequence of morphological, thermal and kinetic roughness. First the morphological roughness will be discussed. From the crystal structure of silicon, the directions of the six P.B.C. vectors can be easily derived. In the absence of thermal and kinetic roughening ($T = 0$, $\Delta\mu = 0$), the kink density function must equal zero where two or more P.B.C. vectors intersect. The same holds for the case of the surface normal vector being perpendicular to one P.B.C. vector. Here, the kink density function must exhibit a sharp cusp, as small miscuts would increase kink density significantly. Individual cusps generated by the respective P.B.C. directions were combined by applying the cusp combining operation proposed by van Suchtelen et al. [20]. Figure 5.40 shows the normalized kink density in a stereographic projection. The dark zones trace the directions of the

P.B.C. vectors. F–faces can be extracted by finding the poles where two or more P.B.C. traces intersect. It can be seen that solely the $\langle 111 \rangle$ and $\langle 100 \rangle$ direction correspond to flat faces (F), each built by the intersection of three and two strong bonded chains, respectively. The $\langle 110 \rangle$ directions are stepped. A particular situation emerges for the $\langle 100 \rangle$ directions, where two P.B.C vectors intersect but their respective strong bonded chains are not coplanar. This leads to alternating smooth and kinked elementary steps, each being aligned parallel and perpendicular to the strong bond dimer rows.

To discuss the influence of thermal roughness, Jackson's criterion eq (2.43) is used to determine the respective transition temperatures. Taking the interaction energy up to the forth nearest neighbour into account, the ratio of the binding energies Ψ_{hkl}/Ψ can be derived as being equal to 0.69 for the $\{111\}$ and 0.05 for the $\{001\}$–faces, respectively [81]. It results, that the $\{001\}$–faces are expected to be thermally rough whereas the $\{111\}$–faces remain flat at 600 °C (see Table 5.7).

On thermally flat F–faces without defects, elementary steps must be created by the birth and spread mechanism ($T > 0$, $\Delta^{l,s}\mu > 0$). In order to be able to quantify the critical supersaturation needed for two–dimensional nucleation on silicon $\{111\}$ the specific step free energy must be known. In the case of growth from solution, prospective solid–liquid interaction at the phase boundary have to be explicitly taken into account. No coherent theoretical or experimental data to quantify these interaction is known to the author. Solely the qualitative nature of the solid–liquid interaction has become accessible by means of recent high–intensity X–ray reflectometry experiments at modern synchrotron radiation sources. Reichert et al. [82] point out the presence of a strong disturbance of the electronic system near the interface leading to a strong densification of indium coupled with a charge transfer from the liquid metal to silicon. The dissipated interaction energy between the atoms of the solid and the liquid at the interface must lower the step free energy thus enabling two–dimensional nucleation on $\{111\}$ even at low supersaturation.

face	morph.	therm. (steps)	therm. (face)	kin.	roughn.
[111]	flat (F)	-	flat (3720 K)	?	flat
[001]	flat (F)	-	rough (261 K)	-	rough
[011]	stepped (S)	rough	-	-	rough

Table 5.7: Determination of the morphological, thermal and kinetic roughness of the three important surfaces in the diamond lattice.

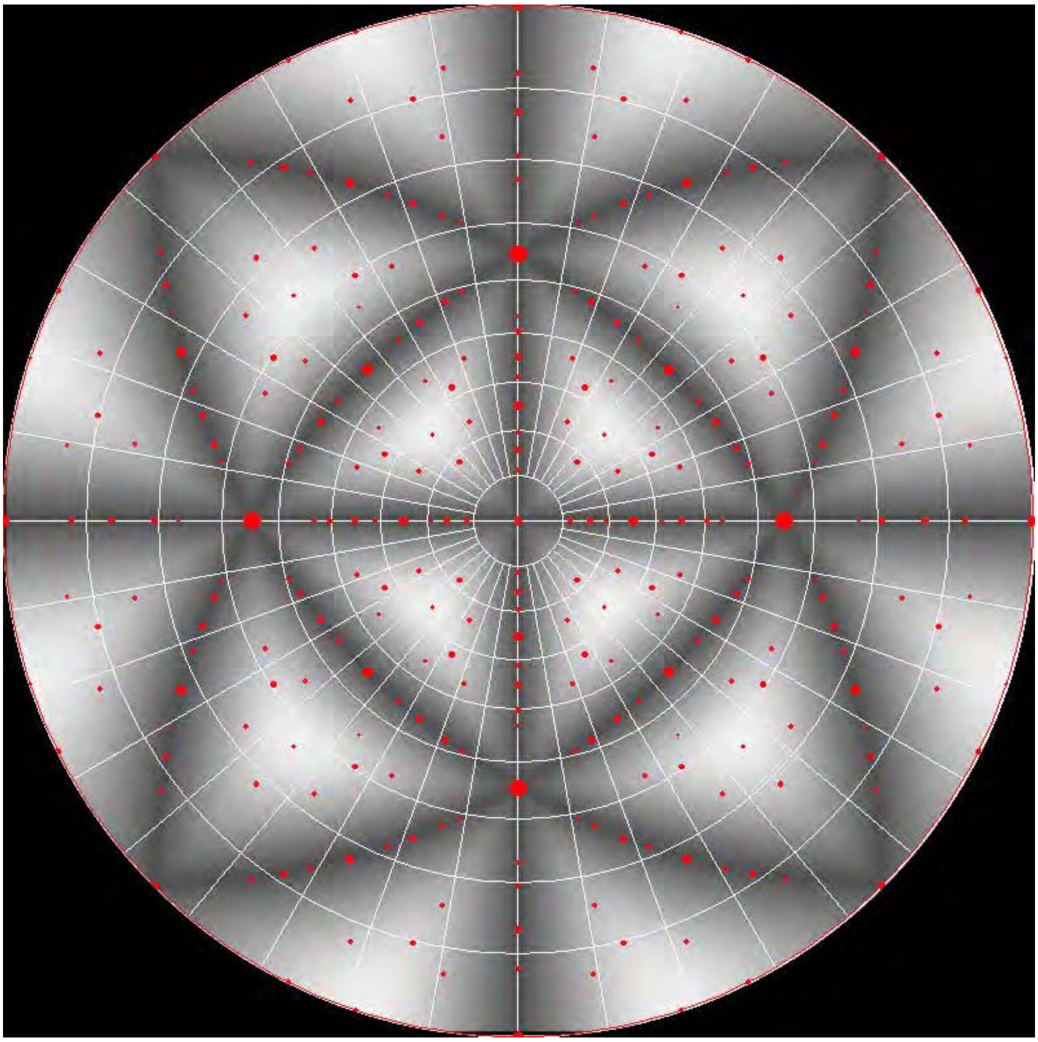

Figure 5.40: Stereographic projection of a [001]–oriented Si crystal structure (red) with normalized kink density (gray) in the absence of kinetic or thermal roughening ($T = 0$, $\Delta\mu = 0$).

From a experimental point of view, the presence of outgrown {111}–terminated untwinned crystallites proof the existence of such a mechanism. Otherwise, the arbitrary shaped seed crystals would just grow to faceted crystals and further outgrowth would be inhibited. Additionally, the onset of unstable growth leading to a hopper morphology as discussed in Section 5.6.5 indicates growth of untwinned crystals to be driven by the two–dimensional nucleation mechanism rather than by a screw dislocation.

Crystal Twins and the Re–Entrant Edge Growth Mechanism

Twinning is one of the common real structure defects observed in material grown in the steady–state solution growth apparatus. The defect involves at least one specific grain boundary which divides the crystal into two or more twin domains. The orientation of the domains is determined by one or more symmetry elements which are not part of the space-group of the crystal. These symmetry elements can either be inversion centers, an additional mirror plane or an additional rotation axis or a combination of them. Whereas applying a symmetry operation which is part of the crystal's space group brings the crystal lattice to full self–coincidence, only partial coincidence is derived by applying a twin symmetry operation.

Twin grain boundaries are usually classified by their CSL (coincidence site lattice) ratio Σ given by the fraction of the quantity of crystal lattice sites to the coincident lattice sites [83]. In the diamond A4 structure, commonly $\Sigma = 3$ twin boundaries form [84]. To construct the twin domain associated with a $\Sigma = 3$ twin boundary, the crystal is cut along a {111} plane. Now, the twin domain can be constructed by a rotation of 60° about the $\langle 111 \rangle$ zone direction. The $\langle 111 \rangle$ zone directions contain a three–fold symmetry which is described by a rotation by 120°. Therefore, the described operation is not part of the crystal's space group.

Figure 5.41 clarifies this situation by showing the $[11\bar{2}]$–view of a twinned crystal, which consists of two domains, as it was grown by steady–state solution growth. The two domains are denoted with c (crystal) and t (twin), respectively. Both domains are terminated by {111}–facets. The twin boundary is marked with a white arrow. The right part of the figure shows the associated stereographic projection of the poles of both domains. The $\langle 111 \rangle$–directions correspond to the circles and spots with the greatest diameter, respectively. In both pictures the [111] zone direction is marked with a continuous line. The rotation by 60° around the [111] direction is indicated by the dashed line of the stereogram.

A closer examination of the material grown by steady–state solution growth revealed

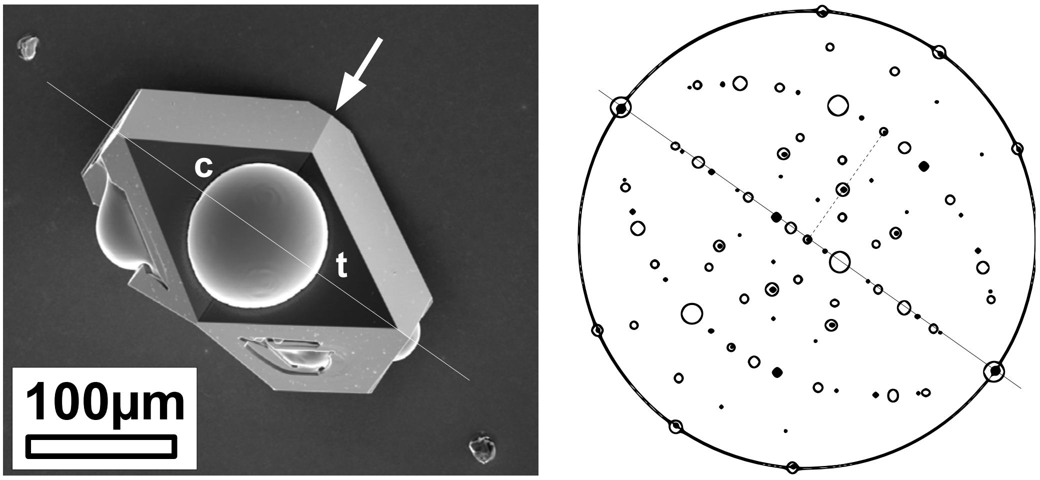

Figure 5.41: SEM micrograph of a {111} faceted crystal exhibiting a $\Sigma = 3$ twin boundary (arrow), double stereographic projection of both twin domains, open circles–crystal (c), dark spots–twin domain (t).

the common presence of twinned crystals containing multiple $\Sigma = 3$ twin boundaries. The consecutive twin boundaries are either parallel (polysynthetic twin) or enclose an angle of 70.528° which is the angle enclosed by two adjacent {111} facets. The latter case leads to the formation of a twin quintuplet as shown in the left part of Figure 5.42. The domains are strung alongside the [110] zone trace. The emerging five $\Sigma = 3$ twin boundaries are marked with continuous arrows in the figure. The repeated angular enclosure of $5 \times 70.528°$ leads to a shortage of 7.36° in respect to 360° which is absorbed in an additional grain boundary. This additional boundary is marked with a dotted arrow in the SEM micrograph. An interesting fact is that in diamond twin quintuplets grown by chemical vapor deposition technique [84] only four $\Sigma = 3$ twin boundaries form. The misfit is reported to be absorbed in a $\Sigma = 81$ boundary. In contrast to these findings, $\Sigma = 81$ twin boundaries were not observed in the case of silicon grown from indium solution.

Polysynthetic twins consist of multiple parallel twin boundaries. In the present case of $\Sigma = 3$ the twin boundaries are aligned parallel to the major {111}–facets which terminate the top and the bottom of the sandwich–like structure (see Figure 5.42). On the sides this leads to the formation of alternating ridges and grooves, denoted with R and G, respectively. At the grooves, a re-entrant angle of 141.1° is enclosed by two {111}–facets. Obviously, this alternating structure promotes faster

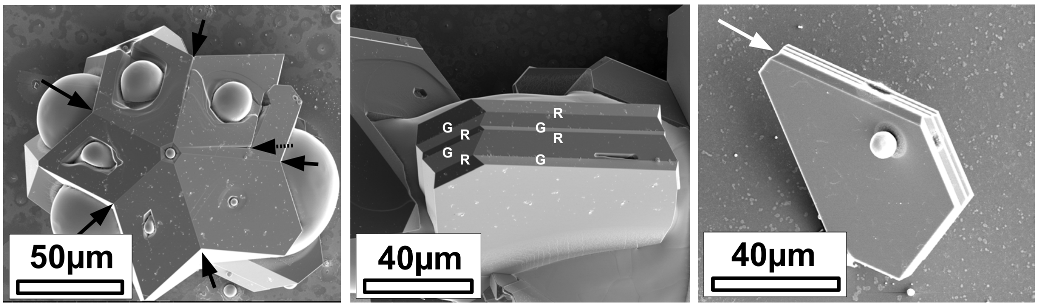

Figure 5.42: $\Sigma = 3$ twinned crystals exhibiting multiple twin boundaries which enclose an angle of 70.528° (cyclic) and are stacked on top each other in a parallel way.

growth rates in the $\langle 112\rangle$–directions perpendicular to the major [111]–direction. As a result, grown polysynthetic twins exhibit highly anisotropic plate–like structures . This anisotropy can be explained by the twin–plane re-entrant edge growth mechanism that Faust and John first described in 1964 [85]. Besides the presence of a self–preserving re-entrant edge formed by two adjacent facets at a twin boundary, the re-entrant edge growth mechanism requires the growth direction being parallel to the twin plane. Figure 5.43 shows the interpretation of the mechanism for silicon on an atomic scale. The crystal structure is projected along the $[1\bar{1}0]$–direction. The twin plane forming the re-entrant edge is vertically aligned at the middle of the drawing and generates local mirror symmetry. The two atoms directly at the edge have their dangling bonds directed towards the opposed facet, respectively. This site is likely for the attachment of a elementary growth unit, which is built by two atoms in the diamond A4 structure. The same mechanism proceeds at the other edge sites aligned parallel to the $[1\bar{1}0]$–direction. In this way, a structure which is similar, but not exactly equal to two elementary steps on $\langle 111\rangle$ is assembled, both aligned along the $[1\bar{1}0]$ direction. They are produced without the need for two–dimensional nucleation and immediately give rise to further conventional step–flow in the $[\bar{1}\bar{1}2]$ direction indicated by the two open arrows in Figure 5.43. As a result, the edge grows in the $\langle 112\rangle$ direction parallel to the twin plane which is denoted with a filled arrow in Figure 5.43. The atomic structure is exactly resembled as the new layer has formed and growth along the twin plane proceeds in a continuous way. In contrast to two–dimensional nucleation this process does not require building up a critical supersaturation. This leads to an enhanced growth rate and the formation of twin platelets. In addition, this mechanism enables fast growth of material even

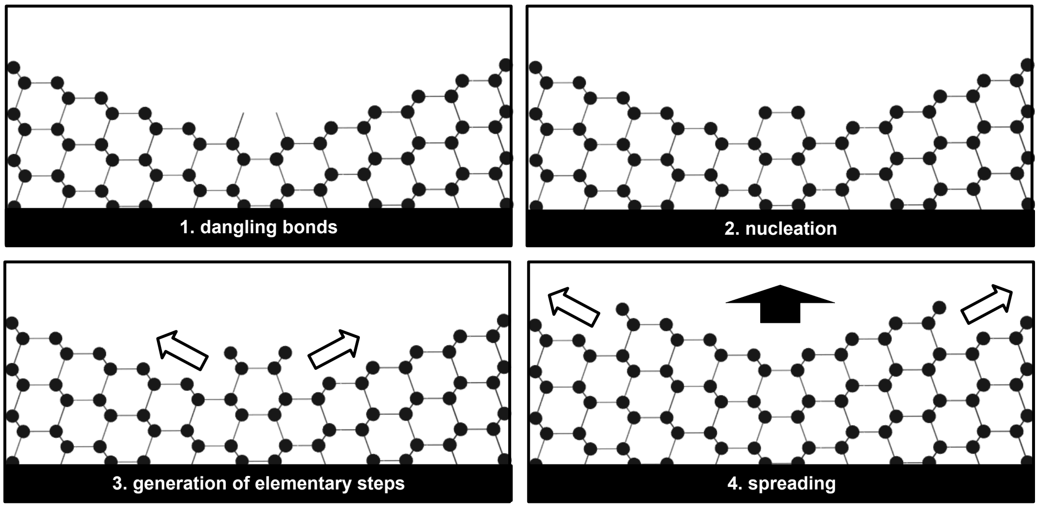

Figure 5.43: $[1\bar{1}0]$–view of the twin–assisted re-entrant edge growth mechanism, birth and spread of elementary steps at the groove (not all dangling bonds are drawn for clarity).

at supersaturation below the transition to kinetic roughening. This behavior is very similar to that of growth at a screw dislocation described by Burton et al. in 1951 [21].

The Development of the Morphological Instability

A further effect, which has not been discussed yet, is the growth of polyhedral crystals which exhibit a hole at the center of their facets as depicted in Figure 5.39. This morphological feature is often referred to as “hopper” or “skeletal” [25, 18]. In the present case, the remaining hole is usually filled up with indium. These results can be explained by the development of a morphological instability which arises from a non–uniform solute concentration above the growing crystal. In the following, the steady–state solution growth technique will be shown to comply with the requirements of unstable growth conditions leading to hopper morphology as described by Kuroda et al. [86]. Conclusions will be drawn about the growth regime needed to enable stable growth of silicon from indium solution.

In Section 2.2.2 convective flow parallel to a semi–infinite horizontal surface has been discussed resulting in the presence of a stagnant boundary layer in the vicinity of the surface. The thickness δ_m of the stagnant boundary layer is a function of the distance from the leading edge of the surface x, the viscosity η, the liquid density ρ and the characteristic fluid flow velocity V (see eq (2.33)). When heating from side,

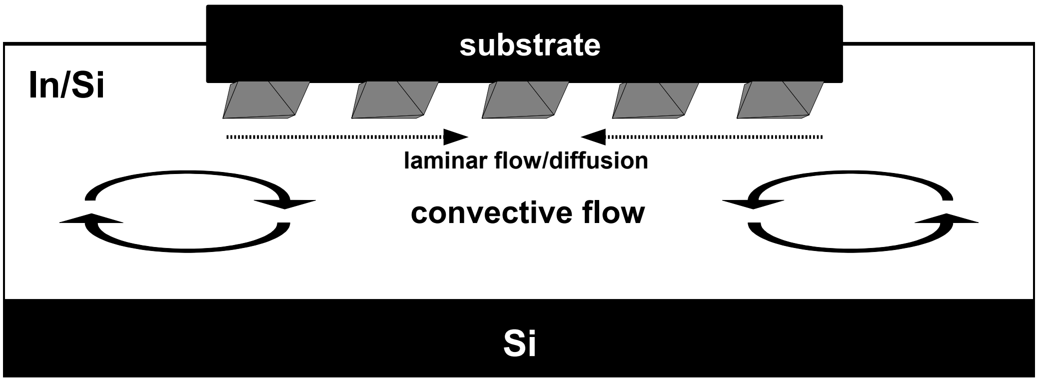

Figure 5.44: Convective flow and laminar boundary layer in the steady–state solution growth apparatus.

liquid indium ($\eta = 0.00122\,\mathrm{Pa\,s}$ [72], $\rho = 6893.8\,\mathrm{kg/\,m^3}$) flows along the $4 \times 4\,\mathrm{cm}^2$ growth substrate with a characteristic velocity of $2\,\mathrm{cm/\,s}$ (see Section 5.5). Using $Sc = 15.7$ [87] and combining eqs (2.33) and (2.33) the thickness of the solute boundary layer can be estimated to range from 180 µm near the edge of the sample ($x = 1\,\mathrm{mm}$) to 840 µm ($x = 20\,\mathrm{mm}$) at the center. In the adjacent bulk liquid, the solute concentration c_∞ is assumed to equal the equilibrium concentration of silicon at $T = T_{bot}$. As silicon is consumed by growing crystallites at the surface, the emerging concentration gradient gives rise to diffusive solute transport from the bulk liquid to the growing crystals. Enlarged crystals reach a size of 50–200 µm. Therefore, it can be assumed that they remain fully enclosed inside the diffusion boundary layer during growth period. Therefore, the enlarged crystallites are grown in a convection–free environment which is a necessary condition for the development of a supersaturation inhomogeneity near the growing facets [88].

The existence of such an inhomogeneity in the case of faceted growth of crystallites from solution was first experimentally found by Berg [89]. The solute concentration adjacent to corners of the growing crystal is found to be higher than at the centers of the respective facets. This is a result of the solvent being rejected at the growing interface due to a distribution coefficient near zero. For geometrical reason, near the corners, the rejected solvent can dissipate into a larger volume than near the center of a facet. This leads to a relative solute depletion near the center of a facet and thus the rate of advance of a step is reduced in this region. The growth rate

$R(x)$ perpendicular to the (stepped) singular interface is given by

$$R(x) = |p(x)|v(x) \tag{5.14}$$

Here, x denotes the position at the growing interface, $v(x)$ is the local step velocity which is a function of the local supersaturation and $|p(x)| = d/\lambda(x)$ (d–step height, $\lambda(x)$–interstep distance) is the local slope of the interface. The interface grows stable if

$$R(x) = R \quad \forall x \tag{5.15}$$

For further discussion one needs to distinguish between the two possible sources for elementary steps in the case of an untwinned crystal below the transition to thermal roughness. First, these steps can be generated by screw dislocations. This defect causes the step spiral to propagate in radial directions from the central position. It follows that the screw dislocation acting as the step source can be expected to be located near the center of a growing facet. Therefore, the lower supersaturation near the center is the growth rate limiting factor for the whole facet in this case and the precondition for unstable growth is not met. In the second case of the steps being generated by two–dimensional nucleation, the growth rate will be determined by the largest supersaturation near the edges. This growth rate cannot be maintained as steps propagate to the center of a facet and the situation implies the potential of unstable growth. Therefore, the case of a birth–and–spread mechanism will be discussed.

Following Chernov, condition in eq (5.15) can be fulfilled even in the presence of inhomogeneous supersaturation by a variation of the local interstep distance which compensates the differences in the local step velocity [18]. The step density has to increase near the center in order to ensure uniform growth rate all over the facet. In other words, the local kinetic coefficient is increased within a certain limit at the center of the facet in order to sustain stable growth. This again decreases the local supersaturation and the efficiency of the compensation mechanism decreases as the local slope is increased. As the supersaturation inhomogeneity is a function of the length h of the facet, the compensating effect cannot be sustained if the crystal exceeds a certain critical size. This results in a morphological instability and hopper growth as it is observed in present steady–state solution growth experiments.

Figure 5.45 shows homo-epitaxial silicon islands grown from indium on a [111]–oriented substrate. Growth has been initiated by a fast cooling step of 100 K starting at 700 °C. This enables nucleation on Si(111) without any preceding etching step.

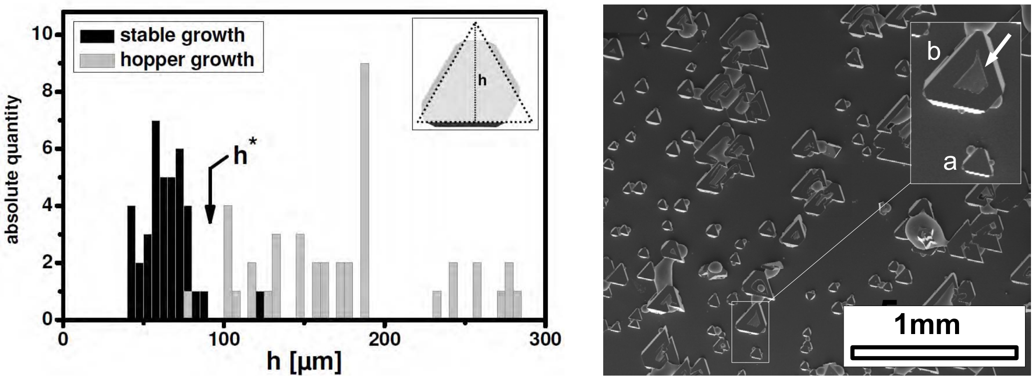

Figure 5.45: Size distribution and SEM micrograph of epitaxially grown islands on Si(111) grown stably (a) and exhibiting hopper morphology (b).

Subsequently, growth was maintained by steady–state growth period at $600\,^{\circ}\mathrm{C}$ with a nominal temperature gradient of $10\,\mathrm{K}$. Each island was analyzed by means of an image processing software to determine a characteristic length which was chosen to be the height h of the triangle enveloping the upper (111)–facet. The size distribution of stably grown islands and islands exhibiting hopper morphology is shown in a histogram in Figure 5.45. The size of the perfect islands does not exceed a critical length of $h^* = 90\,\mu\mathrm{m}$ while the size of the hopper islands clearly exceeds this value. To be able to quantify the conditions for the onset of the instability, the kinetic coefficient for growth of silicon from an indium solution must be known. The kinetic coefficient is a function of the interkink distance λ_0, which in turn depends on the specific energy of the elementary step [18, 21]. The specific energy of a step is expected to be strongly influenced by the solid–solvent interaction and might be accessible only by means of computer simulation. Qualitatively, to prevent the onset of the instability, the author suggests the development of a growth temperature regime which inserts periods where growth stops and therefore the inhomogeneity can be dissipated. As this goes beyond the scope of this work, this should be part of future investigation.

6 Summary

In this work microcrystalline silicon on glass substrates has been obtained by steady–state solution growth for the first time. Basic physical principles underlying the preceeding seed crystal formation as well as the low temperature solution growth step have been analyzed. The conclusions drawn from these findings were implemented in experimental processes to show the feasibility and to adjust the relevant parameters. Grown material was investigated by means of X–ray investigation, SIMS and Raman spectroscopy. Growth shape and common defects like twinning and the onset of a morphological instability have been analyzed and discussed.

First, based on thermodynamic principles, temperature dependent phase equilibria of the materials involved in the process have been evaluated. This lead to the possibility to quantify the potential of solution growth regarding supersaturation and layer thickness. This potential has been discussed in particular for the case of growth at low temperatures. To ensure feasibility of solution growth, the thermodynamic stability of all materials involved in the process has to be ensured. Here, molybdenum, which has been used in former experiments, was shown to be thermodynamically unstable against silicon saturated indium. The author suggested the replacement of the use of molybdenum by the thermodynamic stable molybdenum disilicide.

Thin films of molybdenum disilicide on glass were obtained by co-deposition of stoichiometric Mo–Si multilayers with a subsequent annealing step. Crystallinity and surface properties were investigated as a function of deposition parameters and annealing procedure. Thermodynamic as well as mechanical stability of the emerging layers in contact with the growth solution has been shown.

A comparative study of nucleation and wetting behavior of indium on molybdenum and molybdenum–silicon multilayer structures has been carried out in order to control droplet size and density. The remarkable temperature dependence of the success of microdroplet growth on multilayers has been studied in detail using a pyrometric camera. Partial dissolution of the amorphous silicon and simultaneous crystallization has been observed and explained by thermodynamic considerations. An alternative approach for seed formation based on the observed indium induced amorphous to crystalline transition has been developed and is under investigation at the moment.

The spatially controlled vapor–liquid–solid growth of silicon seed crystals has been investigated by variation of the vapor supersaturation. Suitable growth rates have been determined experimentally.

A specially built steady–state solution growth apparatus has been successfully applied for homo-epitaxial growth of a significant amount of crystalline silicon at low temperatures. The fluid flow and saturation conditions applying different heating configurations have been analyzed in a detailed experimental study. Basic solute transport phenomena were characterized by means of a Rayleigh analysis. The experiments were supplemented by finite–element simulation conducted in collaboration with the numerical modelling group of the IKZ.

The findings were assigned to the outgrowth of silicon seed crystals on glass substrates. The solution growth technique was shown to enable enlargement of seeds by a factor of 10–20 in few hours. Emerging crystallites were investigated by means of SEM/EDX measurement to reveal their morphology and macroscopic defect structure. {111} faceting of the crystallites was explained by means of basic principles of crystal growth like morphological, thermal and kinetic roughening and their respective transition temperatures. Particular defect–induced growth anomalies were studied by their underlying growth mechanisms. Twin assisted nucleation of elementary steps and the premises for the onset of a morphological instability leading to hopper–like morphologies was discussed.

Grown material was investigated by means of X–ray and Raman analysis to reveal crystallinity and orientation as well as secondary–ion mass spectroscopy to find the concentration of impurities.

7 Outlook

In Section 5.3.5 the indium mediated transition of amorphous to crystalline silicon has been observed at temperatures as low as 305 °C. This behavior has been explained by means of thermodynamic principles. In a preliminary investigation, we made use of an expanded approach to the deposition and crystallization of a seeding layer. In contrast to the former experiments, a noticeable greater thickness was chosen for the silicon layer. This enables the transformation of a significant amount of material from the amorphous to the crystalline phase. Figure 7.1 shows SEM micrographs of a glass sample which was coated with 2 µm of amorphous silicon. Subsequently, indium was deposited and the sample was heated to a temperature of about 300 °C. After annealing for 30 min, the sample was handed out the deposition chamber. At low magnification images, indium is found to assemble on the substrate in two different forms. Besides the formation of sub–micron scaled droplets, nearly circular domains are formed, where indium coalesced to form larger droplets. Here, a strong interaction of the liquid metal and the subjacent silicon layer is observed. Like in former experiments (see Section 5.3.5) the metal was found to partly etch the amorphous silicon layer. By this means the solvent droplet gets saturated thanks to low temperature dissolution of amorphous silicon. In this way, the liquid gets supersaturated in respect to crystalline silicon because of the differences in the chemical potentials of the amorphous and the crystalline phase as shown before. This leads to the precipitation of crystalline silicon at the substrate. The crystal facets are clearly visible in the third picture of Figure 7.1. The emerging solid starts to push the indium droplet in a certain direction where further amporphous material can be dissolved and then transformed into crystallites. This direction does not seem to be random but, in fact, partly influenced by the faceted microstructure of the underlying crystalline material. This causes the crystallization process to preferably advance in a $\langle 110 \rangle$–direction. It must be mentioned that this finding is not assured by systematic studies up to now. But, if such a mechanism is found to be well reproducible, this could lead to a control of the growth direction and crystal orientation even on amorphous substrates. This would imply a significant gain of

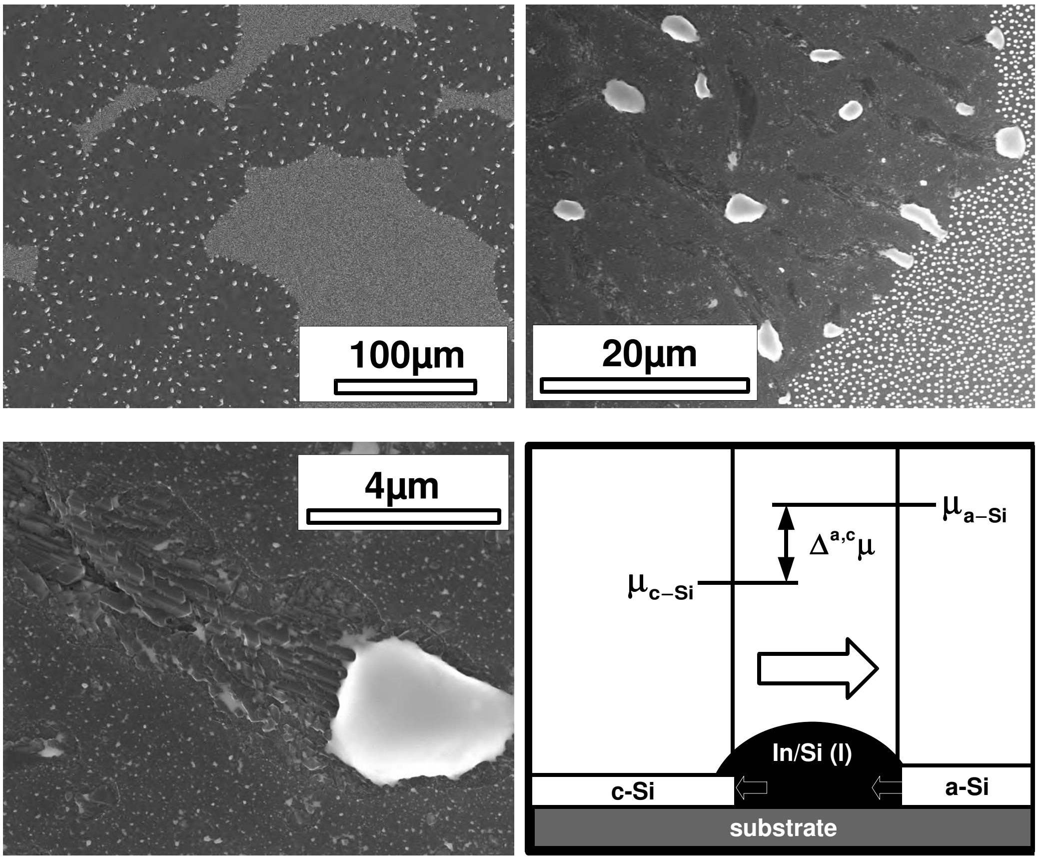

Figure 7.1: The solid–liquid–solid mechanism for growth of crystalline silicon on glass.

applicability for electronic devices as this would enable control of the orientation of the grain boundaries.

In order to gain a closer insight, a systematic study must imply the lateral confinement of the moving solvent droplets which can be realized by a dedicated oxidation of the amorphous silicon. Control of crystal orientation might in this way be gained by a channel structure which forces individual droplets to move in a parallel way. Solution growth should be used to enlarge the seed crystals as it allows high purity and a high perfection of the grown material as could have been shown in this work. It is therefore worth to dedicate more attention to the new approach briefly outlined above.

Appendix A

To be able to predict the absolute position and relative intensity of apparent X–ray diffraction peaks, the type and size of the unit cell as well as the positions of the atoms in the unit cell have to be known. The following phases in the Mo–Si–In system were considered in connection with the analysis of the spectra:

Si							[90]
	a	b	c	α	β	γ	V
cell	5.4308	5.4308	5.4308	90	90	90	160.2
	Z	x	y	z			
Si	14	0.125	0.125	0.125			
spgrp	227-2	cubic					

t-MoSi$_2$							[91]
	a	b	c	α	β	γ	V
cell	3.211	3.211	7.825	90	90	90	80.7
	Z	x	y	z			
Mo	42	0	0	0			
Si	14	0	0	0.3354			
spgrp	139	tetrag.					

h-MoSi$_2$							[92]
	a	b	c	α	β	γ	V
cell	4.622	4.622	6.646	90	90	120	123.0
	Z	x	y	z			
Mo	42	0.5	0.5	0.8333			
Si	14	0.8358	0.1642	0.8333			
spgrp	180	hexag.					

Table 1: Crystallographic data for the phases in the In–Si–Mo system I, lattice constants in [Å].

Mo_5Si_3							[93]
	a	b	c	α	β	γ	V
cell	9.650	9.650	4.911	90	90	90	457.3
	Z	x	y	z			
Mo	42	0.0786	0.2247	0			
Mo	42	0	0.5	0.25			
Si	14	0.171	0.671	0			
Si	14	0	0	0.25			
spgrp	140	tetrag.					

Mo_3Si							[94, 93]
	a	b	c	α	β	γ	V
cell	4.89	4.89	4.89	90	90	90	116.9
	Z	x	y	z			
Mo	42	0	0	0			
Si	14	0.250	0	0.500			
spgrp	223	cubic					

Mo							[95]
	a	b	c	α	β	γ	V
cell	3.147	3.147	3.147	90	90	90	31.17
	Z	x	y	z			
Mo	42	0	0	0			
spgrp	229	cubic					

In							[96]
	a	b	c	α	β	γ	V
cell	3.2523	3.2523	4.9461	90	90	90	52.3
	Z	x	y	z			
In	49	0	0	0			
spgrp	139	tetrag.					

Table 2: Crystallographic data for the phases in the In–Si–Mo system II, lattice constants in [Å].

Bibliography

[1] S. Glunz. Stand und Perspektiven der Photovoltaik. `http://adsabs.harvard.edu/cgi-bin/nph-bib_query?bibcode=1992ApPhL..61.2557Ydb_key=PHY`, 2005.

[2] F. Abdo, A. Fave, H. el Omari, M. Lemiti, C. Bernard, and A. Pisch. Growth of silicon by liquid phase epitaxy at low temperature: application to thin film solar cells. *M. J. Condensed Matter*, 11(1):15–17, 2009.

[3] R. B. Bergmann, G. Oswald, M. Albrecht, and V. Gross. Growth of silicon by liquid phase epitaxy at low temperature: application to thin film solar cells. *Sol. Energy Mater. Sol. Cells*, 46(2):147–155, 1997.

[4] R.H. Buitrago, G.A. Risso, M. Cutrera, M. Battioni, L. De Bernardez, J.A. Schmidt, R.D. Arce, and R.R. Koropecki. Polycrystalline silicon thin film solar cells prepared by PECVD-SPC. *Int. J. Hydrogen Energy*, 33(13):3522 – 3525, 2008.

[5] C. T. Angelis, C. A. Dimitriadis, M. Miasaka, F. V. Farmakis, G. Kamarinos, J. Brini, and J. Stoemenos. Effect of excimer laser annealing on the structural and electrical properties of polycrstalline silicon thin film transistors. *J. Appl. Phys.*, 86(8):4600–4606, 1999.

[6] G. Andrae, J. Bergmann, and F. Falk. Laser crystallized multicrystalline silicon thin films on glass. *Thin Solid Films*, 487(1–2):77–80, 2005.

[7] O. Nast, T. Puzzer, L. M. Koschier, A. B. Sproul, and S. R. Wenham. Aluminum induced crystallization of amourphous silicon on glass substrates above and below the eutectic temperature. *Appl. Phys. Lett.*, 73:3214–3216, 1998.

[8] B. Gorka, P. Dogan, I. Sieber, F. Fenske, and S. Gall. Low–temperature epitaxy of silicon by electron beam evaporation. *Thin Solid Films*, 515(19):7643–7646, 2007.

[9] P. Bennema and O. Sohnel. Interfacial surface tension for crystallization and precipitation from aqueous solutions. *J. Cryst. Growth*, 102:547–556, May 1990.

[10] C.D. Thurmond and M. Kowalchik. Germanium and silicon liquidus curves. *Bell Syst. Tech. J.*, 39:169–204, 1960.

[11] C. W. Bale, P. Chartr, S. A. Degterov, G. Eriksson, K. Hack, R. Ben Mahfoud, J. Melançon, A. D. Pelton, and S. Petersen. Factsage thermochemical software and databases. *Calphad*, 26:189–228, Jun 2002.

[12] C. Spinella and S. Lombardo. Crystal grain nucleation in amorphous silicon. *J. Appl. Phys.*, 84(10):5383–5414, 1998.

[13] F. Rosenberger. *Fundamentals of Crystal Growth I.* Springer Verlag Berlin, 1979.

[14] R. Srivastava and K. N. Khanna. Stokes–Einstein relation in two- and three-dimensional fluids. *J. Chem. Eng. Data*, 54:1452–1456, Apr 2009.

[15] Kenneth A. Jackson. *Kinetic Processes.* Wiley-VCH Verlag GmbH & Co. KGaA, 2004.

[16] I. Markov. *Crystal Growth for Beginners: Fundamentals of Nucleation, Crystal Growth, and Epitaxy.* World Scientific Publishing Company, 2004.

[17] W. A. Tiller. *The science of crystallization: macroscopic phenomena and defect generation.* Cambridge University Press, 1991.

[18] A. A. Chernov. Stability of faceted shapes. *J. Cryst. Growth*, 24–25:11–31, 1974.

[19] P. Hartman and W. G. Perdok. On the relations between structure and morphology of crystals I. *Acta Cryst.*, 8(1):49–52, 1955.

[20] J. van Suchtelen and E. van Veenendaal. The construction of orientation-dependent crystal growth and etch rate functions. Part I. Mathematical and physical aspects. *J. Appl. Phys.*, 87:8721–8731, 1994.

[21] W. Burton, N. Cabrera, and F. Frank. The growth of crystals and the equilibrium structure of their surfaces. *Philos. Trans. R. Soc. London, Ser. A*, 243: 299–358, 1951.

[22] P. Bennema and J.P. van der Erden. *Crystal Graphs, connected nets, roughening transition and the morphology of crystals*, chapter 1, pages 1–76. Materials Science of Minerals and Rocks. Terra Scientific Publishing Company, 1987.

[23] X.-Y. Liu and P. Bennema. Theoretical consideration of the growth morphology of crystals. *Phys. Rev. B*, 53:2314–2325, 1996.

[24] H. M. Cuppen, H. Meekes, W. J. W. van Enckevort, and E. Vlieg. Birth–and–spread growth on the Kossel and a non–Kossel surface. *J. Cryst. Growth*, 286: 188–196, 2006.

[25] I. Sunagawa. *Growth Histories of Mineral Crystals as seen from Their Morphological Features*, chapter 1, pages 1–24. William Andrew Inc./ Springer Verlag Berlin, 2003.

[26] M. Substyk. The origin of synthetic polycrystalline skeletal diamonds. *Cryst. Res. Technol.*, 23:1443–1447, 1988.

[27] T. Young. An essay on the cohesion of fluids. *Philos. Trans. R. Soc. London*, 95:65–87, 1805.

[28] A. Sharma. Relationship of thin film stability and morphology to macroscopic parameters of wetting in the apolar and polar system. *Langmuir*, 9:861–869, 1993.

[29] A.-M. Cazabat. How does a droplet spread? *Contemp. Phys.*, 28(4):347–364, 1987.

[30] A. Sharma. Equilibrium and dynamics of evaporating or condensing thin fluid domains: Thin film stability and heterogeneous nucleation. *Langmuir*, 14: 4915–4928, 1998.

[31] D. M. Mattox. *Handbook of Physical Vapor Deposition (PVD) Processing.* William Andrew Publishing, 1998.

[32] DIAS Infrared. PYROSOFT (software package). See: http://www.dias-infrared.de/index.php/content/view/27/76/lang,de/, 2008.

[33] R. Bergmann and J. Kurianski. The role of hydrogen in silicon liquid phase epitaxy. *Mater. Lett.*, 17(3–4):137–140, 1993.

[34] J. A. Friedrich, G. W. Neudeck, and S. T. Liu. Limitations in low-temperature silicon epitaxy due to water vapor and oxygen in the growth ambient. *Appl. Phys. Lett.*, 53(25):2543–2545, Dec 1998.

[35] W. Kern and D. Puotinen. Cleaning solutions based on hydrogen peroxide for use in silicon semiconductor technology. *RCA Review*, 31:187, Jun 1970.

[36] UTHSCSA ImageTool. See: http://ddsdx.uthscsa.edu/dig/itdesc.html, accessed: December 2009.

[37] Mike Hayles. *xt Nova Nanolab User's Manual.* FEI Company, 1st edition, 2003.

[38] Petr Klapetek and David Necas. Gwyddion – a free SPM data analysis software. Online: http://www.gwyddion.net, accessed: February 2009.

[39] E. N. Kaufmann. *Characterization of Materials*, volume 1 and 2. Wiley–Interscience, 2003.

[40] A. L. Patterson. The Scherrer formula for x–ray particle size determination. *Phys. Rev.*, 56:978–982, 1939.

[41] W. Kraus and G. Nolze. POWDER CELL – a program for the representation and manipulation of crystal structures and calculation of the resulting X-ray powder patterns. *J. Appl. Crystallogr.*, 29(3):301–303, 1996.

[42] J. K. Cockroft and A. N. Fitch. *Experimental Setups*, chapter 2, pages 33–36. RSC Publishing, 2008.

[43] W. Nolting. *Elektrodynamik*, volume 3 of *Grundkurs Theoretische Physik.* Springer Verlag Berlin, 2004.

[44] RCRefSimW v1.08. refer to: http://www.ihp-microelectronics.com/4.0.html (accessed 30.11.2009), accessed November 2009.

[45] C. Gu. *SIMS quantification of matrix and impurity species in III–nidride alloys.* PhD thesis, North Carolina State University, 2005.

[46] T. Boeck, T. Teubner, K. Schmidt, and P.-M. Wilde. A method to grow silicon crystallites on glass. *J. Cryst. Growth*, 198-199:420–424, Mar 1999.

[47] D. Hourlier-Bahloul and P. Perrot. Comprehension of the S(V)LS mechanism growth of silicon-based nanowires. *C.R. Chim.*, 10(7):658–665, 2007.

[48] M. A. McClelland and J. S. Sze. Surface tension and density measurements for indium and uranium using a sessile-drop apparatus with glow discharge cleaning. *Surf. Sci.*, 330:313–322, Jun 1995.

[49] P. Baeri, G. Foti, J. M. Poate, and A. G. Cullis. Phase transitions in amorphous si produced by rapid heating. *Phys. Rev. Lett.*, 45:2036–2039, 1980.

[50] M. G. Grimaldi, P. Baeri, M. A. Malvezzi, and C. Sirtori. Thermodynamic properties of amorphous silicon investigated by pulsed laser heating. *Int. J. Thermophys.*, 13(1):141–151, 1992.

[51] E. P. Donovan, F. Spaepen, J. M. Poate, and D. C. Jacobson. Homogeneous and interfacial heat releases in amorphous silicon. *Appl. Phys. Lett.*, 55:1516–1518, Oct 1989.

[52] M. I. Alonso and E. Bauser. Growth of $si_{1-x}ge_x$ on silicon by liquid–phase epitaxy. *J. Appl. Phys.*, 11(62):4445–4449, 1987.

[53] C. D. Thurmond. Phase equilibria in the GaAs and the GaP systems. *J. Phys. Chem. Solids*, 26:785–802, 1965.

[54] S. P. Yatsenko and E. N. Dieva. Solubility of refractory metals in liquid indium. *Zh. Fiz. Khim.*, 110(47):1658, 1973.

[55] The scientific group thermodata Europe. See: http://www.sgte.org, accessed Jan. 2010.

[56] A. Gokhale and G. Abbaschian. The Mo-Si (molybdenum–silicon) system. *J. Phase Equilib. Diffus.*, 12:493–498, Aug 1991. 10.1007/BF02645979.

[57] X. Y. Wang, I. T. H. Chang, and M. Aindow. A transmission electron microscope study of microstructural development in magnetron-sputtered $MoSi_2$ thin films. *Intermetallics*, 10:829–839, Sep 2002.

[58] O. Thomas, R. Madar, J.-P. Senateur, and F. dH́eurle. Comment. On the recently published Mo–Si equilibrium phase diagram. *J. Phase Equilib.*, 14(2): 136, 1993.

[59] E. Chi, J. Shim, J. Kwak, and H. Baik. Silicide formation by solid-state diffusion in Mo/Si multilayer thin films. *J. Mater. Sci.*, 31:3567–3572, Jan 1996.

[60] T. C. Chou and T. G. Nieh. Phase transformation and mechanical properties of thin $MoSi_2$ films produced by sputter deposition. *Thin Solid Films*, pages 48–57, 1992.

[61] C. M. Doland and R. J. Nemanich. Phase transformation during reactive molybdenum–silicide formation. *J. Mater. Res.*, 5(12):2854–2864, 1990.

[62] A. T. Voutsas, M. K. Hatalis, J. Boyce, and A. Chiang. Raman spectroscopy of amorphous and microcrystalline silicon films deposited by low–pressure chemical vapor deposition. *J. Appl. Phys.*, 78(12):6999–7006, 1995.

[63] P. Reinig, F. Fenske, W. Fuhs, A. Schöpke, and B. Selle. Crystalline silicon films sputtered on molybdenum: A study of the silicon–molybdenum interface. *Appl. Surf. Sci.*, 210:301–306, 2003.

[64] P. Suortti, M. Ahtee, and L. Unonius. Voigt function fit of x–ray and neutron powder diffraction profiles. *J. Appl. Cryst.*, 12:365–369, 1979.

[65] H. Richter, Z. P. Wang, and L. Ley. The one phonon Raman spectrum in microcrystalline silicon. *Solid State Commun.*, 39:625–629, 1981.

[66] A. H. van Ommen, A. H. Reader, and J. W. C. de Vries. Influence of microstructure on the resistivity of $MoSi_2$ thin films. *J. Appl. Phys.*, 64(7):3574–3580, 1988.

[67] N. Kaiser, A. Cröll, F.R. Szofran, S.D. Cobb, and K.W. Benz. Wetting angle and surface tension of germanium melts on different substrate materials. *J. Cryst. Growth*, 231:448–457, 2001.

[68] A. R. Saadat. Activation energies for surface diffusion and polarizabilities of gallium, indium and tin on a molybdenum surface. *J. Phys. D: Appl. Phys.*, 27:356–359, 1994.

[69] Gmelin. *Element Mo*, volume supplement A 2a of *Gmelin Handbook of Inorganic Chemistry.* Springer Verlag Berlin, 1985.

[70] L. Wang, A. Xian, and H. Shao. Density measurement of liquid indium and zinc by the γ–ray attenuation method. *High Temperatures. High Pressures*, 35–36(6):659–665, 2003–2007.

[71] M. V. Peralta-Martinez and W. A. Wakeham. Thermal conductivity of liquid tin and indium. *Int. J. Thermophys.*, 22(22):395–403, 2001.

[72] S.-J. Cheng, X.-F. Bian, J.-X. Zhang, X.-B. Qin, and Z.-H. Wang. Correlation of viscosity and structural changes of indium melt. *Mater. Lett.*, 57:4191–4195, Sep 2003.

[73] F. Groenvold. Heat capacity of indium from 300 to 1000 K. *J. Therm. Anal. Calorim.*, 13(3):419–428, 1978.

[74] B. Pivac, K. Furic, D. Desnica, A Borghesi, and A Sassela. Raman line profile in polycrystalline silicon. *J. Appl. Phys.*, 86(8):4383–4386, 1999.

[75] G. Bliznakov and S. Delineschew. Zur Theorie der orientierten Ausscheidung von Kristallen mit Diamantgitter auf strukturloser Unterlage. *Phys. Status Solidi B*, 13:101–110, 1966. ISSN 1521-3951.

[76] Winwulff stereographic projections. See: http://www.jcrystalsoft.com, accessed Jan. 2010.

[77] R. H. Hopkins. Impurities in silicon solar cells. Online at: `http://ntrs.nasa.gov/archive/nasa/casi.ntrs.nasa.gov/19860010264_1986010264.pdf`, Accessed: Jan 2010.

[78] T. Kilper, W. Beyer, G. Bräuer, T. Bronger, R. Carius, M.N. Donker, D. van den Hrunski, A. Lambertz, T. Merdzhanova, A. Mück, B. Rech, W. Reetz, R. Schmitz, U. Zastrow, and A. Gordijn. Oxygen and nitrogen impurities in microcrystalline silicon deposited under optimized conditions: Influence on material properties and solar cell performance. *J. Appl. Phys.*, 7:10, 2009.

[79] M. Schulz. *Semiconductors: Impurities and defects in group IV and III–V compunds*, volume III/22b. Springer Verlag Berlin, 1989.

[80] Krystalshaper. See: http://www.jcrystalsoft.com, accessed Jan. 2010.

[81] T. Teubner, R. Heimburger, N. Dessmann, T. Boeck, and R. Fornari. Two-dimensional nucleation probability for low-temperature homoepitaxial growth of silicon on different facets from metallic solutions. unpublished work, 2009.

[82] H. Reichert, M. Denk, J. Okasinski, V. Honkimaki, and H. Dosch. Giant metal compression at liquid–solid (Pb–Si, In–Si) Schottky junctions. *Phys. Rev. Lett.*, 98:116101–1–116101–4, 2007.

[83] S. Ranganathan. On the geometry of coincidence–site lattices. *Acta Cryst.*, 21: 197, 1966.

[84] D. Shechtman. Twin quintuplet surfaces in CVD diamond. *J. Mater. Sci.*, 41 (23):7720–7724, 2006.

[85] J. Faust and H. F. John. The growth of semiconductor crystals from solution using the twin-plane reentrant-edge mechanism. *J. Phys. Chem. Solids*, 25(12): 1407–1415, 1964.

[86] T. Kuroda, T. Irisawa, and A. Ookawa. Growth of polyhedral crystal from solution and its morphological stability. *J. Cryst. Growth*, 42:41–46, 1977.

[87] Min Chan Kim and Sang Goo Lee. Onset of solutal convection in liquid phase epitaxy system. *Korean J. Chem. Eng.*, 1(26):21–25, 2009.

[88] Dennis Elwell. Morphological stability of a crystal growing in solution. *Alabama Univ. UAH/NASA Workshop on Fluids Expt. System*, pages 154–159, 1979.

[89] W. F. Berg. Crystal growth from solutions. *Proc. R. Soc. London, Ser. A*, 164 (916):79–95, 1938.

[90] Powdercell structure file. Online at: `http://www.ccp14.ac.uk/ccp/ccp14/ftp-mirror/powdcell/Powder_Cell/structure_files/SILICON1.CEL`, accessed Jan. 2010.

[91] A. N. Christensen. Crystal growth and charaterization of the transition metal silicides $MoSi_2$ and WSi_2. *J. Cryst. Growth*, 129(1–2):266–268, 1993.

[92] L. F. Mattheis. Calculated structural properties of $CrSi_2$, $MoSi_2$ and WSi_2. *Phys. Rev. B: Condens. Matter*, 18:3253–3259, 1992.

[93] A. N. Christensen. Preparation and characterization of Mo_3Si and Mo_5Si_3. *Acta Chem. Scand.*, 28:519–522, 1983.

[94] D. H. Templeton and C. H. Dauben. The crystal structure of Mo_3Si. *Acta Crystallogr.*, 3:261–262, 1950.

[95] A. Goldmann. *Mo (Molybdenum) (Z = 42)*, volume 23c1 of *Landolt–Börnstein (New Series).* Springer Verlag Berlin, 2003.

[96] N. Ridley. Densities of some indium solid solutions. *J. Less–Common Metals*, 84:354, 1965.

List of Figures

List of Tables

Acknowledgements

I would like to thank Prof. Roberto Fornari for giving me the opportunity to work in the fascinating field of crystal growth at the Leibniz Institute for Crystal Growth in Berlin (IKZ), his ongoing support and his fruitful suggestions.

I am very grateful to all members of the group Si/Ge nanocrystals for contributing to a pleasant working atmosphere and for their very helpful practical and theoretical advice, but also for providing the opportunity of a free development of my work. Especially, I would like to thank the leader of the group, Dr. Torsten Boeck, who never got tired to believe in the success of my work and encouraged me with scientific, but also with interpersonal expertise. I wish to express my special gratitude to Peter Schramm for sharing his inexhausible know–how regarding the crystal growth equipment. I am grateful to Dr. Thomas Teubner for the enduring support in solving theoretical and practical problems and the fruitful discussions. I would like to thank Nils Deßmann for the experimental assistance during the last year and for his critical analysis of the findings.

I would like to express my further gratitude for the people, who supported the characterization of the crystals grown in this work: Dr. Martin Albrecht from IKZ for his advice regarding the operation of the electron microscope and the EDX system, Albert Kwasniewski and Dr. Martin Schmidbauer, also from IKZ, for providing the X–ray analysis data, the staff at RTG Mikroanalyse GmbH for the collaboration regarding the SIMS measurements, Dr. Frank Nagel from DIAS Infrared GmbH for the introduction to pyrometric temperature measurements, Dr. Klaus Irmscher from IKZ for explaining the Raman system, and Dr. Thomas Teubner for the help with the AFM measurements.

For proof reading, I would like to thank my long–standing friend Carsten Pfüller.

At the end, I would like to thank my wife and my parents for their ongoing encouragement, advice and sympathy.

Publications

1. R. Heimburger, Th. Teubner, N. Deßmann, H.P. Schramm, T. Boeck, R. Fornari: *Solution growth of crystalline silicon on glass in the In-Si-Mo system*, Journal of Crystal Growth 312, Issue 9 (2010), Pages 1632–1635
2. Th. Teubner, R. Heimburger, K. Böttcher, T. Boeck, R. Fornari: *Equipment for low temperature steady state growth of silicon from metallic solutions*, Crystal Growth and Design 8 (2008), Pages 2484–2488
3. Th. Teubner, U. Jendritzki, K. Böttcher, G. Schadow, R. Heimburger, A.K. Gerlitzke, S. Deiter, C. Eisenschmidt, T. Boeck, R. Fornari, M. Hanke: *Liquid phase epitaxy set-up designed for in situ X-ray study of SiGe island growth on (001) Si substrates*, Crystal Research and Technology 43 (2008) 1278–1285
4. J. Schneider, R. Heimburger, J. Klein, M. Muske, S. Gall, W. Fuhs: *Aluminum–induced crystallization of amorphous silicon: influence of temperature profiles*, Thin Solid Films 487 (2005), Pages 107–112
5. J. Klein, J. Schneider, M. Muske, R. Heimburger, S. Gall, W. Fuhs: *Aluminum–induced crystallization of amorphous silicon: parameter variation for optimisation of the process*, Proc. of the 31st IEEE Photovoltaic Specialists Conference, Orlando, USA, (2005)

Selbständigkeitserklärung

Ich erkläre, dass ich die vorliegende Arbeit selbständig und nur unter Verwendung der angegebenen Literatur und Hilfsmittel angefertigt habe.

Berlin, den 25. Januar 2010 Robert Heimburger